공학박사학위논문

Flame Structure and Combustion Instability Characteristics of Non-premixed GO_2/GCH_4 Flames in a Recessed Single Coaxial Injector

리세스가 있는 단일 동축형 분사기의 비예혼합 GO_2/GCH_4 화염의 구조 및 연소불안정 특성

2021년 2월

서울대학교 대학원

기계항공공학부

배 진 현

Flame Structure and Combustion Instability Characteristics of Non-premixed GO_2/GCH_4 Flames in a Recessed Single Coaxial Injector

리세스가 있는 단일 동축형 분사기의
비예혼합 GO_2/GCH_4 화염의 구조 및 연소불안정 특성

지도교수 윤 영 빈

이 논문을 공학박사 학위논문으로 제출함

2020년 5월

서울대학교 대학원
기계항공공학부
배 진 현

배진현의 공학박사학위 논문을 인준함

2020년 6월

위 원 장 余載洞
부위원장 尹 昌 植
위 원 李 福 植
위 원 趙 杜 衡
위 원 孫 采 秉

ABSTRACT

Although numerous studies have been conducted to solve the combustion instability, which is one of the biggest obstacles in the design process of propulsion engines and low NO_x gas turbine combustors, a general solution for combustion instability has not been proposed. Previous studies have used equivalence ratio or oxidizer-to-fuel (O/F) ratios to determine the combustion characteristics, however, even with the constant O/F ratios, different flame shapes have been formed, resulting in different combustion characteristics. Therefore, the flame shape should also be considered in evaluating combustion instability. Furthermore, only a low and narrow range of modulation frequencies has been used to measure the flame transfer function (FTF) in previous research although the combustion instability occurs mainly in the high-frequency region. Therefore, a direct comparison between combustion instability and FTF was hard to be performed. Moreover, there are fewer studies on combustion instability characteristics of non-premixed methane-oxygen flames, used in launch vehicles, compared to those of premixed flames used in gas turbines. However, the combustion instability of non-premixed flame must be completely resolved in advance because the launch vehicles are hard to be stopped and improved after the launch.

This paper explores the combustion instability characteristic of a recessed coaxial injector using methane, which has recently been spotlighted as an eco-friendly fuel for reusable launch vehicles. Also, the flame shapes and reason of combustion instability mode shifting phenomenon are investigated. Furthermore, a study on FTF is conducted to predict combustion instability, which is the final goal of the combustion instability research.

Before investigating the combustion instability characteristics, the flame shapes are explored with varying O/F ratios and external acoustic modulation to understand the bistable flame characteristics. As a result, attached and detached flames occur, and detached flames exhibit stronger pressure and heat release rate perturbations, compared to attached flames. The bifurcation diagrams of the bistable flames, based on flame shapes,

are generated by varying the O/F ratio and acoustic modulation strength under oxygen flow. These show that while an attached flame can not be lifted off from the injector rim by varying the velocity difference between oxygen and methane, it can be lifted off by high-strength acoustic forces. Conversely, a detached flame can be attached to the injector rim by increasing the velocity difference between oxygen and methane or with moderate acoustic modulation. Therefore, the velocity difference between oxygen and methane and the external modulation are primarily responsible for determining the flame shape. A large velocity difference causes the strong mixing between the oxygen and methane, which results in pulling the flame toward the injector, and finally causing the transition from detached to attached flames. However, the strong acoustic perturbation can interrupt the chemical reaction and cause local extinction, thus causing a transition from the attached to detached flames. The transitions between flame shapes are analyzed using the flame shape and pressure data. The continuous wavelet transform is applied to determine the frequency characteristics during the transitions.

Then, combustion experiments are conducted using a plug nozzle that is confirmed to form a closed acoustic boundary at the downstream end of the combustor through acoustic perturbation experiments. A mode analysis is performed for instability frequency occurring at various O/F ratios. The instabilities are observed in the 1st, 3rd, and 4th harmonic modes of the longitudinal fundamental resonant frequency of the combustor. For intensive research into the instability, the total delay time is measured under each O/F ratio. As a result, instability mode shifts to lower mode as increasing the total delay time. Based on the Rayleigh criterion, the reason for the instability mode shift phenomenon is that the acoustics mode, where the constructive interference between the pressure and heat release rate perturbations inside the combustor occurs, is shifted to the lower mode.

As increasing the combustor length at a fixed O/F ratio, the instability frequency gradually decreases to match the resonant frequency of the combustor and then transitions to the higher mode. This is because varying the combustor length results in a transition of acoustic modes where the constructive interference between the pressure and heat release rate perturbations occurs according to the Rayleigh criterion.

Furthermore, at each O/F ratio, the combustion instability frequency is defined as a

frequency where the strongest pressure perturbation occurs as varying the combustor length. As a result, the combustion instability frequency decreases as increasing the total delay time. According to the time-lag analysis, when the product of total delay time and instability frequency satisfies particular conditions ($n - 0.5$, n: positive integer), the combustion instability theoretically occurs owing to the constructive interference between the pressure and heat release rate perturbations. In this study, the strength of pressure perturbations is greatly amplified when the product of measured total delay time and instability frequency coincides with a theoretical value of 0.5.

Finally, a study is conducted on the FTF which can be used to predict the combustion instability by understanding the flame characteristics. First, as a result of measuring the FTF of bistable flames, the FTF gain for the detached flame has a larger value than that for the attached flame. Since the FTF gain represents the heat release rate perturbations due to the constant external perturbation, FTF results can indicate that the detached flame is more sensitive to external disturbances. Furthermore, the FTF is measured at each O/F ratio, and the peak frequency of FTF gain almost coincides with the combustion instability frequency. The peak frequency of the FTF gain indicates the inherent instability frequency of the flame, which means that the strongest heat release rate perturbations occur at that frequency. If the resonant frequency of the combustor coincides with the inherent instability frequency, positive feedback, amplifying the flame oscillation, occurs due to the resonance of that frequency perturbation, which results in the combustion instability. Therefore, the peak frequencies of the FTF gain and the combustion instability frequencies well match. In addition, as a result of performing the combustion instability prediction using the measured FTFs and the flame shapes, the instability mode shifting phenomenon and the frequency of combustion instability are reasonably predicted compared to the experimental results. The collective understanding of flame shapes and combustion instability of non-premixed flames, formed in a recessed coaxial injector, is advanced based on the experimental approach. Furthermore, the instability prediction is also made using measured FTFs and flame shapes. Therefore, these results will serve as a reference for future studies on improving the combustion stability using non-premixed flames and on understanding the shapes and characteristics of non-premixed flames.

Keywords: Non-premixed Flames, Recessed Coaxial Injector, Bistable Flames, Flame Shape, Combustion Instability, Instability Mode Shifting, Time-lag analysis, Flame Transfer Function, OH-PLIF, PIV, Combustion Instability Prediction

Student Number: 2015-20773

LIST

LIST OF FIGURES

LIST OF TABLES

NOMENCLATURE

Acronyms

A-D	from Achored to Detached flame
AES	Atomic Emission Spectroscopy
ATF	Aoustic Transfer Function
CFD	Computational Fluid Dynamics
CMOS	Complementary Metal-Oxide Semiconductor
CWT	Continuous Wavelet Transform
D-A	from Detached to Anchored flame
DP	Dynamic Pressure sensor
DSLR	Digital Single-Lens Reflex
DWT	Discrete Wavelet Transform
FAA	Federal Aviation Administration
FATF	Flame Area Transfer Function
FFT	Fast Fourier Transform
FTF	Flame Transfer Function
FOV	Field Of View
HWA	Hot Wire Anemometer
LEM	Lunar Excursion Module
LES	Large Eddy Simulation
MFC	Mass Flow Controller
Nd-YAG	Neodymium-doped Yttrium Aluminum Garnet
Nd-YLF	Neodymium-doped Yttrium Lithium Fluoride
O/F	Oxidizer-to-Fuel
ORZ	Outer Recirculation Zone
PaSR	Partially Stirred Reactor
PIV	Particle Image Velocimetry
PLIF	Planar Laser-Induced Fluorescence
PMT	PhotoMultiplier Tube

PVC	Precessing Vortex Core
SP	Static Pressure sensor
SSME	Space Shuttle Main Engine
STFT	Short Term Fourier Transform
RANS	Reynolds-Averaged Navier-Stokes
RI	Rayleigh's Index
RMS	Root Mean Square
RR	Recess Ratio
UV	Ultra Violet
WT	Wavelet Transform

Alphabet

a	scale parameter in continuous wavelet transform
$A_{angular}$	total area of swirl channels
A_{axial}	axial exit area for annular swirled methane jet
b	position parameter in continuous wavelet transform
C	CWT coefficient
D	oxygen post diameter
f_{ext}	external modulation frequency
$F_{Location}$	location of assumed thin flame for instability prediction
f_v	vortex shedding frequency
L_{recess}	length of recess
$\dot{m}_{CH_4}$	methane mass flow rate
OH^*	hydroxyl radical
$\bar{p}$	average pressure
p'	pressure perturbations
$\bar{q}$	average heat release rate
q'	heat release rate perturbations
S	swirl number

$S_{i,j}$	strain tensor
St	Strouhal number
T	acoustic period
$\bar{u}$	average oxygen inlet velcocity
u'	oxygen velcoity perturbations
ΔV	velocity difference between oxygen and methane
$\dot{V}_{O_2}$	oxygen volume flow rate
$\dot{V}_{CH_4}$	methane volume flow rate

Greek symbols

$\theta_{p'-q'}$	phase difference between the p' and q' inside the combustor
$\varepsilon_{xy,max}$	shear strain magnitude
τ_{ci}	delay time from pressure at flame to pressure at injector
τ_{pv}	delay time from pressure to mass flow modulation at injector
$\tau_{convect}$	convection delay time
τ_{eq}	equivalent delay time
τ_{total}	total delay time
Ψ	wavelet function in continuous wavelet transform
ϕ	equivalence ratio
ψ	stream function
$\Omega_{i,j}$	rotation tensor
ω	modulation frequency

Subscript

comb	inside the combustor
ox	inside the oxygen feed line

CHAPTER 1

INTRODUCTION

Figures 1.1(a) and 1.1(b) show the known causes of worldwide launch vehicle failures from 1957 to May 2007 and from 1980 to May 2007, respectively, researched by the Federal Aviation Administration (FAA) in the United States of America [1]. As shown in Fig. 1.1(a), the propulsion problem accounts for the highest percentage of all the reasons for launch failure, and also the highest percentage in Fig. 1.1(b), which indicates the causes of the latest launch failure. The most representative problem in the propulsion stage is combustion instability. Therefore, it is very important to understand the characteristics of combustion instability for successful launches.

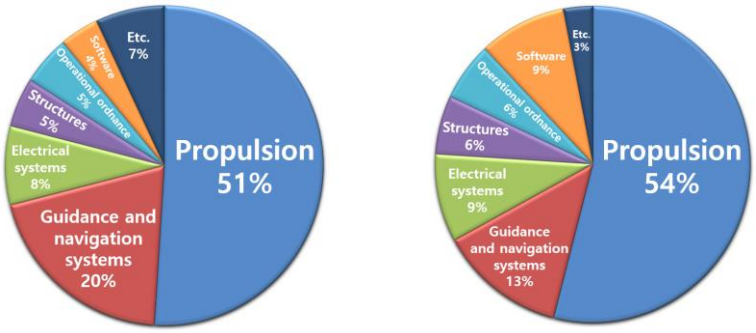

Fig. 1.1 Causes of launch vehicle failures worldwide (a) from 1957 to May 2007 and (b) from 1980 to May 2007 [1].

Figure 1.2 shows a chronology of combustion instabilities since the combustion instabilities were discovered in solid- and liquid-propellant rocket engines in the late 1930s [2]. The collective understanding of combustion instability mechanisms has been identified from many studies on coupling between fuel feed line/acoustic [3, 4], equivalence ratio oscillations [5], oscillatory atomization, vaporization and mixing [3, 4], oscillatory flame-

area variation [6], and vortex shedding [7, 8]. Furthermore, many studies [9, 10] base on various analytic methods such as time-lag analysis [11] have improved the understanding of combustion instability mechanism. The time-lag analysis describes the mechanism of combustion instability through the delay time between pressure perturbations (p') and heat release rate perturbations (q'). In addition, high repetition measurement techniques, such as planar laser-induced fluorescence (PLIF) and particle image velocimetry (PIV), have improved the understanding of the dynamic characteristics of flames and flows.

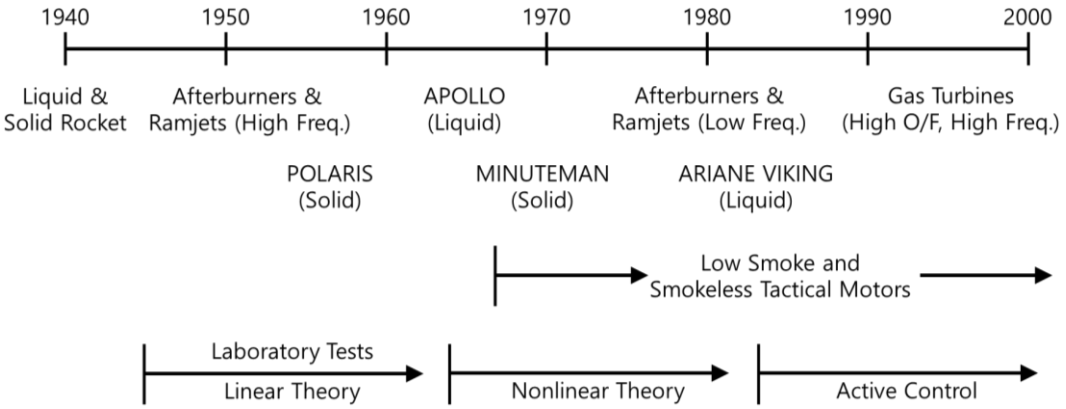

Fig. 1.2 Chronology of combustion instabilities [12].

Although numerous studies on combustion instability have been conducted, research on combustion instability of non-premixed flames has not been conducted sufficiently compared to that of premixed flames [13]. In the propulsion systems, the oxidizer and fuel flow separately into the combustion chamber. Therefore, to understand the combustion instability occurring in the launch vehicles, the characteristics of combustion instability for non-premixed flames should be identified.

Table 1.1 shows the advantages and disadvantages of typically used injector types for non-premixed flames. The impinging injectors, which are used for huge thrust chambers such as F-1, have a simple operating mechanism [14, 15] and are easy to be fabricated [14]. However, the simplicity of impinging injectors is plagued with its inherent susceptibility to

combustion instability [16]. The pintle injectors, which have recently been in the spotlight, are thrust-controllable [17, 18] and have high combustion efficiency [17]. However, the pintle injector has a complex structure and the tip of the pintle rod is very vulnerable to the high temperature due to the protrusion [19]. In addition, owing to the flame structure, the pintle injector has wall compatibility problems [15]. The coaxial injectors, which have been used in numerous launch vehicles so far, are reliable, have a low-pressure drop, and apply low heat loads to the wall of the combustion chamber [15]. However, the coaxial injector is difficult to manufacture when the annulus gap is designed very thin [15]. Also, the flame might become unstable during the throttling [15]. The purpose of this study is to identify the characteristics of combustion instability caused by the coaxial injectors mainly used in launch vehicles.

Table 1.1 Characteristics for typical types of rocket engine injector elements.

Type	**Advantages**	**Disadvantages**	**Application**
Impinging	· Simple operating mechanism [14, 15] · Easy fabrication [14]	· Inherent susceptibility to combustion instability [16]	· Huge thrust chamber (e.g. F-1) [14]
Pintle	· Great throttling [17, 18] · High combustion efficiency [17]	· Wall compatibility problems [15] · Complex structure [19] · Thermal vulnerability of the protruded pintle tip [19]	· LEM decent engine [15]
Coaxial	· Good wall compatibility [15] · Low-pressure drop [15] · Proven dependability [15]	· Difficult to fabricate if annulus gap is very small [15] · Tends to become unstable when throttled [15]	· Saturn II and IV B, J-2 [15] · SSME [15]

In a typical rocket engine shown in Fig. 1.3, the oxidizer and fuel flow into the combustion chamber separately, thus, it is very important to determine the characteristics of non-premixed flames. Furthermore, the main issues to be considered in the development of the recent rocket engines are eco-friendly, reusable, and combustion stability. To achieve these considerations, proper fuel should be selected. Methane is considered an eco-friendly fuel due to fewer pollutions since methane has the smallest amount of carbon per mole than

that of other hydrocarbon-based fuels. Although methane has a lower specific thrust than hydrogen, but is easy to produce, and has a higher specific thrust than other hydrocarbon-based fuels such as RP-1. In addition, since the coking limit of methane is 950 K, which is higher than that of RP-1, which is 560 K, less soot is generated [20], implying that the launch vehicles are easy to reuse. Furthermore, according to the previous studies [21-25], stabilizing effects of a recessed injector have been reported and the recessed region has been assumed as a small combustion chamber that is insensitive to combustion disturbances in the main chamber.

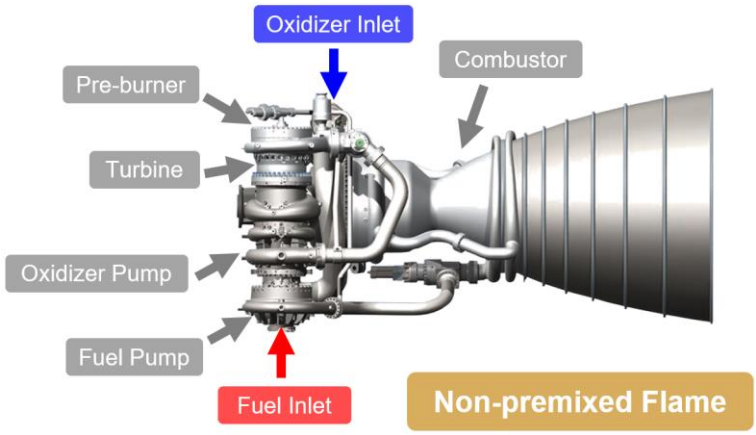

Fig. 1.3 Schematic of a typical rocket engine.

Typical large space launch vehicles use a staged combustion cycle that achieves improved performance by driving one turbine using an oxidizer- or fuel-rich propellant to drive each turbo pump and effectively deliver the propellant into the combustion chamber [26]. However, studies on a full-flow staged combustion cycle, in which two turbo pumps are driven by the oxidizer- and fuel-rich preburners, have been conducted in recent years [27, 28]. The full-flow staged combustion cycle has the advantage of extending the life of the engine and improving its reliability by separately driving the fuel and the oxidizer turbo pumps. In the full-flow staged combustion cycle, all the fuel and oxidizer flow through the preburner, and then the turbines are driven, such that all the propellant flowing into the

main combustor becomes gaseous [29]. The full flow staged combustion cycle is applied to the Raptor which is a reusable methane-fueled rocket engine manufactured by SpaceX.

The combustion instability frequency/mode shifting phenomenon, which is one of the characteristics of combustion instability, is a phenomenon in which the frequency or mode of combustion instability suddenly transitions to the other frequency or mode discontinuously as varying particular parameters. Balachandran et al. [30] reported that the instability frequency was shifted with varying the air flow rates in a laboratory-scale combustor for a maximum rating of 30 kW. Furthermore, Yoon et al. [31] found that the convection delay time ($\tau_{convect}$) of a partially premixed model combustor was the key parameter of the combustion instability frequency/mode shifting phenomenon.

Therefore, as shown in Fig. 1.4, this study is conducted to investigate the combustion instability characteristics of non-premixed flame using gaseous oxygen and gaseous methane in a recessed coaxial injector, especially the combustion instability mode/frequency shifting phenomenon.

Fig. 1.4 Objectives of this study to understand the combustion instability of non-premixed flames formed by a recessed coaxial injector.

The method for exploring the combustion instability can be classified into three categories: 1) analytic method [32-34], 2) numerical simulation (computational fluid dynamics (CFD) using Reynolds-averaged Navier-Stokes (RANS) [35, 36] or large eddy simulation (LES) [37-40]), and 3) experimental approaches [41-43]. Table 1.2 shows the classification of previous studies on combustion instability. In recent years, research [32, 44-48] has been actively conducted to compare the results from two or more methods from different categories for investigating the combustion instability, not just in each field, and through this, the reliability of each method has been improved. The present study employs

the experimental approaches to investigate the combustion instability of non-premixed gaseous oxygen-methane flames formed by a recessed coaxial injector. Furthermore, using an analytic model, the prediction of combustion instability is performed and compared to the experimental results.

Table 1.2 Classification of previous studies on combustion instability.

Category		Year	Affiliation	Research Group	Contents
Analytic solution		1998	Georgia Institute of Technology	T. Lieuwen B.T. Zinn	· Theoretical model was compared with the experimental results [32]
		2019	CNRS	S. Candel	· Analytical study of nonlinear coupling between azimuthal and axisymmetric modes in annular combustors [33]
		2020	University of California, San Diego	F.A. Williams	· Theory of droplet vaporization in the presence of fuel pyrolysis [34]
CFD	RANS	2004	K.U. Leuven	P. Sas	· Hybrid approach utilizing both CFD and thermoacoustic solvers [35]
		2017	Combustion Science & Engineering, Inc.	E.D. Gonzalez-Juez	· Simulation for instabilities on a bluff body stabilized combustor [36]
	LES	2005	Georgia Institute of Technology	V. Yang	· Effect of inlet swirl on combustion dynamics using a LES technique [37]
		2006	CNRS CERFACS	T. Poinsot	· LES and acoustic analysis of a swirled staged turbulent combustor [38]
		2016	Nanjing University of Aeronautics and Astronautics	J. Mao	· Turbulent lean combustion modeling using PaSR combustion model [39]
		2019	Technical University of Munich	W. Polifke	· LES of enhanced heat transfer in pulsatile turbulent channel flow [40]
Experimental Approach		2009	Massachusetts Institute of Technology	A.F. Ghoniem	· Parametric study on flame-vortex interaction [41]
		2010	Pennsylvania State University	D.A. Santavicca	· Both experimental and analytical study on spatially distributed FTF [42]
		2011	University of Cambridge	S. Hochgreb	· Nonlinear heat release response of stratified lean-premixed flames [43]

Furthermore, in the previous studies, the flame transfer function (FTF), which represents the heat release rate perturbation according to the external modulation, has been mainly used to understand the flame characteristics and to predict combustion instability. Therefore, accurate FTF calculation or measurement improves the accuracy of combustion instability prediction. However, the main subjects of studies on FTF have been premixed flames [45, 49, 50]. Furthermore, in the previous studies, the FTF at the frequency where the combustion instability occurred was not identified due to the narrow frequency range of external modulation for calculating or measuring the FTF. Thus, in this study, the FTF is experimentally measured in a wide frequency range of modulation and used to predict the combustion instability of non-premixed flames.

Even under constant operating conditions, flames can form in different shapes with different characteristics, which are called bistable flames. Various studies have been conducted on LES and experimental approaches to bistable flames, but most studies have been conducted on premixed flames, and studies on bistable flames of non-premixed flames have not been sufficient. In addition, in understanding the transition of flame shapes due to external modulation, studies have not been performed sufficiently because the strength range of external modulation was limited in the previous studies. Therefore, in this study, the characteristics of non-premixed flame shapes are studied, and the behavioral bifurcation characteristics of the bistable flames according to the oxidizer-to-fuel (O/F) ratio and a wide strength range of external modulation are also analyzed.

In summary, the purposes of this study are to explore the characteristics of flame shape and combustion instability, which occurs in a recessed coaxial injector, and finally to attempt to predict combustion instability using the measured flame shapes and FTFs. For achieving the objectives of this study, the following studies are conducted.

1. In Chapter 3, the characteristics of the flame shape formed in a recessed coaxial injector are investigated based on the O/F ratio and acoustic modulation strength variation. Even with the constant O/F ratios, different flame shapes are formed (detached and attached), resulting in different combustion characteristics. First, the characteristics of detached and attached flames under constant operating

condition are examined. Furthermore, the bifurcation diagrams of the bistable flames, based on flame shapes, are generated by varying the O/F ratio and acoustic modulation strength under oxygen flow.

2. In Chapter 4, this study examines the effect of the total delay time (τ_{total}), which is calculated using the flame shape and speed, measured by high repetition hydroxyl radical (OH^*) chemiluminescence, OH-PLIF, and PIV, on the combustion instability characteristics of a non-premixed methane-oxygen flame using a recessed coaxial injector. The experiments are repeated by varying the O/F ratio, which is a key parameter of τ_{total}, and combustor length. In addition, the instability mode/frequency shifting phenomenon is studied using the time-lag analysis and simplified Rayleigh criterion. Also, the frequency of combustion instability under each O/F ratio is determined based on the combustor length variation tests and the relationship between the τ_{total} and combustion instability frequency is studied for varied O/F ratios.
3. In Chapter 5, the inherent instability characteristics of flames are studied by measuring the FTFs. The FTFs are measured by keeping the velocity perturbation, which is the denominator of FTF, constant at 5%. First, the effects of distinct characteristics of two bistable flames on FTFs are determined by measuring the FTFs of bistable flames. Furthermore, the FTFs at all O/F ratios, in this study, are measured, and the peak frequencies of FTFs are compared to the combustion instability frequency. Finally, the combustion instability is predicted using the measured FTF and flame shape through an instability prediction tool (OSCILOS). The prediction results for combustion instability frequency and instability mode shifting phenomenon for varied O/F ratio and combustor length are compared to experimental results.

CHAPTER 2

EXPERIMENT AND MEASUREMENT SYSTEMS

2.1 Combustor and Injector

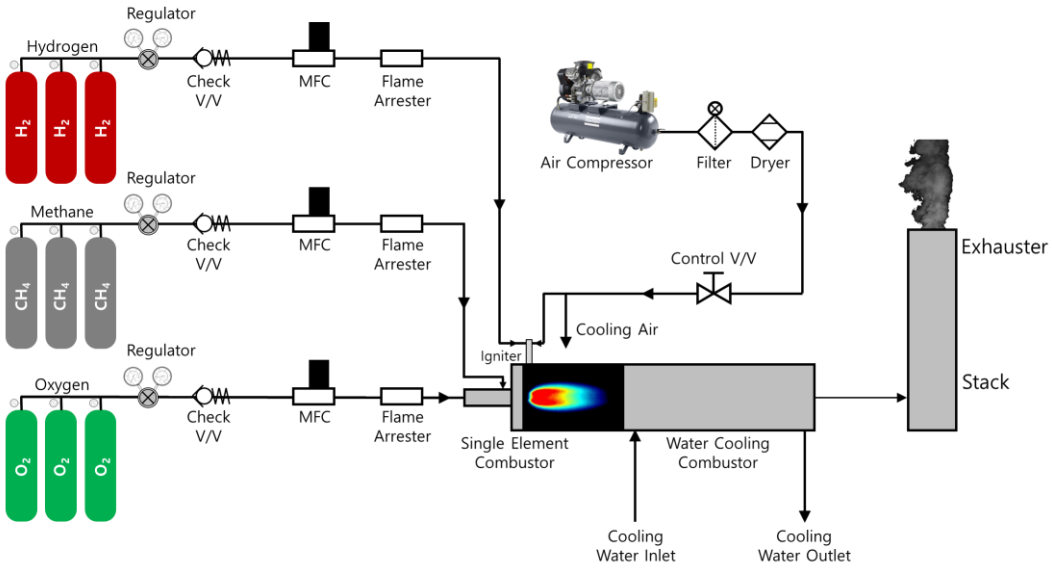

Fig. 2.1 Schematic diagram of the single element combustor test facility.

To explore the flame characteristics, an atmospheric-pressure and high-temperature single element combustion test facility for a recessed coaxial injector is installed. As shown in Fig. 2.1, this facility consists of an atmospheric pressure combustor, air compressor, an external stack, cooling systems using air and water, and supplying systems for oxidizer and fuel. Mass flow controller (MFC) (LineTech, M3300V, uncertainty = ± 1% of full range) is used for controlling the flow rates of oxygen, methane, and hydrogen which are provided from each bottle of high-purity feedstock gases (O_2 purity > 99.9 mol%, CH_4 purity > 99.95 mol%, and H_2 purity > 99.95 mol%). The combustion tests are conducted at slightly aviated pressure (1.05 ~ 1.2 bar) because a water-cooled plug nozzle is used to form an acoustic boundary at the combustor outlet by blocking 99.25% of the combustor area. The flow rate

of oxygen and methane are varied according to the purpose of tests.

Figure 2.2 shows the schematics of the combustion test rig and details for the recessed coaxial injector used in this study. The square cross-section of the combustor is 80 mm × 80 mm and the combustor, made from steel, consists of two parts.

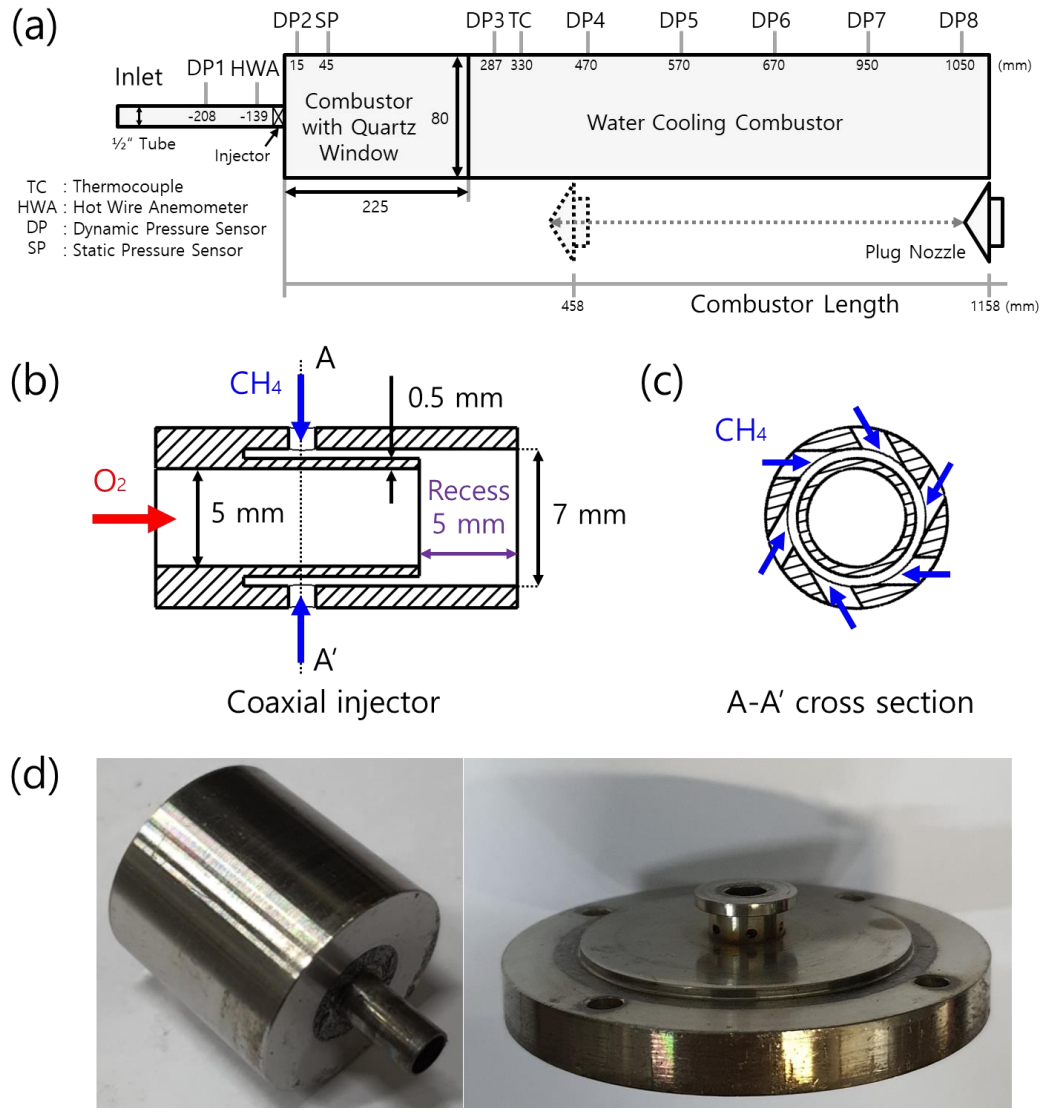

Fig. 2.2 Schematic diagram of (a) measurement sensor locations, (b-c) cross-sectional view of injector, and (d) direct photo for each part of the injector.

The front part is a combustor with four quartz windows on the sidewalls for optical access. The quartz windows are cooled by high-pressure injection of the air. The rear part is a ducted combustor with water channels for cooling. The length of the combustor can be controlled from 458 mm to 1,158 mm by moving the water-cooled movable plug nozzle. Gaseous oxygen and gaseous methane at 290 ± 5 K are supplied by MFCs through a center jet (diameter = 5 mm) and an annular swirled jet (outer diameter = 7 mm, inner diameter = 6 mm, 6 swirl channels), respectively. The cooling air is supplied after being pressurized to 4 bar using a compressor. The oxygen and methane are supplied to the MFCs at 5 bar controlled by regulators and ejected from the MFCs to the atmospheric pressure. The injector used in this study is a coaxial injector, and the oxygen in the center is ejected as a jet as shown in Fig. 2.2(b-d). Therefore, the swirl number can be calculated using the stream of methane. Since the six swirl channels are 1.4 mm in diameter, the swirl number (S) is 1.105 using Eq. (2.1).

$$\mathrm{S} = \frac{\dot{m}_{CH_4}/A_{angular}}{\dot{m}_{CH_4}/A_{axial}}, \tag{2.1}$$

where $\dot{m}_{CH_4}$ is the methane mass flow rate, $A_{angular}$ is the total area of swirl channels, and A_{axial} is the axial exit area for annular swirled methane jet.

The recess length, where oxygen and methane are mixed before entering the combustor, is designed to be 5 mm. Therefore, the recess ratio (RR), defined as the Eq. (2.2), is calculated as unity (1).

$$\mathrm{RR} = \frac{L_{recess}}{D}, \tag{2.2}$$

where L_{recess} is the length of recess and *D* is the oxygen post diameter.

2.2 Flame Imaging

In this study, since the hydrocarbon fuel (methane) is used for combustion tests, the OH^* is produced by chemical reactions. Therefore, to determine the shapes and centroid of flames, OH^* chemiluminescence images are captured. Direct photography has been used in many other studies to investigate the flame shape, however, images produced by this method are not good indicators of the reaction zone [51]. Hu et al. [52] experimentally measured OH^* and methylidyne radical (CH^*) radiation and compared them with the heat release rate. OH^* radiation has a strong linear correlation with heat release rate regardless of equivalence ratio [52]. However, a non-linearity in the correlation between CH^* radiation and the heat release rate increases as the equivalence ratio increases [52]. Thus, the OH^* chemiluminescence image should be used since OH radicals are good indicators of the reaction zone, which is a high-temperature region [51]. In this study, OH^* chemiluminescence images are captured with a complementary metal-oxide semiconductor (CMOS) camera (LaVision, HighSpeed Star 8, 1024 × 640 pixels) with an intensifier (LaVision, HighSpeed IRO), using a ultra-violet (UV) enhanced lens (LaVision, f = 100 mm, f/2.8) and a 320 ± 20 nm narrow bandpass filter (LaVision, 1108760 VZ). The images of OH^* chemiluminescence are taken with 5 μs exposure time and 10,000 images per second. The threshold value used to define the flame is 5% of the maximum intensity of the averaged image.

2.2.1. Chemiluminescence Spectroscopy [53]

In this study, OH^* chemiluminescence measurements are conducted to obtain the flame shapes and centroid by determining the reaction region. The analyte concentration can be determined through the quantitative measurements of the optical emission from the excited chemical species by applying the chemiluminescence which is similar to atomic emission spectroscopy (AES). However, chemiluminescence is different from AES because it is generally defined as emission from activated molecules instead of simply

excited atoms. The bands of light determined by chemiluminescence are wider and more complex because they come from molecular emissions than from bands of atomic spectra. In addition, chemiluminescence can occur in both the solution and gaseous phase while AES occurs mainly in the gaseous phase. Like fluorescence spectroscopy, the strength of chemiluminescence is determined by detecting the electromagnetic radiation produced in a system with very low background. To measure the chemiluminescence, the energy required to release the analyte into higher electronic, vibrational, and rotational states, where the energy can decay by emission, does not come from external light sources such as lasers or lamps, thus completely preventing the source disturbance. This excitation energy is generated by a chemical reaction of analyte and reagents. An example of a reaction of this sort is shown below:

$$CH_3 - S - CH_3 + F_2 \rightarrow \text{products} + hv\ (\text{light}), \tag{2.3}$$

where the analyte is dimethyl sulfide (C_2H_6S) and reagent gas is fluorine (F_2)

In gaseous phase chemiluminescence in the above example, the light emission, which is depicted as *hv*, is emitted by the reaction process of an analyte and a strongly oxidizing reagent gas or ozone. The production of light is intrinsically instantaneous because the reaction occurs on a short time scale. Thus, the analytes and reagents are simply mixed in a small volume chamber directly for most analyte systems. When the analytes are eluted from a gas chromatographic column, the end of the column is often supplied directly into the reaction chamber itself. Since much of the energy emitted by the reaction should be used to excite as many analyte molecules as possible (in the eyes of the analyst), energy loss through gas collisions is undesirable, so maintaining the gas pressure in the reaction chamber at low pressure (~ 1 torr) by a vacuum pump is a final consideration to minimize the effects of collisional deactivation. In the above reaction process, it is necessary to state that the ambiguous specification of "products" is often necessary because of the nature and complexity of the reaction. In some reaction processes, the chemiluminescence emitters are relatively well known. For instance, the major emitter is electronically and vibrationally

excited HF in the above reaction example, while other emitters have been determined whose identities are not known. In Chapters 3 and 4, OH^* chemiluminescence images are captured to determine the flame shape and centroid. Furthermore, in Chapter 5, the intensity of OH^* chemiluminescence signals is measured to determine the FTF.

2.2.2. OH PLIF Measurement

LIF is a sequence described as the absorption of a photon by a molecule of radical, followed by emission of a photon as the molecules transition from a higher energy state to a lower one [54]. Figure 2.3 shows the schematic of relaxation processes for the emission of photons. Some of the molecules will relax to the initial state by the emission of a photon [54]. However, several relaxation processes are possible including (a) spontaneous emission, (b) stimulated emission by exterior stimulus, (c) quenching by collision of molecules, (d) redistribution of energy level, and (e) change of molecular component by chemical reaction [54]. LIF signal is described as the rapid or spontaneous emissions of photons and the frequency of LIF signal can have a different value from that of inducing laser beam [54].

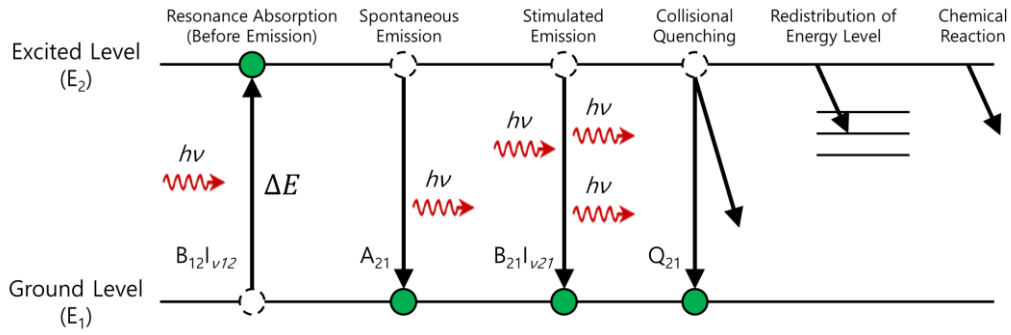

Fig. 2.3 Schematic of relaxation processes for the emission of photons [54].

By using OH-PLIF, spatially and temporally resolved images in the reaction zone can be obtained. Table 2.1 shows the formation and destruction of OH radicals which increase

rapidly around the flame in approximately 20 μs [55, 56] and then decompose gradually from 1 to 5 ms by a 3-body recombination reaction [57]. Thus, super-equilibrium OH exists near the flame front. The OH radical, which is an intermediate product of the chemical reaction, has a concentration of more ten times than that of O or H radicals [58]. When absorbing laser light, the more intensive fluorescence signal is measured from the OH radical than other species, so the fluorescence signal of OH radical is widely used as an indicator for determining the flame front in reacting flows [54].

Table 2.1 Formation and destruction of OH radical [54].

Fast OH formation by two-body reactions (~ 20 μsec)
$H + O_2 \leftrightarrow OH + O$ $O + H_2 \leftrightarrow OH + H$ $H + HO_2 \leftrightarrow OH + OH$
Slow destruction by three-body recombination reactions (1 ~ 5 msec)
$H + OH + M \leftrightarrow H_2O + M$

To observe the line positions for transition, I scan the dye laser and record the signal at each step. I intend to use $Q_1(8)$ transition of the $A^2\Sigma^+ \leftarrow X^2\Pi$ ($v' = 1$, $v'' = 0$) band (λ = 283.55 nm) for the excitation wavelength. Using a CMOS camera with a UV-enhanced lens (LaVision, f = 100 mm, f/2.8), in conjunction with a test flame in laminar premixed condition, a laser excitation scan is performed over the range of interest from λ = 283.4 nm to λ = 283.7 nm with 0.005 nm step. At every scanning step, 20 pulses of signals are recorded and averaged. After scanning the dye laser, the OH^* excitation spectrum can be obtained as shown in Fig 2.4. Among the peak values of the excitation spectrum, I use $Q_1(8)$ as the excitation wavelength of OH radical because it shows strong fluorescence and is almost temperature-insensitive over the flame temperature region (1400 K to 2500 K) [59, 60]. Figure 2.5 shows the OH^* fluorescence spectrum for $Q_1(8)$ measured in a previous study [61]. The peak value is found at around 308 ~ 320 nm.

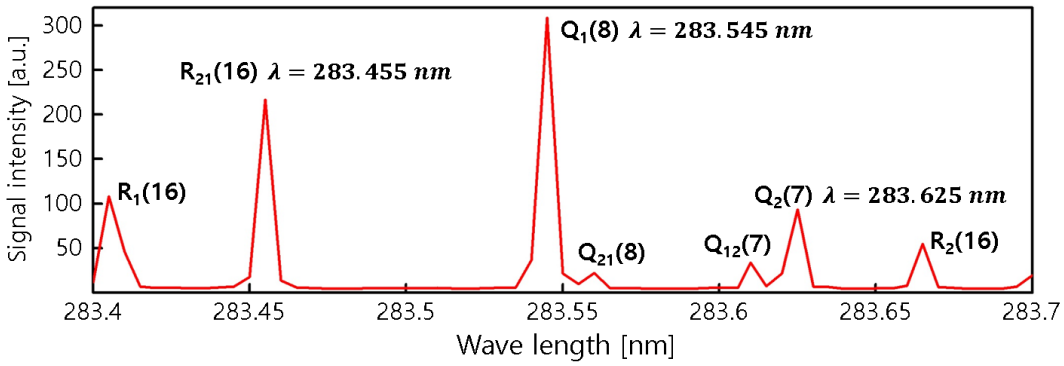

Fig. 2.4 Measured OH^* excitation spectrum; $Q_1(8)$ is used for OH-PLIF in this study.

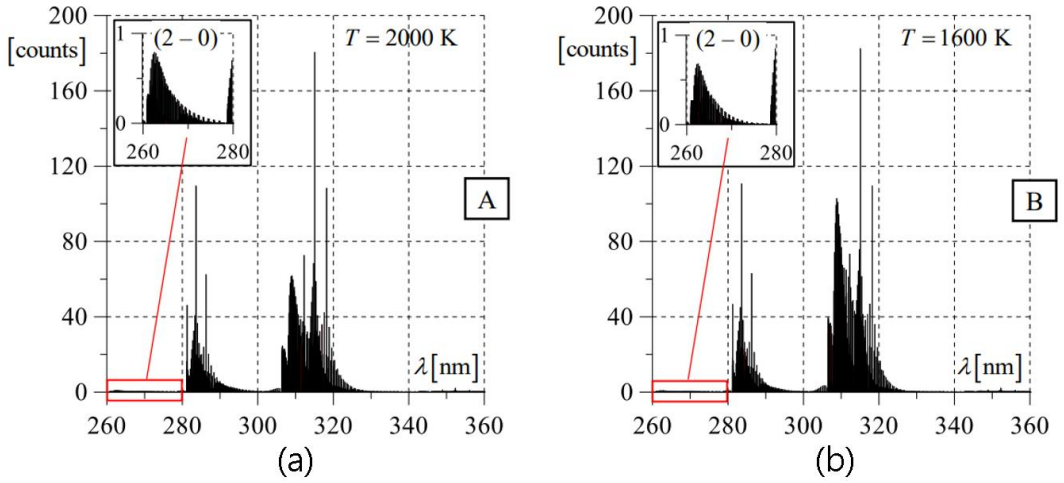

Fig. 2.5 OH^* fluorescence spectrum for $Q_1(8)$ at temperatures of (a) 2000 K and (b) 1600 K [61].

For OH PLIF, a neodymium-doped yttrium aluminum garnet (Nd-YAG) pumped by dye laser is turned to $Q_1(8)$ (λ = 283.545 nm). To measure the UV light, all the lenses made with quartz are used since UV light cannot penetrate the common glass. The region of interest is focused on the intensifier and CMOS camera. An advanced bandpass filter is used to block scattered signal lights. The transmittance of the filter is shown in Fig. 2.6. In addition, Fig. 2.7 shows the schematics of OH-PLIF system in this study.

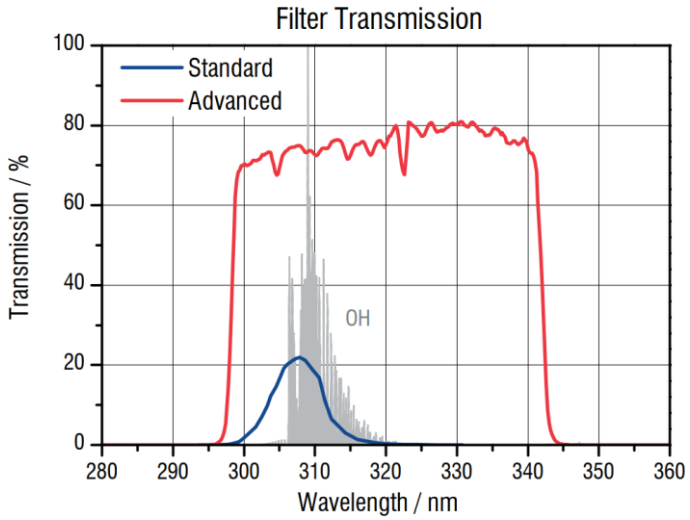

Fig. 2.6 The transmittance of the bandpass filter (LaVision, 1108760 VZ) (red line) shown in the manufacturer's catalog.

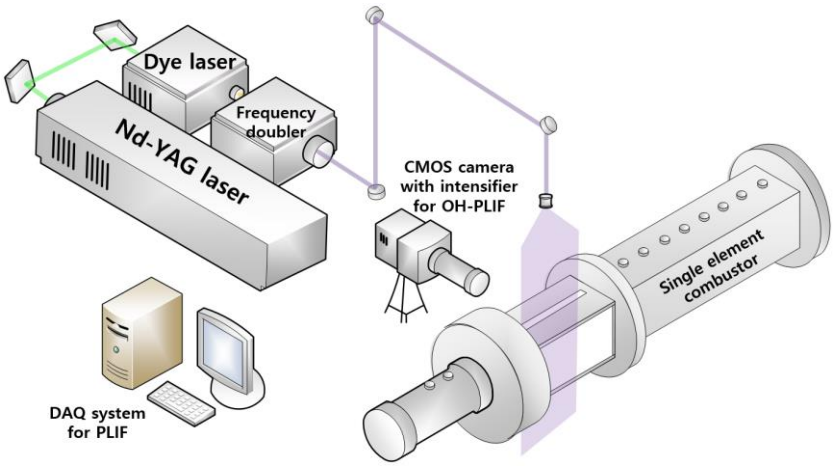

Fig. 2.7 Schematic diagram of OH-PLIF measurement system.

High-repetition laser measurements have been widely used in various research fields to find the unknown high repetition characteristics, so many research groups are conducting experimental approaches about CH_4/Air flame, liquid fuel flame, and micro structure of the flame [62]. The detailed information about the research is summarized in Table. 2.2 [62].

Table. 2.2 High-speed PLIF application research summary [62].

Research group	Year	Author	Contents	Repetition rate
AFRL	2013	S. Hammack	Plasma-enhanced flame characteristics of turbulent non-premixed flame [63]	10 kHz
CNRS	2012	P. Petersson	Simultaneous high-speed PIV & OH-PLIF about coaxial diffusion flame burner [64]	10 kHz
CNRS	2014	P. Xavier	Cavity flame anchoring characteristics based on high-speed OH-PLIF [65]	10 kHz
DLR	2010	I. Boxx	Simultaneous measurement of transient phenomena in a partially premixed swirl flame [66]	5 kHz
DLR	2011	M. Stohr	Blow off characteristics of CH_4 swirling flame [67]	5 kHz
DLR	2013	M. Stohr	Simultaneous measurement of PIV & OH PLIF in CH_4 swirling flame [68]	10 kHz
Michigan University	2015	P.M. Allison	CH_2O-PLIF measurements in dual-swirl burner [69]	4 kHz
Sydney University	2011	S. Meares	High-speed OH-PLIF imaging of extinction and re-ignition [70]	5 kHz
University of Cambridge	2011	J.R. Dawson	Near blow-off characteristics of bluff body stabilized CH_4 flame [71]	5 kHz
University of Cambridge	2012	N.A. Worth	Flame interaction of CH_4/Air conical bluff-body stabilized flame [72]	5 kHz

In this study, the high-frequency combustion instabilities are measured and high-repetition OH-PLIF is applied to explore the structural characteristics of flames. The OH-PLIF is conducted using an Nd-YAG laser (Edgewave, IS-200-2-L) and a dye laser (Sirah, Credo-Dye-LG-24). The OH-PLIF images are captured with a CMOS camera (LaVision, HighSpeed Star 8) with an intensifier (LaVision, HighSpeed IRO), using a UV-enhanced lens (LaVision, f = 100 mm, f/2.8) and a 320 ± 20 nm narrow bandpass filter (LaVision, 1108760 VZ). The OH-PLIF images are captured at 10 kHz. The field of view for the OH-PLIF is 110 mm × 70 mm.

2.2.3. PIV Measurement [53]

The velocity vector fields of a flow can be obtained using PIV by comparing consecutive two images. The experimental set-up of PIV system consists of several sub-systems: double-pulse light source system, detecting system, and particle seeding system as shown in Fig. 2.8. Since PIV measures only the velocity of the particles, instead of the flow itself, by comparing the displacement of each particle image illuminated by the sequential light pulses, small particles should be seeded into the flow to conduct PIV measurement technique.

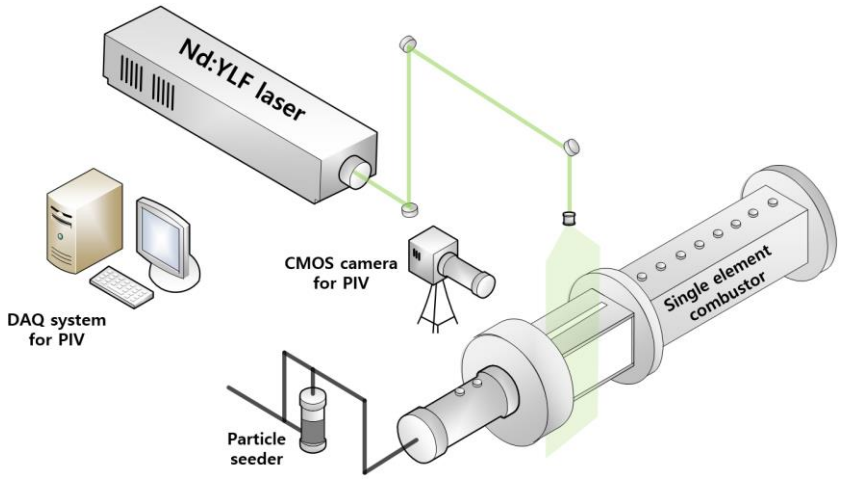

Fig. 2.8 Schematic diagram of PIV measurement system.

In this study, a double-pulse neodymium-doped yttrium lithium fluoride (Nd-YLF) laser is used as a light source and a high speed CMOS camera is employed to obtain instantaneous particle images at a measurement plane. There are no specific rules for particle seeding system; however, the size of the particle should be determined by considering whether particles can follow the flow well or not [22]. In most cases, it is necessary to add tracer particles into the flow. These particles are illuminated at the measurement plane of the flow twice times within a short interval. The scattering or fluorescence signals from particles are recorded on a single frame or sequential frames. The

displacement of the particle signals identified by the light pulses is calculated through evaluation of the PIV.

To calculate the displacement of the particles captured by a CMOS camera, it is necessary to divide the image into several grids, which are called interrogation windows. After setting the size of the interrogation window, one interrogation window of the first images is picked and compared with all the interrogation windows of the second images. The displacement between the interrogation window of the first image and the interrogation window of the second image represents one vector of the flow field. By conducting this work in all the interrogation windows, whole vectors of flow-field can be obtained. This process is called a correlation.

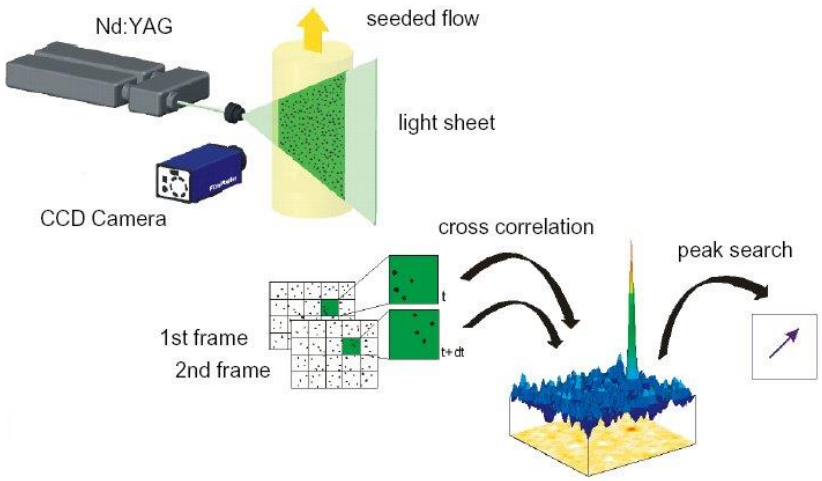

Fig. 2.9 Principle of the typical PIV system [53].

The correlation function is expressed as follows:

$$h(s_x, s_y) = \int_0^\infty \int_0^\infty f(x,y)g(x+s_x, y+s_y)dxdy \tag{2.4}$$

The expression can become simple as conducting Fourier transformation for convenience's sake in calculating. Here, *F* and *G* are Fourier transformed function of each

f and g, and they mean Fourier transform operator.

$$F(h) = F^*(f) \times F(g) = F^* \times G \tag{2.5}$$

$$h = F^{-1}(F^* \times G) \tag{2.6}$$

Equation 2.4 is the same expression of spatial masking in an image processing technique. Thus, it means that a correlation is a kind of masking concept. According to this concept, the correlation can be called a process to figure out the distribution of the similarity by signal distribution in an image plane. Equation 2.6 makes us use the fast Fourier transform (FFT) algorithm which reduces the calculation time drastically. The interrogation window size of $2n \times 2n$ should be chosen to use FFT algorithm because FFT algorithm is a method by dividing even and odd terms. However, the calculation time becomes short by log_2N/N times comparing with the direct Fourier transform (DFT) algorithm.

A correlation method is separated into auto-correlation and cross-correlation. Mathematically, auto-correlation is the case; $f(x; y) = g(x; y)$ in Eq. 2.4 and cross-correlation is the case; $f(x; y) \neq g(x; y)$. Experimentally, an auto-correlation is used for the case where the first image at $t = t_1$ and the second image at $t = t_2$ are recorded in one frame (called as a single frame/double exposure mode) and cross-correlation is used for the case where the first image at $t = t_1$ and the second image at $t = t_2$ are recorded in separated frames (called as a double frame/single exposure mode). Comparing with an auto-correlation method, a cross-correlation method has some merits as follows:

1. Directional ambiguity problem can be avoided easily.
2. The algorithm is simple because there is only one peak as a result of correlation.
3. Dynamic range is relatively large.

However, it was difficult to satisfy hardware requirements for cross-correlation. Especially, a time interval was a problem in most cases because the device, which satisfied

both high-resolution conditions and short time intervals (microsecond), was very expensive. Nowadays, it becomes relatively inexpensive and popular. Thus, most PIV systems use a cross-correlation method.

In this study, the scattering signal of seeding particles (zirconium oxide (ZrO_2) with a mean diameter of 1.5 μm) from a sheet beam of the Nd-YLF laser (Photonics, DM20-527) is measured using a CMOS camera (LaVision, HighSpeed Star 8) mounted with a Nikon lens (f = 105 mm, f/2.8) and a 527 ± 10 nm narrow bandpass filter (LaVision, 1108572 VZ). The field of view for the PIV is 95 mm × 60 mm. The time interval between the images in each PIV pair (dt) is 10 μs in Chapter 3 and 5 μs in Chapter 4. The PIV image resolution is 9.28×10^{-5} m per pixel, and the interrogation window sizes for PIV are 48 × 48 pixels and 24 × 24 pixels, in the multi-pass mode. The overlap ratio is 75%, and FFT-based cross-correlation and noise reduction are applied for post-processing. Figure 2.10 shows the field of view of OH^* chemiluminescence, OH-PLIF, and PIV measurement.

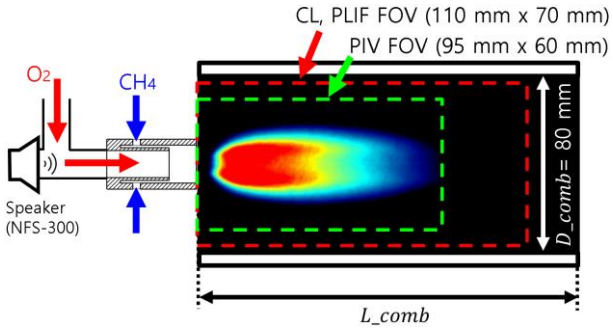

Fig. 2.10 Field of views for OH^* chemiluminescence, OH-PLIF, and PIV.

2.3 Ignition Sequence

To conduct the combustion tests in this study, initial ignition is required, thus, a torch igniter using air and hydrogen is used. The main flame is formed using oxygen and methane. In addition, air cooling is performed to prevent the quartz windows from breaking and deformation of the combustor due to high temperature during the combustion process. Figure 2.11 shows the sequence for combustion tests used in this study.

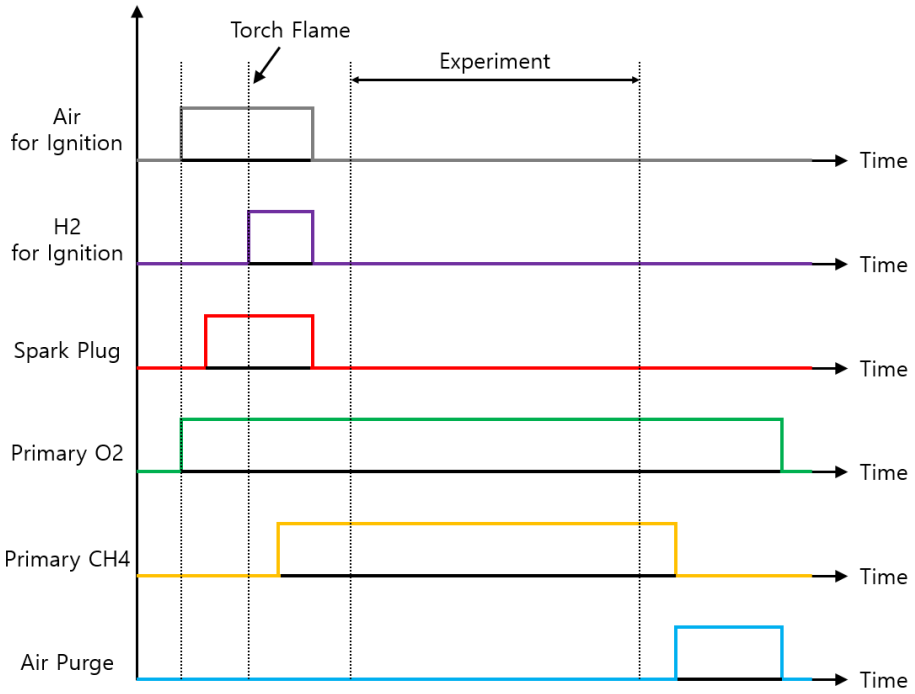

Fig. 2.11 Sequence for combustion tests including ignition.

After setting the flow rate of air for ignition and oxygen for main flame to the operating conditions, a spark plug is activated. Then, the hydrogen for ignition is supplied to ignite a torch flame. After igniting the pilot torch flame, the methane is supplied to ignite the main flame. If the methane is supplied before the torch ignition, the combustor is filled with methane, which causes an explosion at ignition by abruptly igniting the methane inside

the combustor. The combustion tests are conducted after spark plugs, ignition air, and ignition hydrogen are turned off and only the main flame is formed inside the combustor. After the combustion tests are completed, supplying the methane for main flame is turned off and the purging air is supplied to extinguish the flame. Finally, the combustion process is finished by stopping the flows of oxygen and purge air.

2.4 Flame Transfer Function Measurement

The flame inherent characteristics can be determined by measuring the FTF using Eq. (2.7), where the input function is the velocity fluctuation and the output function is the perturbation of the volume-integrated heat release rate.

$$\mathrm{FTF}(\omega) = \frac{q'/\bar{q}}{u'/\bar{u}}, \tag{2.7}$$

where ω is the modulation frequency and u is the oxygen velocity. Furthermore, x' and $\bar{x}$ are the fluctuation and average of x, respectively.

When perturbation occurs in the flame, it leads to perturbation of the heat release rate and causes an unstable flame. Figure 2.12 shows the mechanisms of heat release rate perturbations by velocity disturbances.

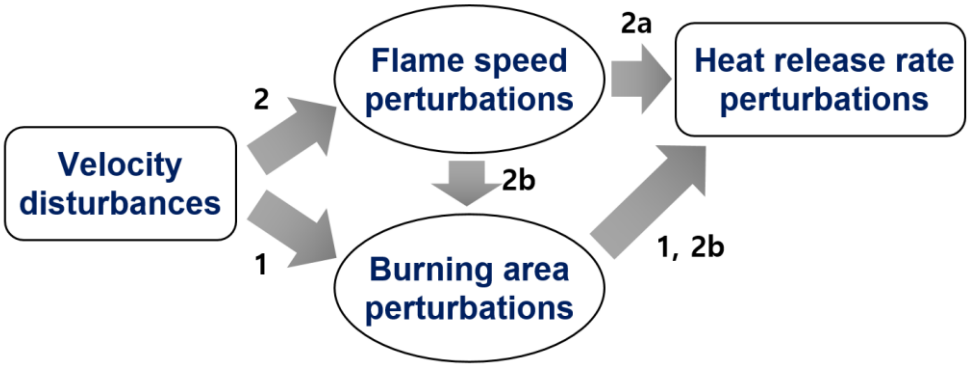

Fig. 2.12 Mechanisms of heat release rate perturbations by velocity disturbances [73].

At low frequencies, velocity disturbances cause heat release rate perturbations by changing the flame area (Route 1). However, at high frequencies, flame speed perturbations occur due to the flame stretch effect, so heat release rate perturbation is induced either directly (Route 2a) or indirectly (Route 2b).

Figure 2.13(a) shows the flame shapes according to external modulation at low and

high frequencies. For low-frequency modulation, the flame front winkles with constant amplitude from the flame base to its tip [74]. However, for high-frequency modulation, flame wrinkling is evident only at the flame base and decays downstream, and this structural difference is caused by the flame stretch effects as shown in Fig. 2.13(b) [74]. As the disturbance frequency increases, reduced Strouhal number (St_f), which represents the flame speed effect, increases, so the flame stretch effect increases. The gain of FTF can be expressed by St_f and Markstein number ($\hat{\sigma}_C$) according to the magnitude of St_f as summarized in Table. 2.3 [74].

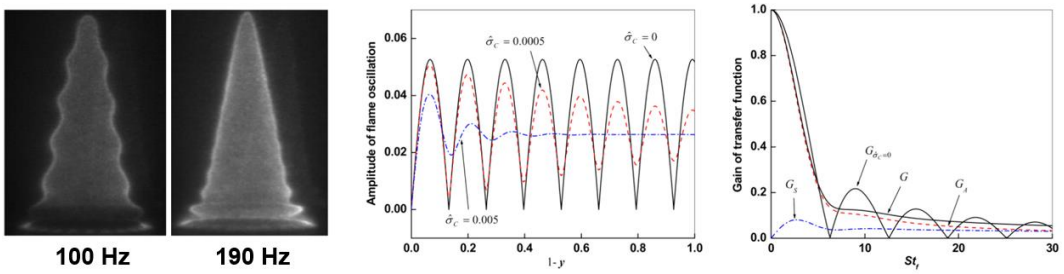

Fig. 2.13 (a) Flame shapes according to external modulation. (b) The amplitude of flame oscillation and (c) gain of FTF for different Markstein numbers ($\hat{\sigma}_C$) [74].

Table 2.3 Gain of FTF expressed by St_f and $\hat{\sigma}_C$ according to the magnitude of St_f.

St_f conditions	Stretch effect	Gain of FTF (G) [74]
$St_f \ll 1$	Non-stretch flame (flame area effect >> flame speed effect)	$\lvert G\rvert = \frac{2}{St_f}\lvert\sin(St_f/2)\rvert$
$St_f \sim O(\hat{\sigma}_c^{-1/2})$	Weak-stretch flame (flame area effect > flame speed effect)	$G \approx -\frac{1}{iSt_f}(1 - e^{-\hat{\sigma}_c St_f^2} e^{iSt_f})$
$St_f \sim O(\hat{\sigma}_c^{-1})$	Strong-stretch flame (flame area effect ≈ flame speed effect)	$G \approx -\frac{1}{iSt_f}(1 + \hat{\sigma}_c^2 St_f^2 - i\hat{\sigma}_c St_f)$

When the disturbance frequency is small, so St_f is negligibly small, the effect of the flame area on the heat release rate perturbation is dominant. Therefore, the theoretical value

of FTF gain decreases with oscillating as the disturbance frequency increases as shown in Fig. 2.13(c). However, as the disturbance frequency increases a little further, the flame stretch effect increases, so the disturbance is attenuated. Finally, when the disturbance frequency is large and the flame stretch effect becomes very large, the FTF gain decreases gradually without oscillating as shown in Fig. 2.13(c).

Commonly, three kinds of modulation devices have been used during FTF measurement experiments: the control valve, the siren, and the acoustic devices [62]. Table 2.4 shows the previously research which used various modulation devices.

Table 2.4 Summary of flow modulation device and application.

Modulation device	**Author**	**Contents**
Control valve	A.X. Sengissen	LES and experiment: 2007 [75]
	K.P. Geigle	Syngas FFT and CFD: 2007 [76]
Siren	W.S. Cheung	FTF measurement: 2003 [77]
	A. Gentemann	FTF measurement: 2004 [78]
Speaker	B. Varoquié	n-τ model for FTF of non-premixed flame: 2002 [79]
	C.O. Paschereit	Transfer matrices: 2002 [80]

Some research used a control valve [75, 76] which can generate any excitation signal. However, the range of modulation frequency, which can be generated by this type of actuators, is narrow and the maximum frequency of oscillation is low. Another option for modulation is to use a siren-like pulsator [77, 78], i.e., with a rotating part. This type of actuators can generate a high maximum frequency of oscillation, however, the geometry of pulsator should be changed to vary the strength of oscillation. Therefore, in this study, a speaker is selected for the modulation device because the frequency and strength of oscillation can be varied easily [79, 80]. Although a speaker has a disadvantage that it is hard to be used to oscillate a large flow, the flow rate of this study is sufficiently small to be modulated by a speaker. The modulation frequency of the speaker is varied up to 2000 Hz. Figure 2.14 shows the FTF measurement system.

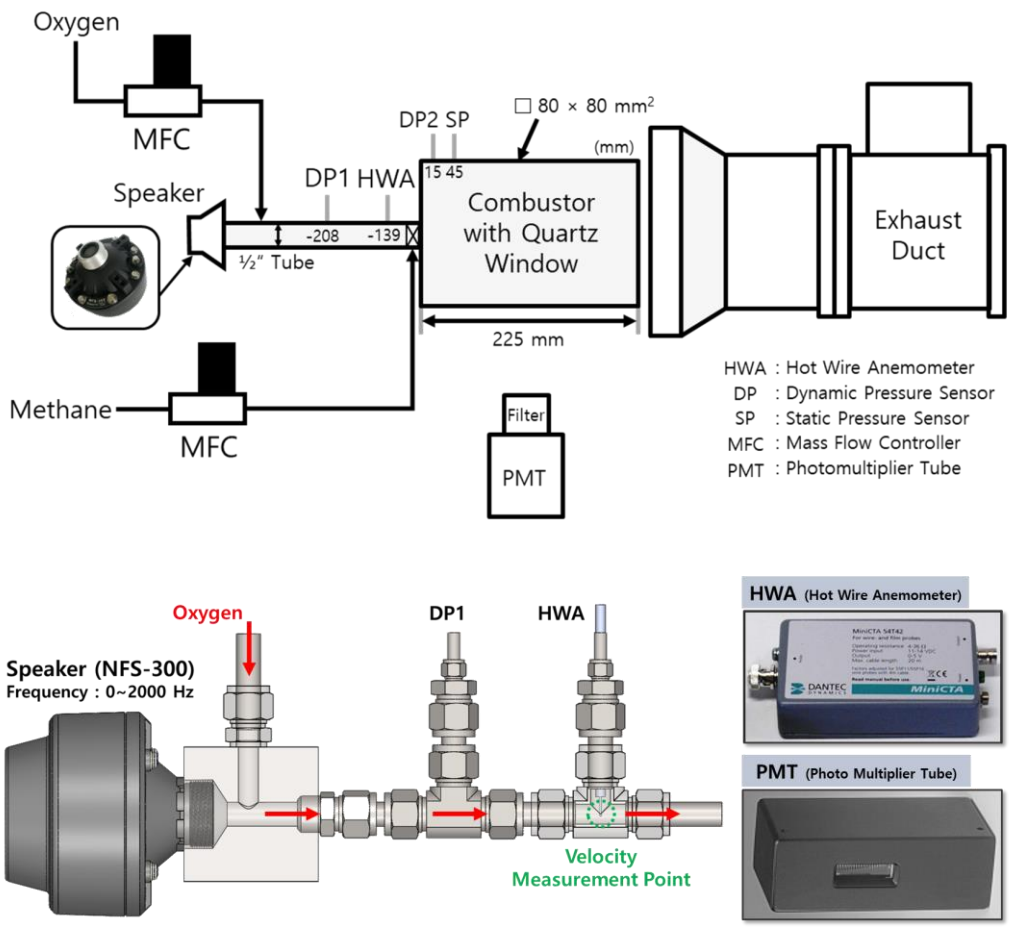

Fig. 2.14 Schematic diagram of the FTF measurement system.

In this study, the FTF is measured using a speaker (Sammi, NFS-300) mounted at the upstream of the oxygen feed line for a single frequency modulation under oxygen flow [79]. A hot wire anemometer (HWA) (Dantec, MiniCTA) is used for measuring the velocity perturbation of the oxygen flow. A PMT (Hamamatsu, H7732-10) is used for measuring the heat release perturbation under open boundary conditions without a plug nozzle and downstream combustor to remove the acoustic boundary effect of the combustor. Figure 2.15 shows the change in FTF for varied strength of velocity perturbations.

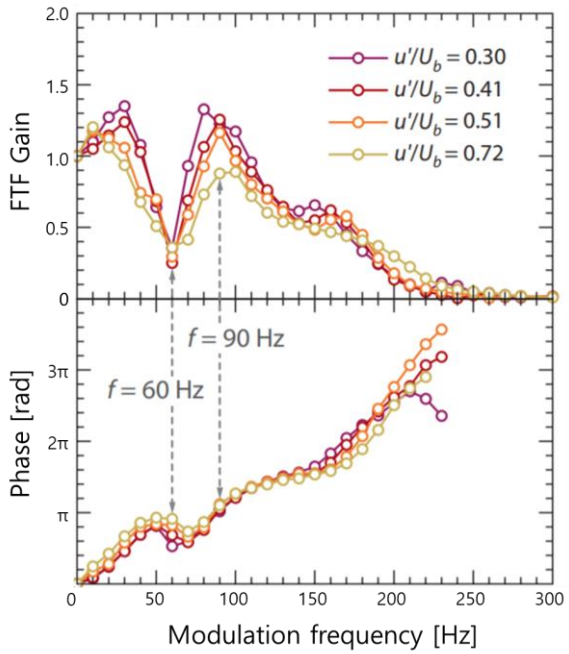

Fig. 2.15 Effect of modulation strength on FTF characteristics [48].

According to the previous research [48], the amplitude of inlet velocity perturbation is a key parameter which can change the FTF. In this study, when measuring the FTF, the amplitude of the velocity perturbation is checked in real-time, so that the voltage of speaker can be adjusted. Therefore, the velocity fluctuation in the denominator of the FTF is kept constant at 5% of the mean velocity. This 5% fluctuation is sufficiently high to provide a good signal-to-noise ratio and small enough to avoid non-linearity. Measurement data are recorded by the Labview-based data acquisition system, with a sampling rate was 10,000 samples/s.

2.5 Shear Strain Magnitude Calculation

The continuity equation of two-dimensional flow is as Eq. (2.8).

$$\frac{\partial}{\partial \mathrm{x}}(\rho u) + \frac{\partial}{\partial \mathrm{y}}(\rho v) = 0 \tag{2.8}$$

If the function $\psi(x, y)$ is defined so that Eq. (2.8) can be expressed as Eq. (2.9), Eq. (2.8) is always satisfied for the function $\psi(x, y)$.

$$\frac{\partial}{\partial \mathrm{x}}\left(\frac{\partial \psi}{\partial y}\right) + \frac{\partial}{\partial \mathrm{y}}\left(-\frac{\partial \psi}{\partial x}\right) = 0 \tag{2.9}$$

Therefore, this function $\psi(x, y)$ should be defined as Eq. (2.10) by comparing Eq. (2.8) and Eq. (2.9), which is called "stream function".

$$\rho u = \frac{\partial \psi}{\partial y}, \qquad \rho v = -\frac{\partial \psi}{\partial x} \tag{2.10}$$

In addition, the streamline of a two-dimensional flow is defined as Eq. (2.11) or (2.12).

$$\frac{dx}{u} = \frac{dy}{v} \tag{2.11}$$

$$\rho u\, dy - \rho v\, dx = 0 \tag{2.12}$$

If the stream function defined in Eq. (2.10) is applied to Eq. (2.12), the streamline of a two-dimensional flow can be expressed as Eq. (2.13).

$$\frac{\partial \psi}{\partial x} dx + \frac{\partial \psi}{\partial y} dy = 0 = d\psi \tag{2.13}$$

Therefore, since there is no change in ψ along the streamline, the streamline can be determined as a constant ψ, and the change in ψ represents the mass flow rate.

Figure 2.16 shows the schematic diagram of the shear layer under the different flow cases. When the inflow has inner and outer streams of large velocity difference with a velocity jump, the shear layer, where the inner and outer streams are mixed, grows wide as shown in Fig. 2.16(a). However, when the inner and outer streams have near-identical velocities, shear strength between the two flows is small, resulting in the thin shear layer as shown in Fig. 2.16(b). Consequently, when the velocity varies linearly, which represented that the velocity difference between two flows at the interface is almost zero, the inflow acts as a single flow.

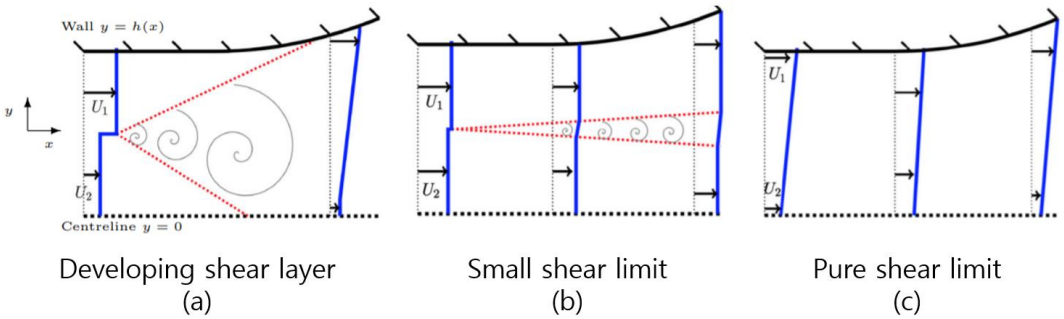

Fig. 2.16 Schematic diagram of shear layer under the different flow cases. (a) developing shear layer case with large velocity difference, (b) small shear limit case with small velocity difference, and (c) pure shear limit where the velocity varies linearly [81].

Figure 2.17 shows the details of shear layer between the inner and outer flows. The width of shear layer (δ) is defined as $\delta = h - h_1 - h_2$, where h, h_1, and h_2 are the widths of channel, outer plug flow, and inner plug flow, respectively. The shear rate (ε_y) is defined as $\varepsilon_y = (U_1 - U_2)/\delta$.

Therefore, in Fig. 2.16(a), since the large velocity difference between two streams results in strong ε_y, the shear layer grows fast. However, in Fig. 2.16(b) and 2.16(c), the velocity differences between the two streams are small, so thin shear layers form and they grow slowly.

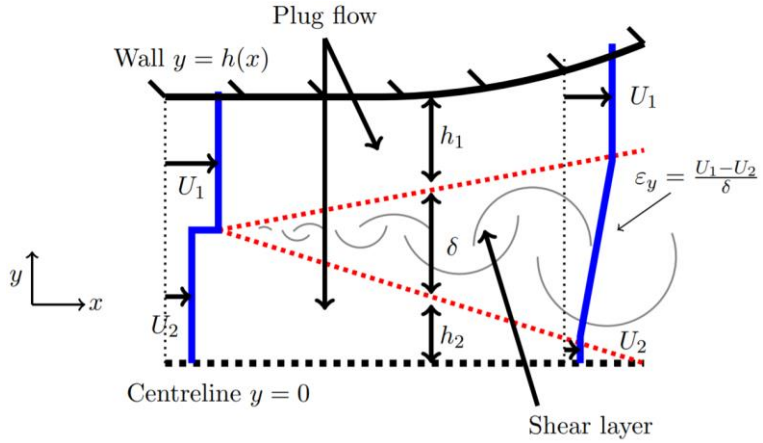

Fig. 2.17 Schematic diagram of symmetric flow in a half channel [81].

To determine the mixing strength between oxygen and methane for different flame shapes, the shear strain magnitude ($\varepsilon_{xy,max}$) is calculated using the velocity gradient (∇V) measured by PIV:

$$\nabla \mathrm{V} = \begin{bmatrix} \frac{\partial v_x}{\partial x} & \frac{\partial v_x}{\partial y} \\ \frac{\partial v_y}{\partial x} & \frac{\partial v_y}{\partial y} \end{bmatrix} = \begin{bmatrix} \frac{\partial^2 \psi}{\partial x \partial y} & \frac{\partial^2 \psi}{\partial y^2} \\ -\frac{\partial^2 \psi}{\partial x^2} & -\frac{\partial^2 \psi}{\partial y \partial x} \end{bmatrix}, \tag{2.14}$$

where V is the velocity vector measured using PIV; v_x and v_y are the velocities along the x- and y-axes, respectively; and ψ is the stream function.

Here, ∇V includes two tensors: a symmetric tensor ($S_{i,j}$, strain tensor) and an anti-symmetric tensor ($\Omega_{i,j}$, rotation tensor) [82, 83] as

$$S_{i,j} = \frac{1}{2}\left(\frac{\partial v_i}{\partial x_j} + \frac{\partial v_j}{\partial x_i}\right), \tag{2.15}$$

$$\Omega_{i,j} = \frac{1}{2}\left(\frac{\partial v_i}{\partial x_j} - \frac{\partial v_j}{\partial x_i}\right), \tag{2.16}$$

where i and $j \in \{x, y\}$.

Therefore, ∇V can be described as:

$$\nabla V = \begin{bmatrix} \frac{\partial^2\psi}{\partial x\partial y} & \frac{1}{2}\left(\frac{\partial^2\psi}{\partial y^2} - \frac{\partial^2\psi}{\partial x^2}\right) \\ \frac{1}{2}\left(\frac{\partial^2\psi}{\partial y^2} - \frac{\partial^2\psi}{\partial x^2}\right) & -\frac{\partial^2\psi}{\partial y\partial x} \end{bmatrix} + \begin{bmatrix} 0 & \frac{1}{2}\left(\frac{\partial^2\psi}{\partial y^2} + \frac{\partial^2\psi}{\partial x^2}\right) \\ -\frac{1}{2}\left(\frac{\partial^2\psi}{\partial y^2} + \frac{\partial^2\psi}{\partial x^2}\right) & 0 \end{bmatrix} \quad (2.17)$$

The principal strain rates ($\dot{\varepsilon}_1$ and $\dot{\varepsilon}_2$) can then be calculated by Eq. (2.18) [83], which are the eigenvalues of $S_{i,j}$.

$$\dot{\varepsilon}_1 \text{ and } \dot{\varepsilon}_2 = \frac{\dot{\varepsilon}_{xx} + \dot{\varepsilon}_{yy}}{2} \pm \sqrt{\left(\frac{\dot{\varepsilon}_{xx} - \dot{\varepsilon}_{yy}}{2}\right)^2 + \dot{\varepsilon}_{xy}^2}, \quad (2.18)$$

where $\dot{\varepsilon}_{ij} = \frac{\partial v_i}{\partial x_j}$.

Therefore, the shear strain magnitude ($\varepsilon_{xy,max}$) can be expressed as [83]:

$$\varepsilon_{xy,max} = \sqrt{\left(\frac{\dot{\varepsilon}_{xx} - \dot{\varepsilon}_{yy}}{2}\right)^2 + \dot{\varepsilon}_{xy}^2} \quad (2.19)$$

In this study, the $\varepsilon_{xy,max}$ is calculated from the injector exit to near the flame base, as shown in Fig. 2.18.

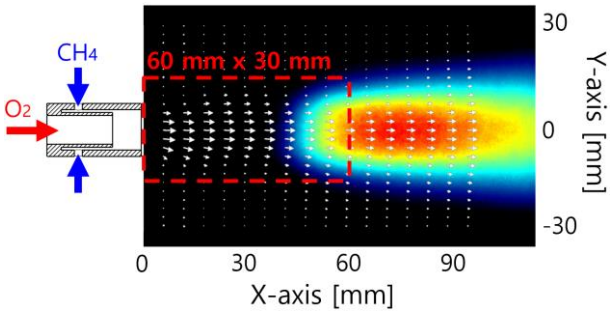

Fig. 2.18 Area used for calculating the shear strain magnitude ($\varepsilon_{xy,max}$).

2.6 Continuous Wavelet Transform

When analyzing a signal of dynamic characteristics varying over time, such as transient phenomena, using a Fourier transform (FT) is possible to check only whether a modulation at a particular frequency has occurred, but not to analyze the frequency change over time. Therefore, short term Fourier transform (STFT) and wavelet transform (WT) are used to compensate for this limitation. STFT is a method of performing FT analysis after dividing a long signal, varying over time, into several short time signals. However, as reducing the signal length, the time resolution increases, but the frequency resolution decreases. Therefore, WT is used to solve these limitations. WT analyzes the frequency and magnitude of the signal at each time by finding the optimal conversion condition with varying the scale and position of the wavelet for simulating the signal. The WT can be categorized into a continuous wavelet transform (CWT) and a discrete wavelet transform (DWT) according to a difference in a method for determining a scale parameter. Since CWT analyzes with a finer sampling of scales than DWT, it can exhibit better analysis results of vibration characteristics than DWT.

The continuous wavelet transform is developed as an alternative approach to the STFT to overcome the resolution problem [84]. The wavelet analysis is done in a similar way to the STFT analysis, in the sense that the signal is multiplied with a function, with the wavelet, similar to the window function in the STFT, and the transform is computed separately for different segments of time-domain signal [84].

$$C\big(a,b;\ f(t),\Psi(t)\big) = \int_{-\infty}^{\infty} f(t)\frac{1}{a}\Psi^{*}\left(\frac{t-b}{a}\right)dt\,, \tag{2.20}$$

where *C(a, b)* is the CWT coefficient, *a* is the scale parameter, *b* is the position parameter, Ψ is a wavelet which is called the mother wavelet, and * denotes the complex conjugate.

In multiplying the wavelet, if the signal has a spectral component corresponding to the value *a*, the product of the wavelet at that position provides a relatively large value. Especially, in the transition process, such as sudden changes in flame shapes, perturbations

corresponding to a particular frequency occur and disappear in a very short time. In such cases, if the analysis is performed using a typical FT, the magnitude of the corresponding perturbation for the total time becomes smaller, making it difficult to distinguish from the noise and to determine when such perturbation occurs. Therefore, CWT is the most appropriate method to analyze the dynamic characteristics that occur and then disappear in a very short time or the dynamic characteristics that vary over time. By applying the CWT, it is very important to select the proper wavelet to perform an accurate analysis. Figure 2.19 shows the changes in CWT results according to wavelets.

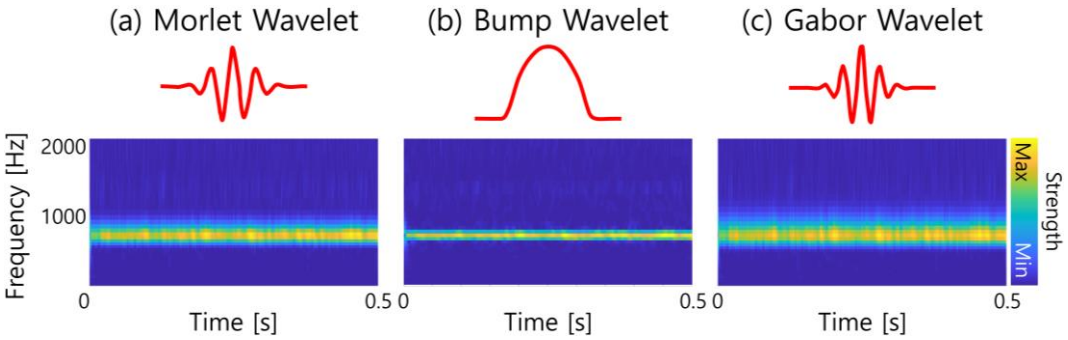

Fig. 2.19 Change in CWT results according to wavelets; (a) Morlet wavelet, (b) bump wavelet, and (c) Gabor wavelet.

The ‘Morlet’, ‘bump’, and ‘Gabor’ wavelets are used to compare the CWT results from the same input data. The ‘bump’ wavelet shows the highest resolution of frequency analysis, thus it is selected as the wavelet for CWT in this study. Therefore, in this study, the CWT, by bump wavelet, is applied for dynamic pressure signals to explore both the time and frequency domain characteristics.

2.7 Instability Prediction by 1D Lumped Network Model

The most serious problem with rocket engines is the combustion instability, which arises because the pressure perturbation inside the combustion chamber is greatly amplified due to the interaction between the pressure perturbation and the heat release rate perturbation inside the combustion chamber. Combustion instability can interfere with mission success by causing abnormal thrust or, more seriously, an engine explosion [85, 86]. Therefore, it is very important to understand the characteristics of combustion instability during the engine development. To determine the conditions for combustion instability experimentally, it takes a long time because the combustion tests should be conducted in the real combustor. Furthermore, if the explosion occurs by combustion instability, the engine should be re-manufactured, which resulted in a cost problem. Therefore, if the combustion instability can be predicted and explored, it is possible to design a very stable combustion system from combustion instability in advance. In addition, using the predicted characteristics of combustion instability, it is possible to control the operating condition to reduce the combustion instability during the operation. In order to predict the combustion instability, various attempts have been made. The lower order model [87], the direct method (RANS, LES) [88], the linearized equations in time domain [89] and the Helmholtz solver [90] have been studied to predict the combustion instability [62]. One example of predicting the combustion instability is to use OSCILOS (an open source combustion instability low order simulator; http://www.oscilos.com/) which is based on the 1D lumped network method.

OSCILOS is a code developed by the A.S. Morgans in Imperial College London to predict combustion instability in the frequency domain and time domain. The OSCILOS analysis was carried out through the CFD based FTF and the combustor geometry information, and it was confirmed that the instability frequency was successfully predicted [87]. OSCILOS identifies the characteristics of combustion instability by using combustor geometry information, thermal properties, flame characteristics, and boundary conditions of the combustor. The FTFs are measured experimentally under each condition and the

flame locations are also defined based on the flame and flow diagnostics results. For the boundary condition, the prediction analysis is conducted by assuming that the inlet and outlet are set as the open and closed boundary, respectively. In this analysis, only the longitudinal acoustic waves in the 1D plane are considered assuming that the radial perturbation is very small compared to the longitudinal perturbation. Furthermore, each combustion chamber is divided into a module and the continuity condition of each module boundary is considered using governing equation [87].

CHAPTER 3

CHARACTERISTICS OF FLAME SHAPES

3.1 Background and Objectives

Because the flame shape is a key parameter in determining combustion characteristics [91-93], several studies [91-96] have investigated the flame shape, flame characteristics, and their dependence on operating conditions. Typical flame shapes of non-premixed flames include detached and attached flames. The root of the flame is not anchored to the injector exit for a detached flame, while it is anchored to the injector exit for an attached flame. These have distinct static and dynamic stability characteristics. Moore and Kuo [92] and Moore et al. [93] showed that an increasing fuel-jet Reynolds number, from the annular region of a coaxial injector, produced a transition from an attached stable flame to a detached flame state with oscillations. Furthermore, in lean premixed pre-vaporized combustors with twin annular premixing swirlers, the main flame is anchored by a smaller non-premixed pilot flame, and for certain off-design conditions, this anchoring is unsteady, possibly causing combustion instability [97, 98]. In addition, the flame shape has been used to define the delay time between p' and q' inside the combustor [85], which subsequently determines whether combustion instability occurs [99, 100].

In previous studies on combustion characteristics, flame and combustion stabilities were assessed using the equivalence ratio [101] or O/F ratio [102]. However, the swirling flows commonly used to support flame stabilization feature several types of vortex breakdowns and frequently exhibit bifurcation, where a flame transition may occur spontaneously between different co-existing states, such as attached and detached, even under constant conditions [103, 104]. Such a flame is called a bistable flame. Consequently, it is impossible to determine combustion stability from only the O/F ratio, without also measuring the flame shape. Therefore, this study aims to improve combustion stability by identifying the causes of bifurcation and transition between flame shapes, which exhibit

distinct combustion characteristics despite existing under constant operating conditions.

Tay-Wo-Chong and Polifke [105] investigated how the thermal wall boundary condition and combustor confinement impact FTFs for different flames in a perfectly premixed axial swirl burner, using LES. They showed that the two flame states had different flow fields and FTFs, yielding distinct stability characteristics. Previous studies [106-108] have experimentally explored precessing vortex core (PVC) occurrence during transitions between premixed V-shaped and M-shaped flames. Furthermore, the shape of a lean premixed flame has been varied depending on the type of shear layer where the flame occurs. Above a critical equivalence ratio, the flame kernel was found to expand to the outer recirculation zone (ORZ) and ignite the entire ORZ reactant region, resulting in flame shape transition [109]. Hermeth et al. [104] studied the bifurcation characteristics of bistable flames by varying the pilot fuel flow rate and acoustic perturbation strength, using LES in a lean swirl-stabilized gas turbine burner. They found an important relationship between flame states and thermoacoustic instabilities, where changes from one flame state to the other subsequently change the acoustic stability [104]. However, bifurcations of bistable flames have not yet been investigated sufficiently, despite engineers reporting their prevalence. Furthermore, LES-based studies [104, 105] have revealed a lack of sufficient experimental data to validate LES results, and only a limited range of acoustic perturbation strengths has been used [104] to investigate flame bifurcation thus far. Some works in the Swiss Federal Institute of Technology in Zurich (ETH Zürich) [110, 111] have explored thermoacoustic bistability in a lab-scale turbulent combustor at atmospheric pressure and attributed the bistable region to an amplitude-dependent phase difference and inertia effects. Additionally, studies done at the Indian Institutes of Technology (IITs) [112, 113] on the bifurcation of ducted laminar premixed flames found that the nonlinear interactions between combustion and acoustics caused bifurcations in the pressure oscillations characteristics. In addition, Bennewitz et al. [114, 115] reported the possibility that external acoustic modulation could reduce the combustion instability through the analytical and experimental approach.

Although the effects of fuel staging [116] and airflow modulation [117] on non-

premixed flame shapes have been recently investigated experimentally, only the transition from one state of flames (detached or attached flames) has been considered, and transition from the other state has not been studied. Furthermore, the modulation strength and the change in flame shapes under the transition owing to the modulation have not been measured, and the effects of the O/F ratio and velocity difference between oxidizer and fuel (ΔV) have not been considered. So, the bistable characteristics of non-premixed flames, which are primarily used in most propulsion systems with coaxial injectors, have not been sufficiently explored. Therefore, this study experimentally investigates the characteristics of non-premixed methane-oxygen flame shapes, formed by a recessed coaxial injector at the lab-scale single element combustor.

3.2 Experimental Methods

The atmospheric single element combustor used in this study is shown in Fig. 3.1. The square cross-section of the combustor is 80 × 80 mm^2 and quartz windows are employed on the sidewalls for optical access. The downstream of the combustor is set as an open boundary condition. Acoustic perturbations are applied with a speaker (Sammi, NFS-300) for single frequency modulation under oxygen flow. The overall schematic of the injector used in this study is provided in Figs. 2.2(b-d) and 2.10.

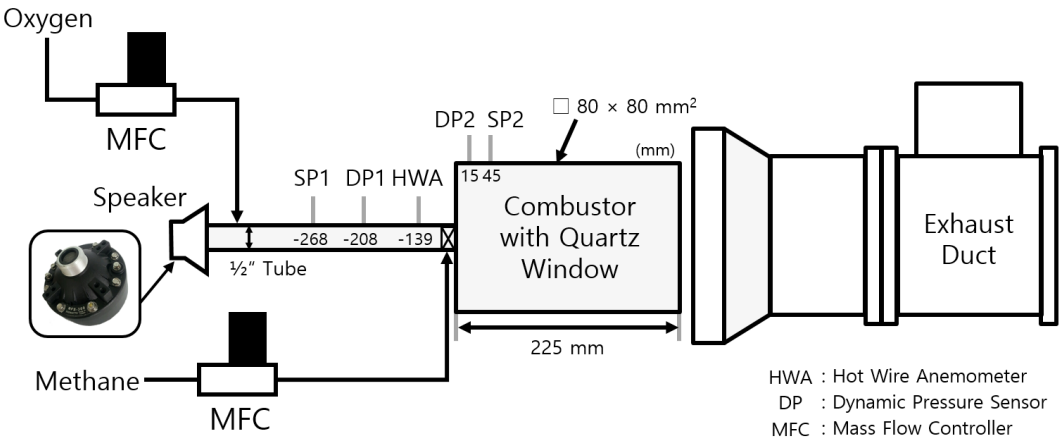

Fig. 3.1 Schematic of the single element combustor with acoustic modulation device.

Gaseous oxygen (O_2, 50 slpm, purity > 99.9 mol%) and gaseous methane (CH_4, 6–35 slpm, purity > 99.95 mol%) at 290 ± 5 K are supplied by a MFC (LineTech, M3300V, uncertainty = ± 1% of full range) through a center jet and an annular swirled jet, respectively. The reference attached and detached flames are formed under a constant condition (reference condition: $\dot{V}_{O_2}$ = 50 slpm, $\dot{V}_{CH_4}$ = 35 slpm). Two static pressure sensors (SP) (VALCOM, VPRQ-A5-5bar, uncertainty = ± 0.8%) and two dynamic pressure sensors (DP) (PCB, 102A05, uncertainty = ± 1%) are used to measure the static pressure and the pressure perturbation, respectively, at both the inlet and inside the combustor, at 10 kHz rates. The CMOS camera signals are measured along with the pressure signals so that the pressure

corresponding to each OH-PLIF and OH^* chemiluminescence images can be identified. The time interval between the images in each PIV pair (dt) is 10 μs. Direct images are obtained using a digital single-lens reflex (DSLR) camera (Canon, EOS 7D).

In this study, the effects of O/F ratio and acoustic modulation strength are investigated. For the O/F ratio variation tests, the oxygen flow rate is fixed as 50 slpm while the methane flow rate decreases from 35 to 6 slpm for increasing the O/F ratio from 2.85 to 16.6. For the acoustic modulation strength variation tests, the oxygen and methane flow rates are fixed as 50 and 35 slpm, respectively. The frequency of acoustic modulation is 200 Hz, and the strength ($u'_{ox}/\bar{u}_{ox}$), which represents the strength of oxygen velocity perturbations (u'_{ox}) relative to the average velocity ($\bar{u}_{ox}$) inside the oxygen feed line, is varied from 0 to 100%. The detailed test conditions of this chapter are summarized in the Table 3.1.

Table 3.1 Summary of the bistable flame test conditions.

Parameters	**O/F ratio**	**Acoustic modulation strength**	**Unit**
Combustor exit condition	Open end		-
Oxygen flow rate (Bulk velocity at injector exit)	50 (42.4)		slpm (m/s)
Methane flow rate (Bulk velocity at injector exit)	6 ~ 35 (9.8 ~ 57.1)	35 (57.1)	slpm (m/s)
O/F ratio	2.85 ~ 16.6	2.85	-
Inlet temperature	290		K
Oxygen Reynolds number	13,280		-
Methane Reynolds number	3,989 ~ 23,268	23,268	-
Modulation Frequency	-	200	Hz
Modulation strength ($u'_{ox}/\bar{u}_{ox}$)	-	0 ~ 100	%

3.3 Shapes of Methane-Oxygen Flame

Despite the constant volume flow rates of oxygen and methane, $\dot{V}_{O_2}$ = 50 slpm and $\dot{V}_{CH_4}$ = 35 slpm, respectively, used in this work, both attached and detached flames are formed. Direct, OH-PLIF, and PIV images of each flame shape are shown in Fig. 3.2. The attached and detached flames are defined as being attached to and lifted off, though not blown off, from the injector rim, respectively.

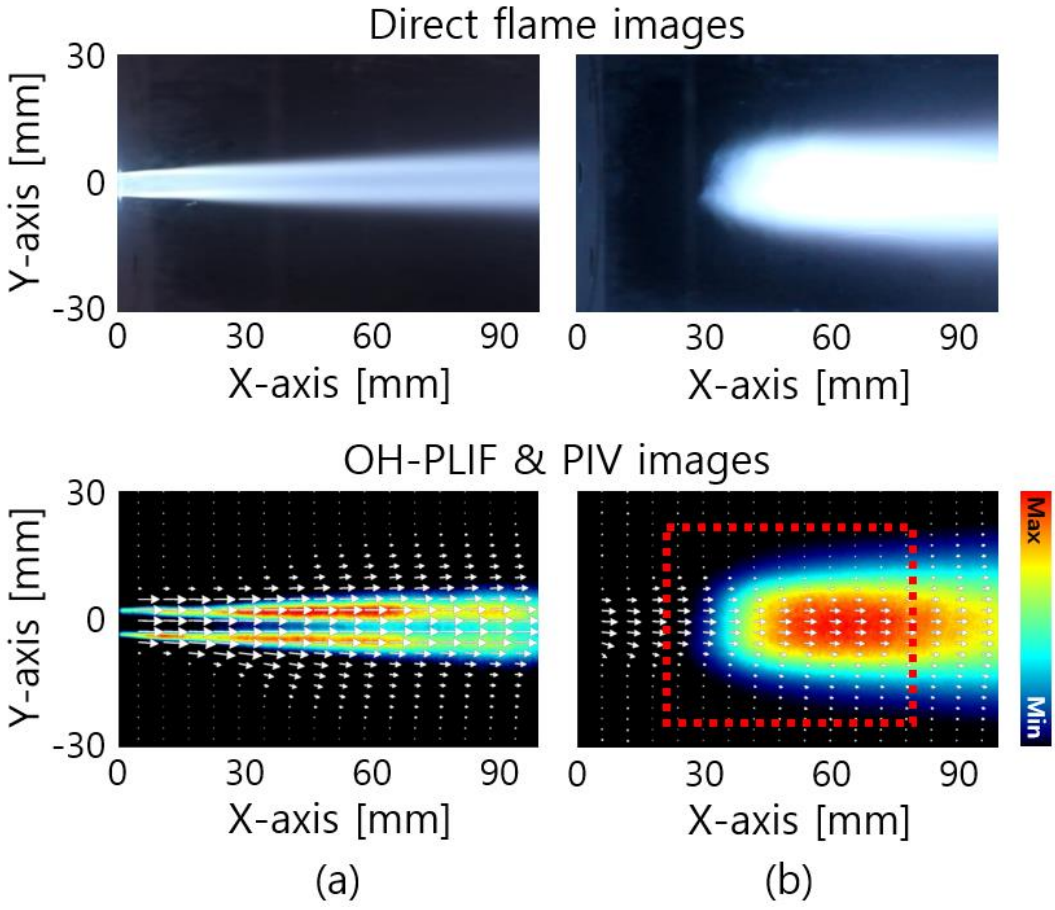

Fig. 3.2 Bistable flame shapes of the (a) attached and (b) detached flame for the reference case, with O/F ratio = 2.85, $\dot{V}_{O_2}$ = 50 slpm, and $\dot{V}_{CH_4}$ = 35 slpm. Top row: direct images. Bottom row: time-averaged OH-PLIF and PIV images.

The root mean squares (RMS) and the peak value of the pressure were 1.75 and 10.4 times stronger, respectively, in the detached flame than those in the attached flame, representing more significant pressure perturbations, p'. Additionally, both average and RMS of the OH^* chemiluminescence intensities, measured by the PMT, were 2.71 times stronger in the detached flame than those in the attached flame, representing more significant heat release rate perturbations, q'. Thus, in the present study, the attached flame was considered stable, with weak pressure and heat release perturbations, p' and q', while the detached flame was considered unstable, with strong p' and q' despite constant flow conditions as shown in Fig. 3.3. The dominant frequency of these perturbations under the detached flame, without external modulation, was measured to be 830 Hz.

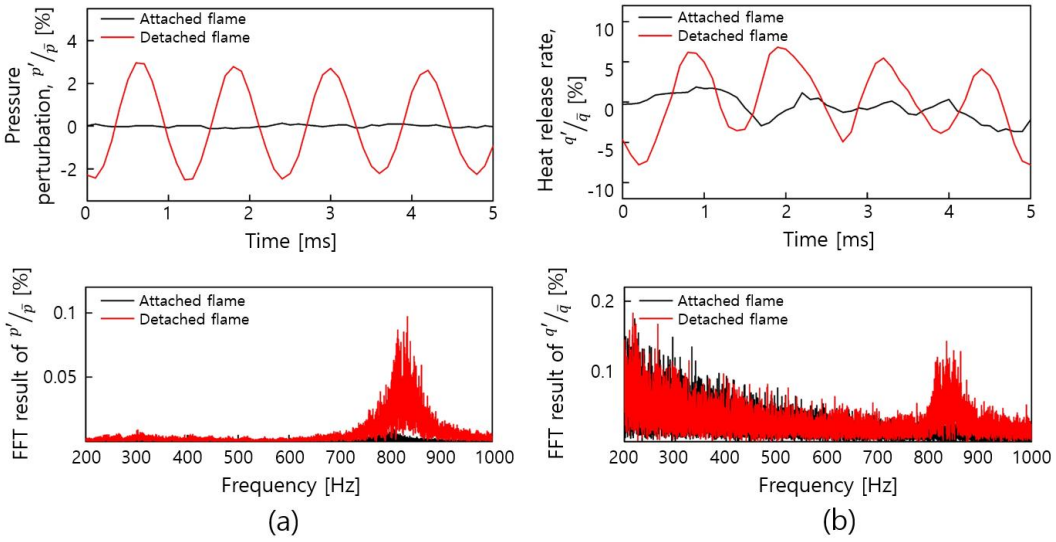

Fig. 3.3 Time-series data and FFT results for (a) pressure and (b) heat release rate corresponding to both attached and detached flames.

Figures 3.4(a) and 3.4(b) show the methane velocity at the methane feed line when the attached and detached flames are formed, respectively. During the ignition process, the attached and detached flames are formed randomly despite the constant ignition condition. As shown in Fig. 3.4, the tendency of the initial increase in the methane flow rate supplied

by the MFC, when the main flame is formed, is measured to identify the difference in the process of flame formation. If $\dot{V}_{CH_4}$ was gradually increased initially by the MFC, an attached flame was formed initially under the high O/F ratio and then transitioned into the reference attached condition (Fig. 3.4(a)). However, if $\dot{V}_{CH_4}$ was rapidly increased, the detached flame was initially formed at a low O/F ratio and then transitioned into the reference detached condition (Fig. 3.4(b)). The difference in flame shape according to O/F ratio will be discussed in Chapter 3.4. Furthermore, the tendency of forming an attached flame increased after conducting the long-term combustion test. In other words, the thermal conditions of injector rim might impact the formation of bistable flames.

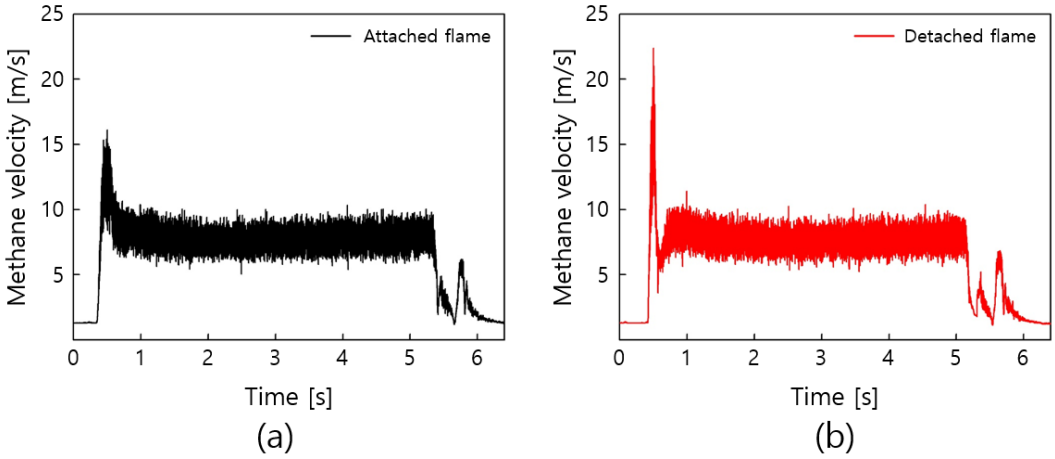

Fig. 3.4 Flow velocity at the methane feed line for (a) attached and (b) detached flames.

Figures 3.5(a) and 3.5(b) show the instantaneous and phase-averaged OH^* chemiluminescence images, respectively, of the detached flame without external modulation, and Fig. 3.5(c) provides the spatially-integrated OH^* intensity spectrum along the Y-axis in Fig. 3.5(b).

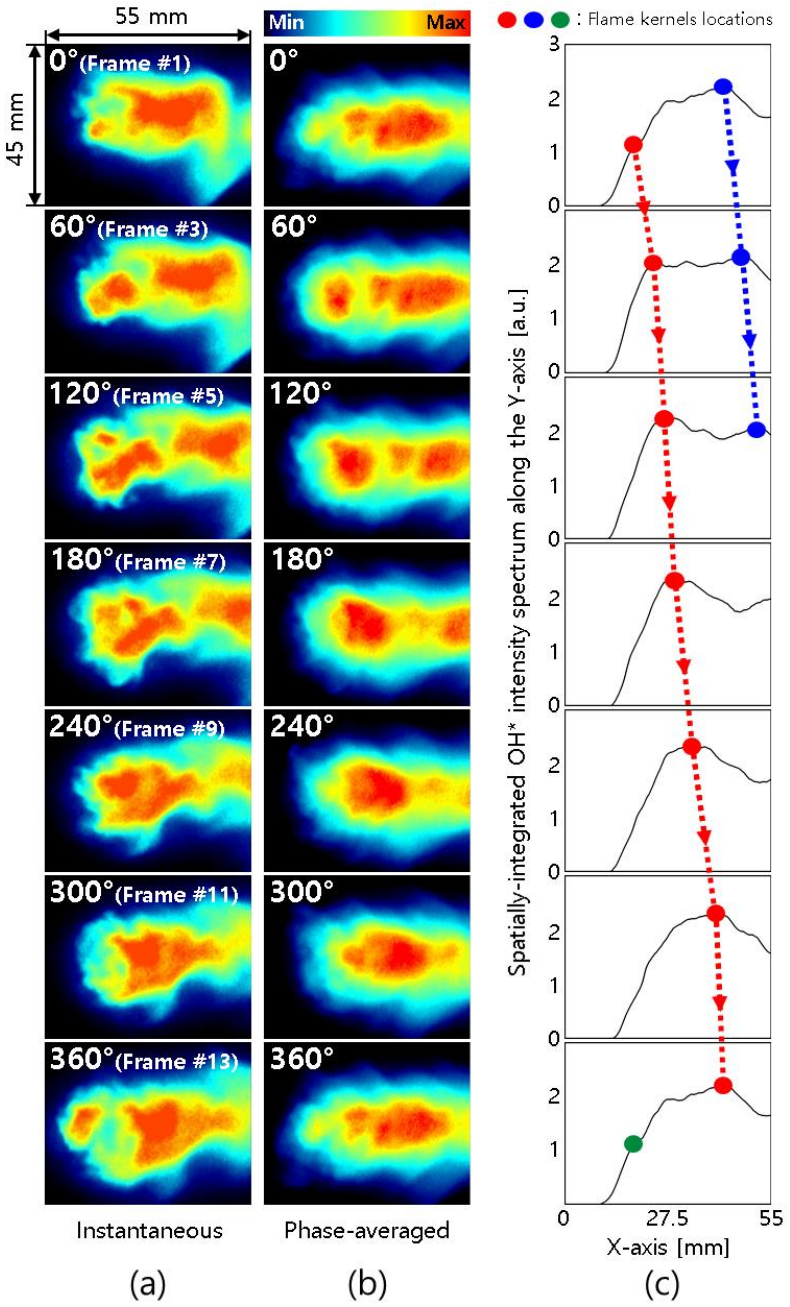

Fig. 3.5 (a) Instantaneous and (b) phase-averaged OH^* chemiluminescence signals obtained near the base of the detached flame in the red-dashed box (55 mm × 45 mm) denoted in Fig. 3.2(b). (c) Spatially-integrated OH^* intensity spectrum along the Y-axis of Fig. 3.5(b).

According to the Figs. 3.5(a) and 3.5(b), the flame kernel was formed at the flame base which was determined by OH-PLIF, and it propagated to the downstream with increasing the size. The flame kernel propagation could be also identified by Fig. 3.5(c) where the location of flame kernel was denoted by the colored circle: blue, red, and green circles are the previous, present, and new flame kernel, respectively. Clearly, one cycle of flame kernel formation and propagation covered 12 frames, representing 833.33 Hz cycles and coinciding with the perturbation frequencies of pressure and heat release rate as shown in Fig. 3.3. Thus, the flame shape variation could be attributed to the perturbations of pressure and heat release rate.

Figure 3.6 shows the temperatures and perturbation frequencies with varying the $\dot{V}_{O_2}$ or $\dot{V}_{CH_4}$, respectively, while keeping the other flow rate constant. As shown in Fig. 3.6(a), when the $\dot{V}_{O_2}$ was constant, the temperature decreased as increasing the O/F ratio owing to an decrease in the total amount of heat input, which caused an decrease in the perturbation frequency (red triangle) as shown in Fig. 3.6(b). Conversely, with varying the $\dot{V}_{O_2}$ when $\dot{V}_{CH_4}$ was constant, the temperature was highest at O/F ratio = 4 (stoichiometry) and then the temperature decreased slightly as the total flow rate increased owing to the constant heat input as shown in Fig. 3.6(c). Therefore, the perturbation frequency (red triangle) was almost constant or slightly decreased as shown in Fig. 3.6(d).

Because the temperature was measured near the wall of the combustor, there would have been a difference from the actual temperature inside the combustor. Therefore, there was a difference between the measured frequency of the pressure perturbation (red triangle) and the calculated resonant frequency using measured temperature (black circle) as shown in Fig. 3.6(b) and 3.6(d). To correct this, the temperature was modified by adding a value obtained by multiplying the temperature difference between the measured temperature and room temperature by a particular constant which was selected by the least square method to minimize the error. The resonant frequency calculated using the modified temperature (blue square) was similar to the measured perturbation frequency (red triangle) in both cases. As a result, it is confirmed that the perturbation frequency inside the combustor

coincides with the resonant frequency of the combustor.

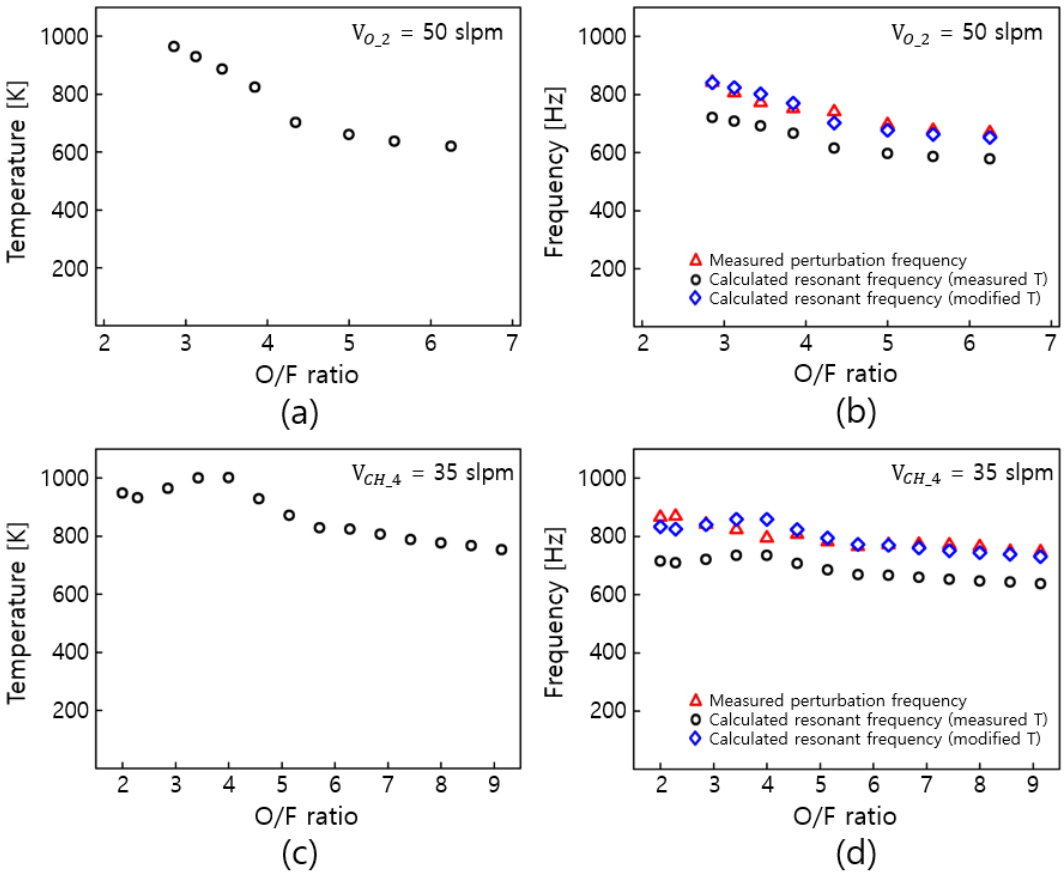

Fig. 3.6. Variation in (a), (c) temperature and (b), (d) frequency with varying the O/F ratio while keeping oxygen or methane flow rate constant, respectively.

3.4 Bifurcation due to O/F Ratio Variation

Structural changes in the flames resulting from increased O/F ratios are investigated by decreasing the methane flow rate from the level used in the reference bistable flames shown in Fig. 3.2. As shown in Fig. 3.7(a), the attached flame was maintained its state of attachment to the injector rim owing to the low-speed recirculation zone on the oxygen post tip despite these changes to the O/F ratio, but the detached flame underwent a flame shape transition and became anchored for O/F ratios above 6.23. Figure 3.7(b) shows a bifurcation diagram for the pressure perturbation inside the combustor according to the O/F ratio.

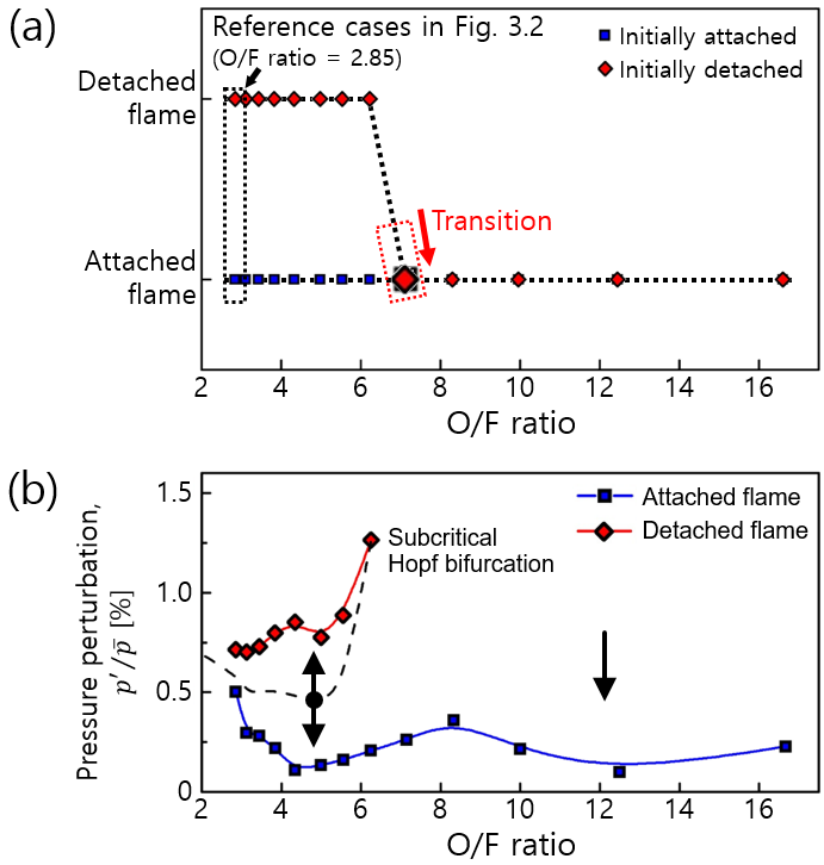

Fig. 3.7 (a) Variation of flame shape and (b) bifurcation diagram based on pressure perturbation for varied O/F ratios with $\dot{V}_{O_2}$ = 50 slpm.

In the case of the attached flame, the bifurcation characteristics did not occur because the magnitude of the pressure fluctuation inside the combustor continuously changed with varying the O/F ratio. However, in the case of a detached flame, the pressure perturbation continuously changed up to the O/F ratio of 6.23, but after that, as the flame shape was rapidly changed, the pressure perturbation also rapidly changed, which represented a subcritical Hopf bifurcation.

Since the injector used in this study has a 5 mm recess, it is not possible to measure the velocity of the two flows at the exit of oxygen post where oxygen and methane meet. Therefore, using a non-recessed injector with an increased length of the oxygen post, the flow velocities of oxygen and methane at the injector exit are measured through PIV to infer the velocities inside the recess. Figure 3.8(a) shows the ΔV calculated by subtracting the methane velocity from oxygen velocity, which are measured respectively via independent PIV according to the O/F ratio.

In the coaxial injector used in this study, the flow velocities of oxygen and methane are near equal when the O/F ratio is 4; thus, ΔV increases as the O/F ratio deviates from 4. As shown in Fig. 3.8(b), larger ΔV values can cause stronger mixing between oxygen and methane in the inner shear layer, which can cause strong turbulent mixing [118] and subsequently produce the flammable condition, where a flame can form. Furthermore, according to previous research [119], an increased ΔV between two streams causes the shear layer to spread more rapidly into the low-speed region, and the growth rate of the shear layer increases linearly with ΔV. As shown in Fig. 3.8(c), the flame base was pulled towards the injector as the ΔV increased, which might be attributed to increased mixing strength. Therefore, the transition from a detached to attached flame, denoted as the D-A transition, occurred when $\Delta V > 20$ m/s.

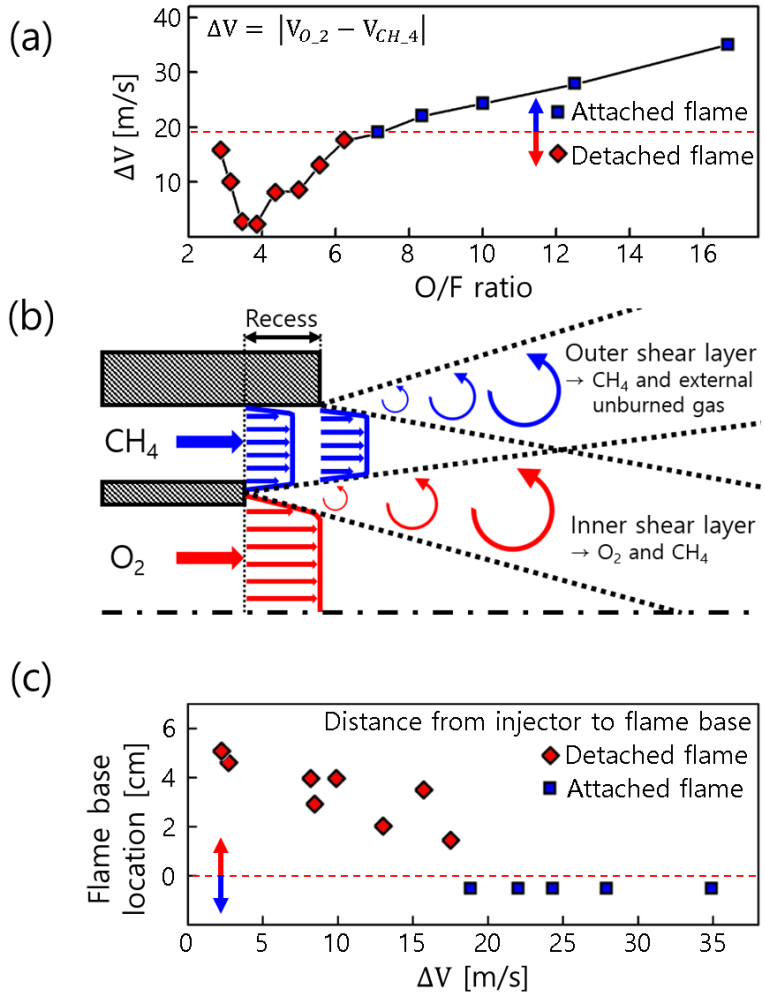

Fig. 3.8 (a) Velocity difference between oxygen and methane for varied O/F ratios with $\dot{V}_{O_2}$ = 50 slpm. (b) Schematic of mixing regimes in the coaxial injector adapted from the previous study [120] and (c) flame base location for varied ΔV with $\dot{V}_{O_2}$ = 50 slpm.

To determine the mixing strength between oxygen and methane for different flame shapes, the $\varepsilon_{xy,max}$ is calculated using the velocity gradient measured by PIV (these calculations are discussed in Chapter 2.5). Figures 3.9(a) and 3.9(b) show the time-averaged 2D $\varepsilon_{xy,max}$ and spatially-integrated $\varepsilon_{xy,max}$ spectrum along the Y-axis of the

attached and detached reference flames, respectively, in the red-dashed box denoted in Fig. 2.18. For the attached flame in Fig. 3.9(a), the shear strength near the injector exit was maximal, promoting strong mixing between oxygen and methane [118], increasing the chemical reaction rate [100, 121], and thus enabling the flame to form near the injector exit, producing an attached flame. However, for the detached flame in Fig. 3.9(b), the shear strength near the injector exit was small, and the shear strength was distributed until the flame formed. The mixing between methane and oxygen at the injector exit was insufficient for flame formation; thus, it formed in the middle of the combustor, away from the injector exit.

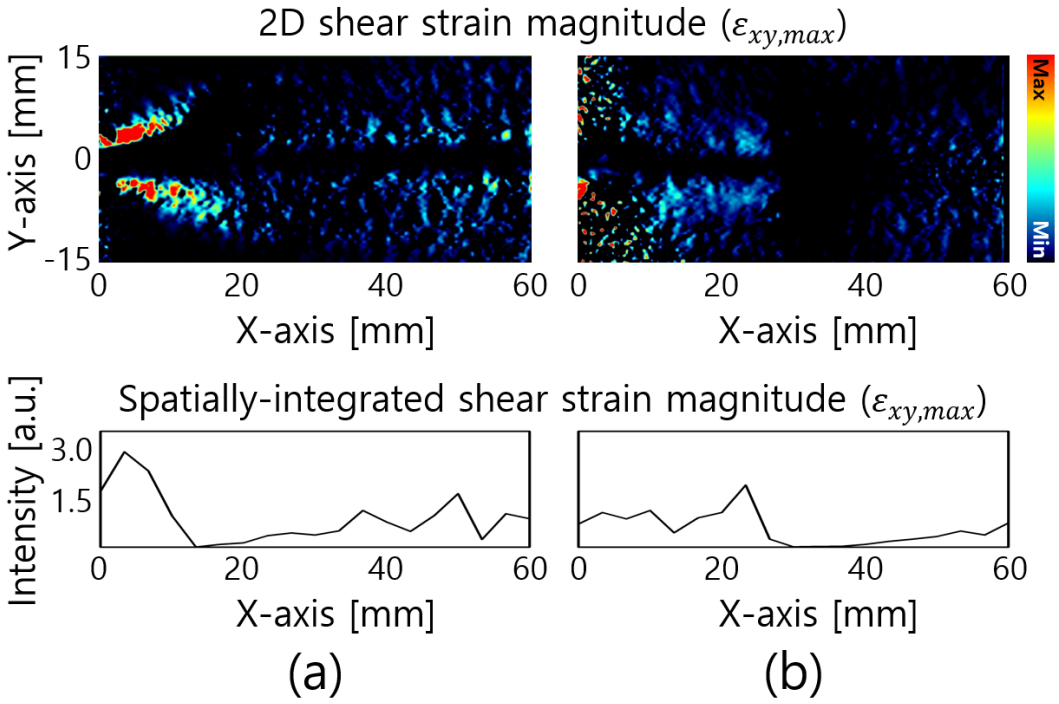

Fig. 3.9 Shear strain magnitude ($\varepsilon_{xy,max}$), obtained by PIV, for (a) attached and (b) detached reference flames with O/F ratio = 2.85, $\dot{V}_{O_2}$ = 50 slpm, and $\dot{V}_{CH_4}$ = 35 slpm. Top row: time-averaged 2D $\varepsilon_{xy,max}$. Bottom row: spatially-integrated $\varepsilon_{xy,max}$ spectrum along the Y-axis.

The detached flame fluctuated despite the absence of any external excitation. Figure 3.10(a) shows the $p'/\bar{p}$, which represents the strength of the pressure perturbations (p') relative to the average pressure ($\bar{p}$) inside the combustor during the D-A transition. Furthermore, $p'/\bar{p}$ was moderate for the detached flame (Fig. 3.10(a)(i)); increased in the fluctuating region (Fig. 3.10(a)(ii)), then, decreased gradually during the transition process (Fig. 3.10(a)(iii)) before reaching a minimum for the attached flame (Fig. 3.10(a)(iv)). The $p'/\bar{p}$ frequency in the fluctuating region in Fig. 3.10(a)(ii) was measured as about 670 Hz by conducting a 1-D CWT analysis, as shown in Fig. 3.10(b).

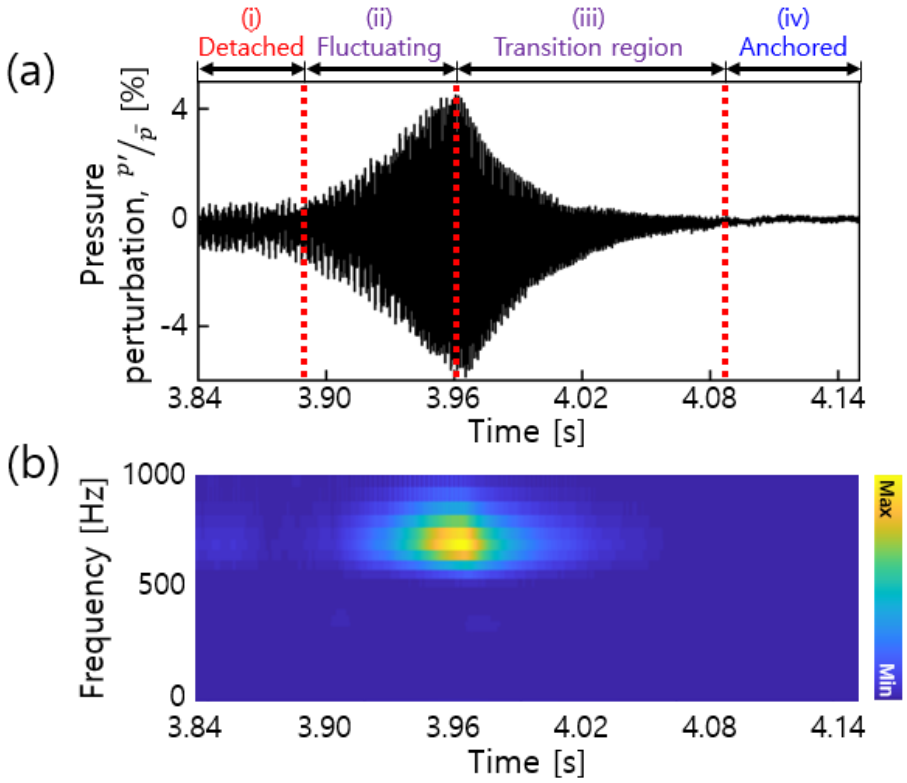

Fig. 3.10 (a) Variation in strength of pressure perturbation ($p'/\bar{p}$) for (i) detached flame, (ii) a fluctuating flame, (iii) the transition region, and (iv) an attached flame. (b) Perturbation frequency for the same time range covered in Fig. 3.10(a) for a transition from a detached to attached flame. The O/F ratio was continuously increased from 6.23 to 7.12.

Since the combustor used in this study has a closed-open boundary condition with an open end, the resonant frequency can be calculated through Eq. (3.1).

$$f = \frac{(2n-1)\cdot c}{4L}, \tag{3.1}$$

where L is the combustor length, c is the sound speed, and n is a positive integer.

The modified temperature inside the combustor was measured to be about 800 K, and the length of the combustion chamber is 225 mm, so the fundamental resonant frequency was calculated as 651.1 Hz. Therefore, it is confirmed that the frequency of perturbation corresponds to the resonant frequency of the combustion chamber.

To investigate the fluctuation, the Strouhal number (*St*) is measured, which describes oscillating flow mechanisms and is defined as in [122]:

$$St = \frac{f_v \cdot D}{\Delta \mathrm{V}}, \tag{3.2}$$

where f_v is the vortex shedding frequency and D is the oxygen post diameter.

The vortex in the shear layer is the most unstable where the *St* was between 0.1 and 0.3 [8, 122], which is called the preferred mode [123]. In this case, the *St* was calculated as approximately 0.18 at f_v = 670 Hz, indicating that fluctuations in the transition region can be attributed to vortex shedding in the shear layer.

To determine the cause of the change in the perturbation strength, the effect of the vortex shedding on the perturbation strength is investigated by calculating the *St*, and then the vortex shedding is measured through PIV. First, the D-A transition was observed under various constant $\dot{V}_{O_2}$ conditions including 50 slpm as $\dot{V}_{CH_4}$ decreased. Figure 3.11 shows *St* numbers under each $\dot{V}_{O_2}$ condition when the D-A transition occurred (St_{tran}) and when the maximum pressure perturbation occurred before the transition (St_{max}), respectively. When $\dot{V}_{O_2}$ was small, the strongest pressure perturbation occurred just before the D-A transition. However, when $\dot{V}_{O_2}$ became large, the D-A transition occurred at larger ΔV

than that at which the maximum pressure perturbation occurred. Therefore, the pressure perturbation strength at the D-A transition was smaller than the maximum strength.

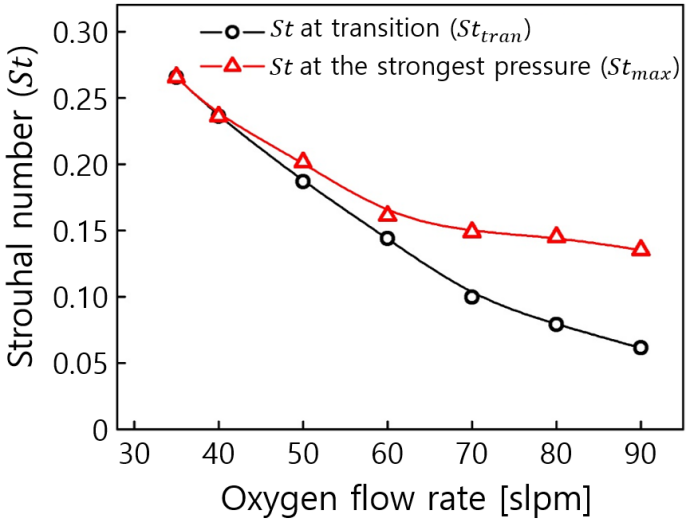

Fig. 3.11 *St* numbers under each $\dot{V}_{O_2}$ condition when the D-A transition occurred (St_{tran}) and when the maximum pressure perturbation occurred before the transition (St_{max}), respectively.

Two conditions are required for D-A transition to occur. The first is that the flame must be formed near the injector exit, and the second is that there must be a perturbation of the flame. However, if either condition becomes extreme, the influence of the other condition becomes less. In other words, if the ΔV becomes very large, the flame may attach to the injector even if the perturbation is small, so that a D-A transition may occur. In contrast, even if the flame is away from the injector, the D-A transition can occur owing to the strong perturbation. When the ΔV satisfies the preferred mode, resonance occurs between the vortex shedding in the shear layer and the combustor, resulting in a rapid increase in pressure perturbation in the combustor. Furthermore, when the overall flow rate is small, the flame is easily pulled towards the injector.

When the $\dot{V}_{O_2}$ was less than 40 slpm, a larger ΔV was required to satisfy the preferred mode condition than the D-A transition. However, under the condition just before the D-A transition, the flame was sufficiently pulled near the injector and the pressure perturbation was strong enough for the flame to attach to the injector. Therefore, the pressure perturbation was maximum at the D-A transition condition, so St_{tran} and St_{max} are the same. However, when the $\dot{V}_{O_2}$ was between 40-50 slpm, the flame was pushed downstream owing to the increase in the overall flow rate, so a larger ΔV was required for the flame to form near the injector, and the D-A transition condition and the preferred mode condition coincided. When the $\dot{V}_{O_2}$ was greater than 50 slpm, even though the preferred mode condition occurred, the D-A transition did not occur because the flame was pushed downstream due to the increase in the overall flow velocity. Although a further increase in ΔV reduced pressure perturbation strength, it pulled the flame further toward the injector, resulting in the D-A transition. Therefore, St_{max} was kept between 0.1 and 0.3, but St_{tran} decreased gradually since a larger ΔV was required for D-A transition as increasing the $\dot{V}_{O_2}$. In consequence, ΔV is a key parameter to determine the pressure perturbation.

Figure 3.12 shows streamlines for the bottom half of a detached flame, before the transition, obtained via PIV measurements. For the time-averaged streamline (Fig. 3.12(a)), the flow rotation was measured. Figures 3.12(b) and 3.12(c) show the instantaneous and phase-averaged streamline images, respectively. Clearly, a vortex formed near the flame base and propagated downstream. After the vortex moved downstream for 7 frames, a new vortex formed near the flame base and repeated the propagation process. Because these PIV measurements are conducted at 5 kHz, a 7-frame cycle corresponds to 714 Hz; thus, the detached flame, before transition, exhibits vortex perturbation at a frequency that is similar to that of p'. Therefore, just before the D-A transition with $\dot{V}_{O_2}$ = 50 slpm, the strength of the pressure perturbation was amplified because the preferred mode of vortex shedding in the shear layer between the two flows coincided with the resonant frequency of the combustor.

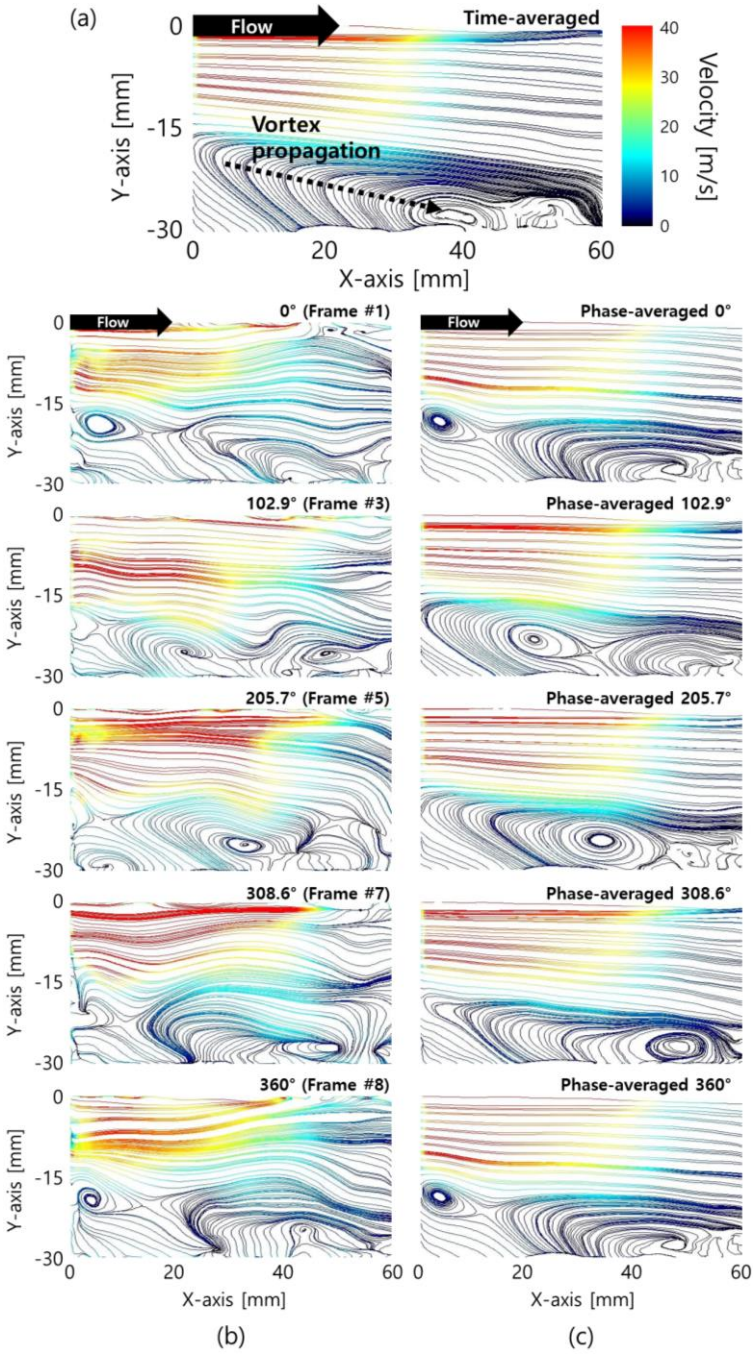

Fig. 3.12 (a) Time-averaged, (b) instantaneous, and (c) phase-averaged streamlines for the bottom half of the detached flame, with an O/F ratio = 6.23.

The images in Figs. 3.13 and 3.14 are obtained simultaneously with the $p'/\bar{p}$ measurements in Fig. 3.10(a). Figure 3.13 shows one cycle of the pressure and measured flame shape, obtained by OH^* chemiluminescence and OH-PLIF, for the fluctuating region represented in Fig. 3.10(a)(ii). Although OH^* chemiluminescence and OH-PLIF cannot be measured simultaneously due to the limitation of possessed equipment, two images of the same phase show a more detailed change in flame shape. The flame movement is analyzed by a previously reported method [124], based on pressure variations measured upstream and downstream of the combustor. The flame was pulled towards the injector because the pressure inside the combustor was greater than that at the inlet for the 0°–180° phase (Figs. 3.13(a) and 3.13(b)). However, as shown in Figs. 3.13(a) and 3.13(c), the pressure at the inlet was greater than that inside the combustor for the 180°–360° phase; thus, the flame propagated downstream. Consequently, in the fluctuating region, the flame continuously moved back and forth because of the pressure changes at the inlet and inside of the combustor. Furthermore, the strength of $p'/\bar{p}$ increased until the transition was reached.

Figure 3.14 demonstrates how the flame shape changes at the beginning of the transition region (Fig. 3.10(a)(iii)) as the O/F ratio increases continuously from 6.23 to 7.12. As shown in Figs. 3.14(a)–(c), the flame was pulled towards the injector, as in Fig. 3.13(b). In this case, however, the flame contacted the injector because of the strong $p'/\bar{p}$ (Fig. 3.14(c)), and could ignite the oxygen and methane inside the injector to form an attached flame, as shown in Figs. 3.14(d)–(f). After this attached flame formation, $p'/\bar{p}$ decreased; thus, the attached flame retained its state and additional flame shape transitions did not occur with further O/F ratio and ΔV increased.

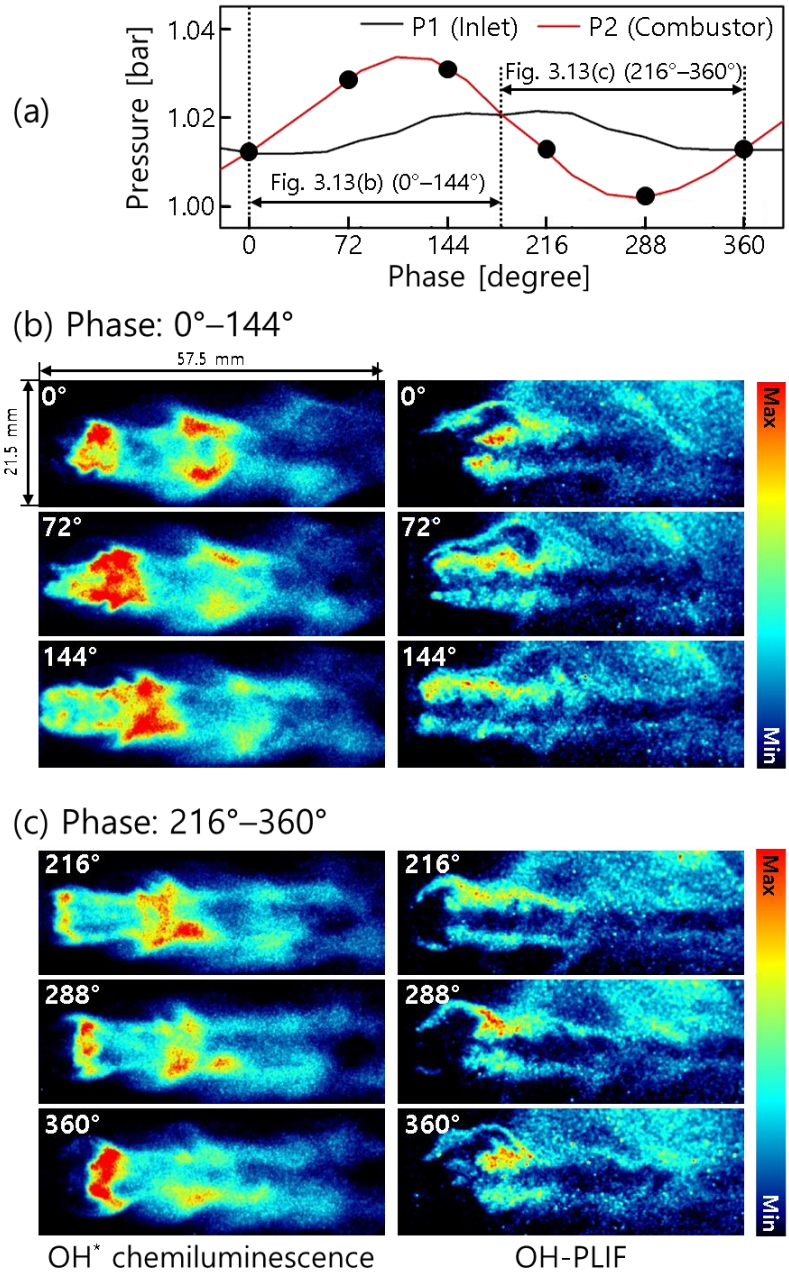

Fig. 3.13 (a) A single pressure variation cycle at the inlet and inside of the combustor, and (b-c) OH^* chemiluminescence and OH-PLIF images of the detached flame in the fluctuating region (Fig. 3.10(a)(ii)) for (b) 0°–144° and (c) 216°–360°.

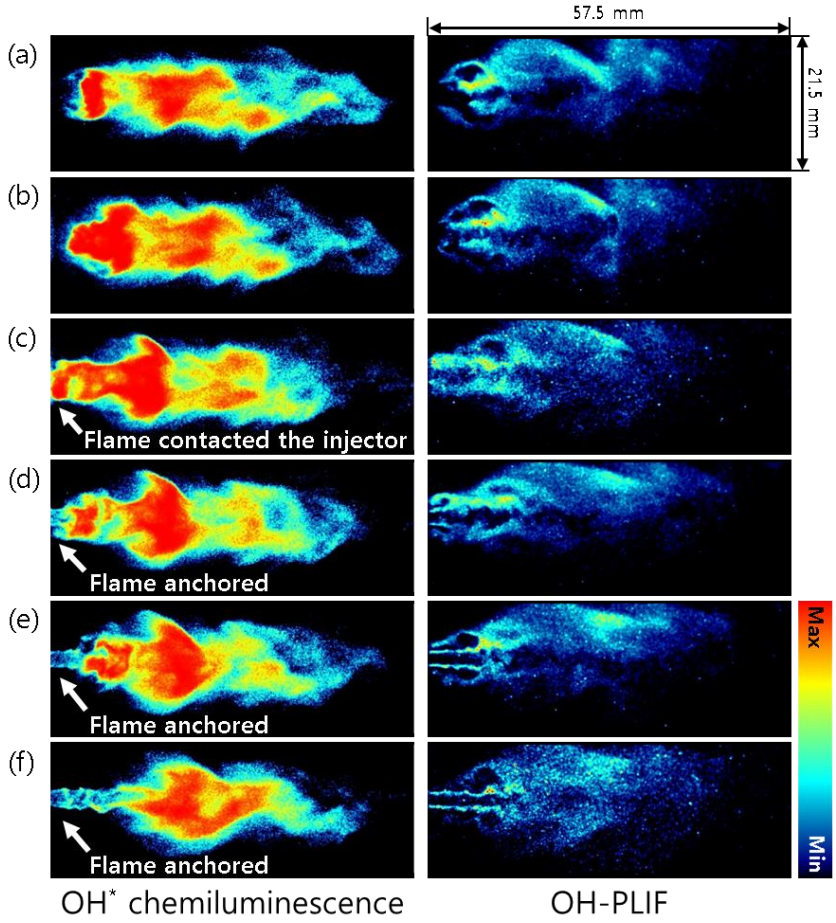

Fig. 3.14 Flame shape changes, measured by OH^* chemiluminescence and OH-PLIF, at the beginning of the transition region (Fig. 3.10(a)(iii)).

3.5 Bifurcation due to Acoustic Modulation

Flame shape deviations from the reference bistable flames in Fig. 3.2 are also investigated by varying the modulation strength under central oxygen flow, defined as the strength of oxygen velocity perturbations ($u'_{ox}/\bar{u}_{ox}$), calculated by dividing the velocity fluctuation (u'_{ox}) by the average velocity ($\bar{u}_{ox}$) in the oxygen feed line, which are measured by a HWA (Dantec, MiniCTA). A speaker is employed, and its voltage varies to control $u'_{ox}/\bar{u}_{ox}$ between 0 and near 100%. To exclude the resonance effect between the vortex and the combustion chamber and to consider only the perturbation effect of the flow, the modulation frequency is selected as not corresponding to the resonant frequency and preferred mode. Also, the speaker produces the strongest modulation at the 200 Hz for the same voltage. Furthermore, the flame has the characteristics of a low pass filter [49], so the flame does not have enough time to react to the external high-frequency perturbation resulting in the small perturbation. Therefore, a low frequency of 200 Hz is selected.

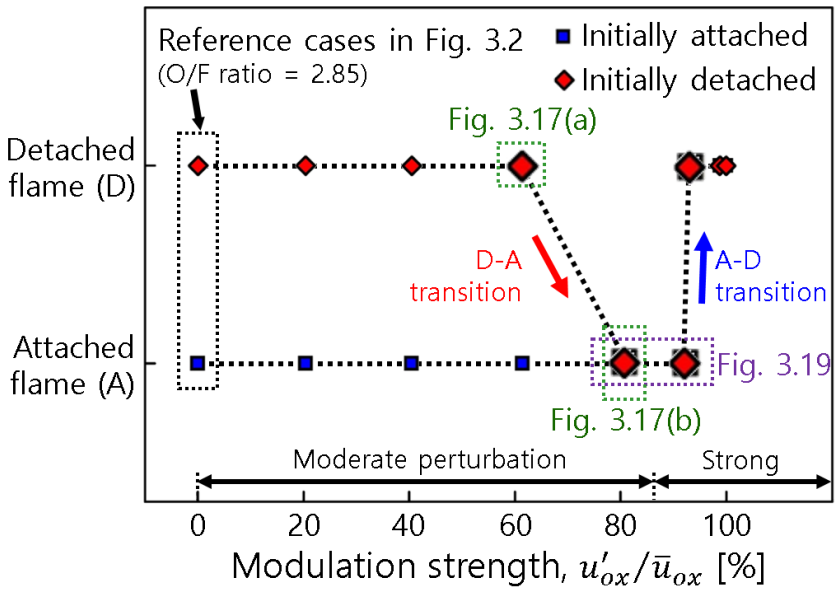

Fig. 3.15 Variation of flame shape for varied acoustic modulation strength. f_{ext} = 200 Hz, O/F ratio = 2.85.

As shown in Fig. 3.15, when $u'_{ox}/\bar{u}_{ox}$ = 80%, a pulsed detached flame attached to the injector rim and became a pulsed attached flame. However, for above $u'_{ox}/\bar{u}_{ox}$ = 93%, a pulsed attached flame detached from the injector rim and became a pulsed detached flame.

Figure 3.16 shows the bifurcation diagram through the pressure perturbation strength inside the combustor. As for the attached flame, the strength of pressure perturbation inside the combustor was proportional to the acoustic modulation strength. However, under more than 93% of acoustic modulation, the attached flame was transferred to the detached flame, and the pressure perturbation increased rapidly, resulting in the subcritical Hopf bifurcation.

As for the detached flame, since it was maintained up to about $u'_{ox}/\bar{u}_{ox}$ = 60%, the pressure perturbation inside the combustor increased in proportion to the acoustic modulation strength. However, when 80% of acoustic modulation was applied, the pressure perturbation inside the combustor rapidly decreased owing to the transition to the attached flame, so subcritical Hopf bifurcation occurred. When more than 93% of acoustic modulation was applied after the D-A transition, the pressure perturbation was discontinuously increased owing to the transition from attached to detached flame (A-D transition), resulting in subcritical Hopf bifurcation.

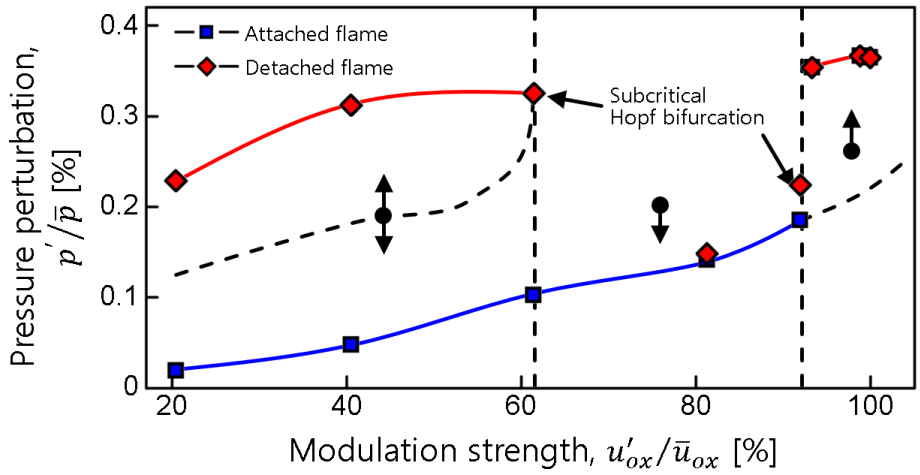

Fig. 3.16 Bifurcation diagram for varied acoustic modulation strength. f_{ext} = 200 Hz, O/F ratio = 2.85.

Figures 3.17(a) and 3.17(b) show the cycles of shape changes for a pulsed detached flame with $u'_{ox}/\bar{u}_{ox}$ = 60% and a pulsed attached flame with $u'_{ox}/\bar{u}_{ox}$ = 80%, respectively. As shown in Fig. 3.17(a), pulsed detached flames repeatedly formed at the constant auto-ignition location inside the combustor and propagated by burning off external unburned gas in cycles that correspond to the external acoustic modulation. Contrarily, pulsed attached flames were extended and then broken by the modulation. A small portion of the flame, however, remained anchored to the injector rim, denoted by the white circle in the first image of Fig. 3.17(b); thus, the next flame also formed as attached.

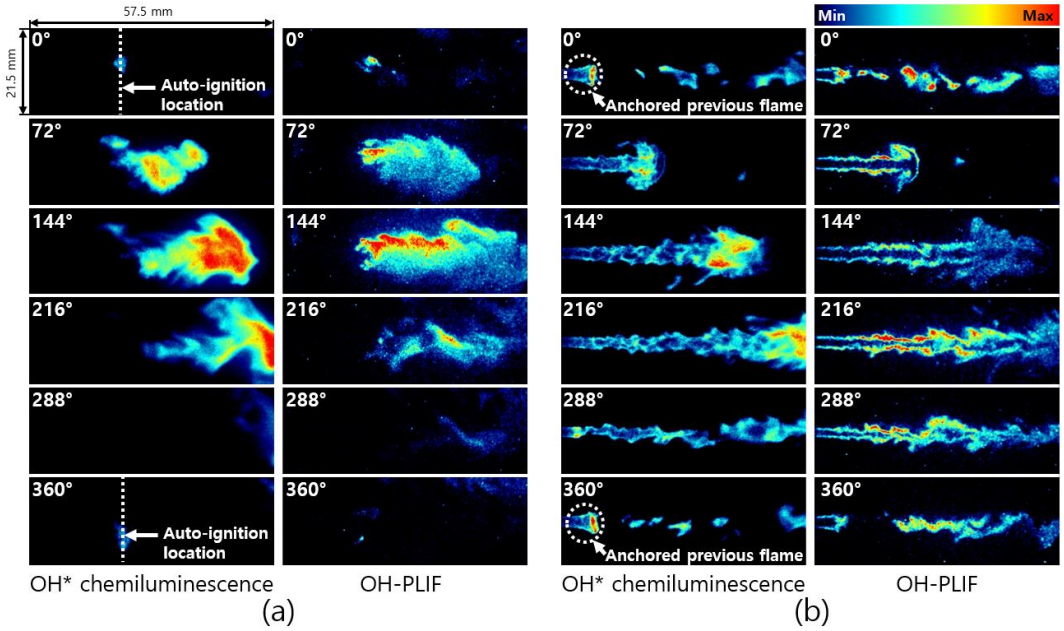

Fig. 3.17. One cycle of flame shape variation for a pulsed (a) detached flame with $u'_{ox}/\bar{u}_{ox}$ = 60% and (b) attached flame with $u'_{ox}/\bar{u}_{ox}$ = 80%. f_{ext} = 200 Hz, O/F ratio = 2.85.

The auto-ignition location of the pulsed detached flame shown in Fig. 3.17(a) is shown in Fig. 3.18 for varied $u'_{ox}/\bar{u}_{ox}$. Under moderate $u'_{ox}/\bar{u}_{ox}$, the auto-ignition location moved upstream with increasing $u'_{ox}/\bar{u}_{ox}$. The flammable region may be pulled towards the injector by increased mixing between oxygen and methane flows [125] and by the

suction force caused by acoustic perturbations. However, strong $u'_{ox}/\bar{u}_{ox}$ can interrupt the chemical reaction [117], causing local extinction at the injector rim and near the injector exit despite the strong suction force. Therefore, under strong perturbations, auto-ignition was pushed downstream with increasing $u'_{ox}/\bar{u}_{ox}$, contrary to the trend exhibited under moderate perturbations.

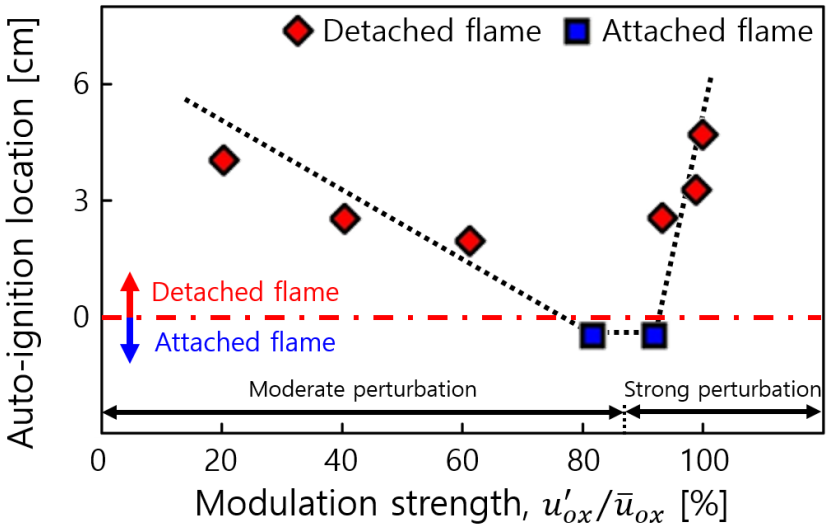

Fig. 3.18 Auto-ignition location for varied $u'_{ox}/\bar{u}_{ox}$. f_{ext} = 200 Hz, O/F ratio = 2.85.

Figure 3.19 shows the amount of the previous flame remaining anchored to the injector rim, before the next flame was formed, for varied $u'_{ox}/\bar{u}_{ox}$ for the attached flame. As $u'_{ox}/\bar{u}_{ox}$ increased, a smaller amount of the previous flame remained anchored to the injector rim before the new flames formed, because the flame was pulled more toward the injector due to stronger suction forces and mixing.

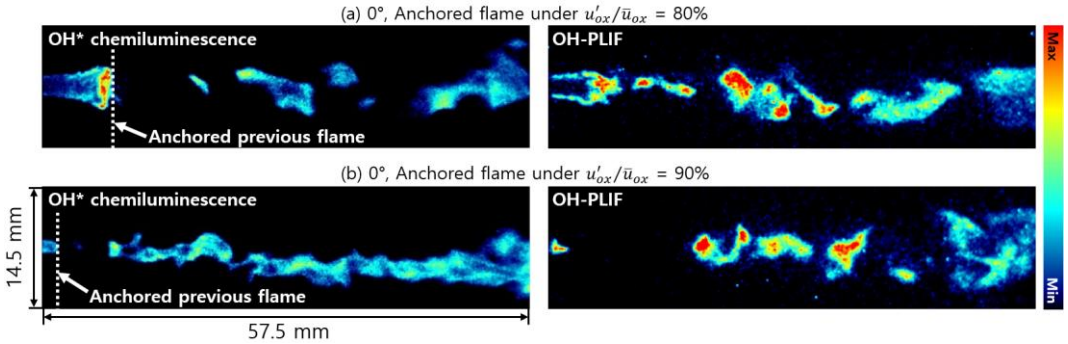

Fig. 3.19 Amount of previous pulsed attached flame remaining anchored to the injector rim for varied $u'_{ox}/\bar{u}_{ox}$: (a) 0°, $u'_{ox}/\bar{u}_{ox}$ = 80%; (b) 0°, $u'_{ox}/\bar{u}_{ox}$ = 90%. f_{ext} = 200 Hz, O/F ratio = 2.85.

Figure 3.20 shows ΔV for varied $u'_{ox}/\bar{u}_{ox}$. ΔV was calculated using the mass flow rate of oxygen and methane because it was difficult to measure the velocity change owing to the external acoustic modulation through PIV in real-time and the velocity of oxygen and methane measured by PIV in Chapter 3.4 was similar to the bulk velocity.

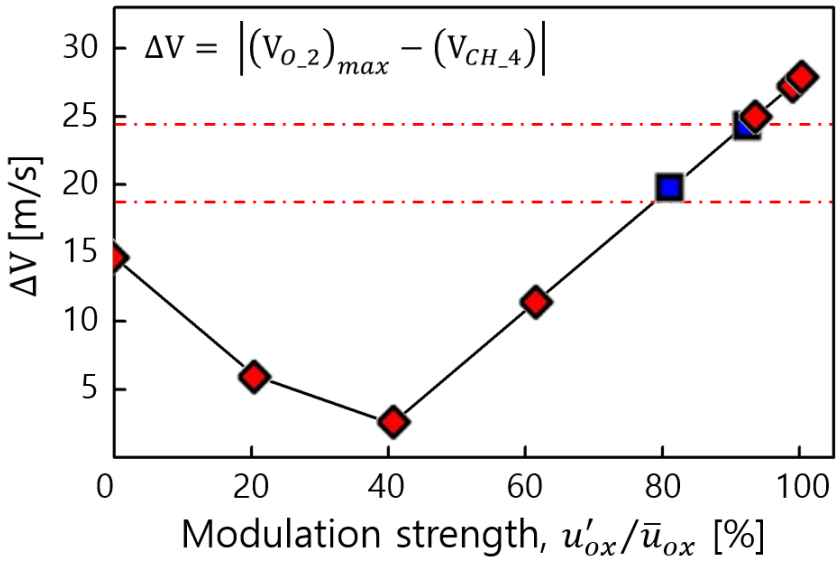

Fig. 3.20 Velocity difference (ΔV) for varied $u'_{ox}/\bar{u}_{ox}$. f_{ext} = 200 Hz, O/F ratio = 2.85.

For $\dot{V}_{O_2}$ values much smaller than $\dot{V}_{CH_4}$, flames are primarily formed in the outer, rather than inner (Fig. 3.8(b)), shear layer; thus, these flames are not attached [92], so the maximum oxygen velocities are used to calculate ΔV to determine the mixing strength in the inner shear layer. Thus, the D-A transition occurred when the ΔV > 20 m/s, as shown in Fig. 3.20, which agrees with the results for O/F ratio variation (Fig. 3.8(a)). When $u'_{ox}/\bar{u}_{ox}$ exceeded 90%, the flame might not be able to form due to excessive or insufficient oxygen supply and the normal chemical reactions were hindered near the injector because of local extinction [126], possibly causing the A-D transition [117].

Figure 3.21 shows the OH^* chemiluminescence and OH-PLIF images for flame shape changes during the D-A transition (moderate perturbation, Fig. 3.21(a)) and A-D transition (strong perturbation, Fig. 3.21(b)).

As shown in Fig. 3.17(a), the detached flame could not reach the injector under weak modulation, but increasing $u'_{ox}/\bar{u}_{ox}$ (Fig. 3.18) allowed the flame to pull towards the injector. Therefore, when $u'_{ox}/\bar{u}_{ox}$ > 80% (Fig. 3.21(a)), the detached flame could reach the injector and burn off the oxygen and methane inside the recess at t = 0.8 ms, thereby undergoing the D-A transition and forming an attached flame. The flame base at t = 1.6 ms had the same width as that of the attached flame; thus, the transition was determined to occur at t = 1.6 ms, and the flame at t < 1.2 ms was considered to be in the previous transition stage. These results agree with the trend shown in a previous LES study [104], which was not identified in a previous experimental study [117]. Notably, the bistable characteristics of flames under constant conditions have not been satisfactorily examined for non-premixed flames; thus, results for premixed flames [104, 117] are used here for comparison. Contrarily, as shown in Fig. 3.19, as $u'_{ox}/\bar{u}_{ox}$ increased under pulsed attached flames, a smaller amount of a previous flame remained anchored to the injector rim before a new pulsed attached flame formed. Therefore, as shown in Fig. 3.21(b), when $u'_{ox}/\bar{u}_{ox}$ > 93%, a new flame formed (t = 1.2 ms) without any previous flame (t = 0.8 ms) because of the strong modulation. Consequently, this flame became detached at t = 1.6 ms. The flame was still near the injector at t = 1.2 ms; thus, the flame at t = 1.6 ms was

determined to have undergone the A-D transition. Furthermore, the detached flame propagated to the combustor downstream, it could burn off the external unburned gas, and the flame speed was the same as the flow velocity so that the flame could no longer be attached to the injector rim and remained in the detached state (A-D transition). This result agrees with the trend shown in a previous experimental study [117], which was not identified in a previous LES study [104] because the $u'_{ox}/\bar{u}_{ox}$ range was too narrow to observe this phenomenon.

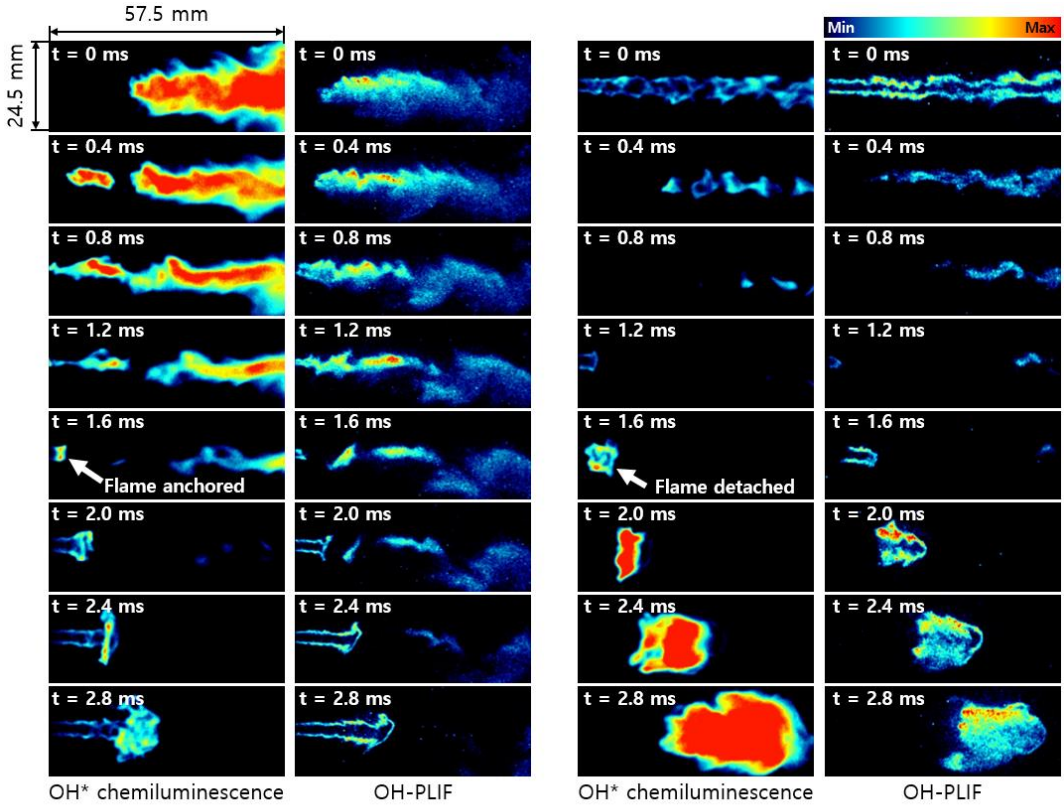

Fig. 3.21 Flame shape changes under transitions (a) from detached to attached (D-A transition, $u'_{ox}/\bar{u}_{ox}$ = 80%) and (b) from attached to detached (A-D transition, $u'_{ox}/\bar{u}_{ox}$ = 93%). f_{ext} = 200 Hz, O/F ratio = 2.85.

To understand the causes of the flame attaching and then detaching as the external acoustic modulation increased, the suction velocity is calculated through the difference between the flame speed and the flow velocity when the external flow is inhaled upstream. The flame speed is determined by measuring the flow velocity at the flame base via PIV without external modulation assuming that flame speed is the same as the flow velocity at the flame base because the detached flame in this study does not blow off or flashback. The theoretical suction distance is calculated through the product of the RMS value of the suction velocity and the half-period of the perturbation frequency. As shown in Fig. 3.22, the suction length increased linearly with the strength of external acoustic modulation. It can be seen that the flame was attached when the suction length was greater than the distance between the flame base without acoustic modulation and the oxygen post. Therefore, when the flame reached the oxygen post owing to the external acoustic modulation, the flame was anchored to the oxygen post by igniting oxygen and methane inside the recess, thereby forming the attached flame. In contrast, when the strength of the acoustic modulation exceeded 93%, a strong upstream pressure perturbation occurred and Δp increased, resulting in a flow separation where $\frac{dp}{dx} > 0$ at the oxygen post. Therefore, the A-D transition might occur as the flame anchoring was separated from the oxygen post.

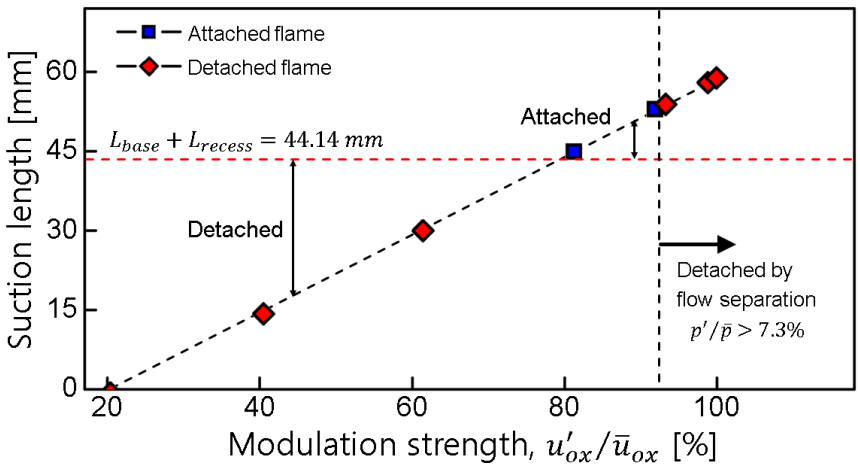

Fig. 3.22 Suction length for varied $u'_{ox}/\bar{u}_{ox}$. f_{ext} = 200 Hz, O/F ratio = 2.85.

In this study, characteristics of flame shapes are investigated experimentally for methane–oxygen flames formed by a recessed coaxial injector. In conclusion, flame shape is a key parameter to consider, in conjunction with the O/F ratio, in evaluating combustion characteristics. In particular, flame stability characteristics can be adjusted by controlling the flame shape through ΔV variation or external modulation application; varying ΔV can cause the transition from detached to attached flames, while the acoustic perturbations can cause the transitions in both directions. Thus, flames formed by recessed coaxial injectors can be stabilized by controlling the operating conditions or external disturbances, despite the constant geometric conditions.

CHAPTER 4

EFFECT OF DELAY TIME ON INSTABILITY CHARACTERISTICS

4.1 Background and Objectives

Research on combustion instability, which is the largest problem in the development of liquid rockets and dry low nitrogen oxide (NO_x) gas turbine engines, is being conducted since the discovery of combustion instability in the late 1930s [127]. The understanding of the combustion instability mechanism has been improved through many studies in which various analytic methods such as time-lag analysis have been used [9, 10]. Time-lag analysis [11] involves interpreting the combustion instability mechanism based on the delay time between the p' and q' inside the combustor. Figure 4.1 shows the waveforms for time-lag analysis performed using disturbances (p', mass flow, equivalence ratio (ϕ), and q').

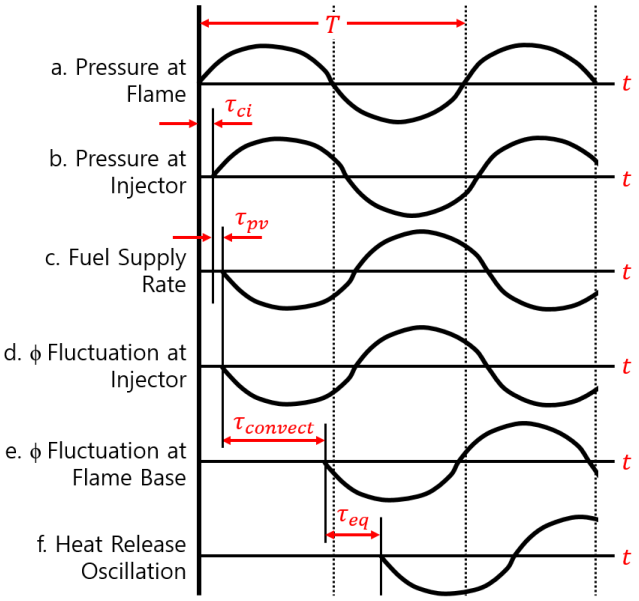

Fig. 4.1 Waveforms of disturbances for time-lag analysis [10].

Each disturbance lags behind the previous one, resulting in the delay time (delay time from pressure at flame to pressure at injector (τ_{ci}), delay time from pressure to mass flow modulation at injector (τ_{pv}), $\tau_{convect}$, and equivalent delay time (τ_{eq})). Time-lag analysis using the τ_{total}, which is the summation of all delay times, can be conducted by measuring the FTF [128] or by calculating the delay time using the measured flame structure and speed [9].

Lieuwen and Zinn [9] and Lieuwen [10] investigated combustion instability characteristics using the measured delay time and found that the range of the delay time in which instability occurred depended on the inlet conditions; if the fuel injector is unchoked, τ_{ci} and τ_{pv} can be neglected. Due to the perturbation in the flame, fluctuation occurs at the oxidizer and fuel, so the perturbation of the equivalence ratio can be expressed as Eq. (4.1).

$$\frac{\phi'}{\bar{\phi}} = \frac{\frac{m_f'}{\bar{m}_f} - \frac{m_o'}{\bar{m}_o}}{1 + \frac{m_o'}{\bar{m}_o}}, \tag{4.1}$$

where m_f and m_{o} are the flow rate of fuel and oxidizer, respectively.

Under the conditions where the fuel flow rate is less than the oxidizer flow rate, the change in the fuel flow rate has a dominant effect on the change in the equivalence ratio. Therefore, it can be assumed that there is no phase difference between the fuel flow rate and the equivalence ratio.

In addition, if the fuel injector is not choked, the fuel flow rate can be expressed as Eq. (4.2) using the pressure difference between the feed line and combustor.

$$m_f = K_{or}\sqrt{\Delta p_{or}}, \tag{4.2}$$

where K_{or} is an orifice coefficient and Δp_{or} is the pressure between the feed line and combustor.

Equation (4.3) is the result of differentiating Eq. (4.2) over time and shows that the

phases of the pressure difference and fuel flow are the same.

$$\frac{m_f'}{\bar{m}_f} = \frac{\Delta p_{or}'}{2\Delta p_{or}}, \tag{4.3}$$

Since the pressure difference is calculated by subtracting the pressure in the combustor from the feed line pressure, the pressure difference and the pressure in the combustor have a phase difference of 180 degrees. Therefore, the fuel flow rate and the pressure of the combustor have a phase difference of 180 degrees.

Figure 4.2 shows that the dependence of fuel flow rate through the fuel orifice to inlet duct pressure oscillations upon L_{fuel}/λ [9]. Unless the length of the fuel feed line corresponds to a multiple of the half-wavelength of the perturbations to cause destructive interference, the gain $\left(\left(m'_f/\bar{m}_f\right)/(p'/\bar{p})\right)$, which is the ratio between the two perturbations, has an almost constant value and the phase is near 180 degrees. In this study, since L_{fuel} is 47 mm, L_{fuel}/λ has a value near 0.2, so the phase difference between the pressure and fuel flow rate is 180 degrees, which represents that τ_{pv} is zero.

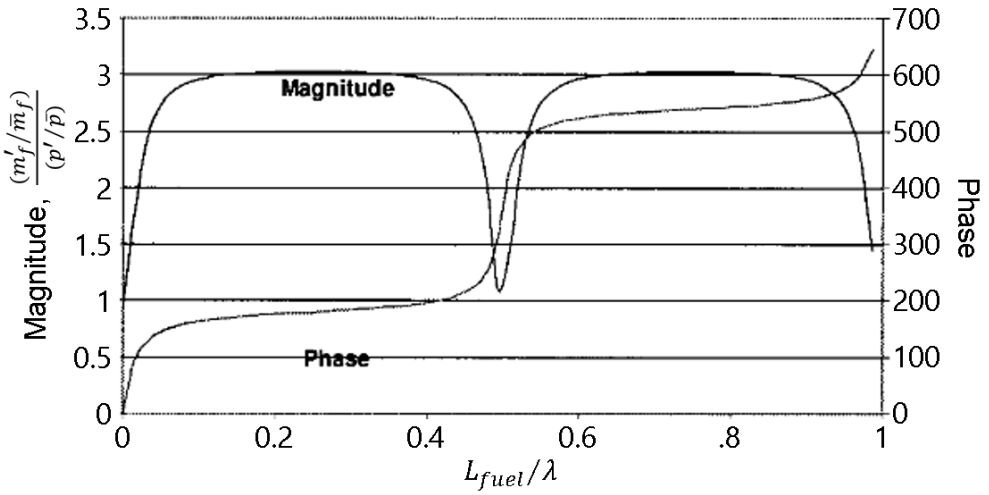

Fig. 4.2 Dependence of the response of the unsteady fuel flow rate through the fuel orifice to inlet duct pressure oscillations upon L_{fuel}/λ [9].

Furthermore, instability occurs when $\tau_{total} + 0.5T = nT$, where T is the acoustic period, which represents the condition where the phase difference between the p' and q' inside the combustor ($\theta_{p'-q'}$) is zero for constructive interference between them. These unstable conditions can be described as $\tau_{total}/T = n - 1/2$ $(n = 1, 2, \cdots)$, and they also coincide with the unstable conditions in Lee et al. [129], as shown in Fig. 4.3.

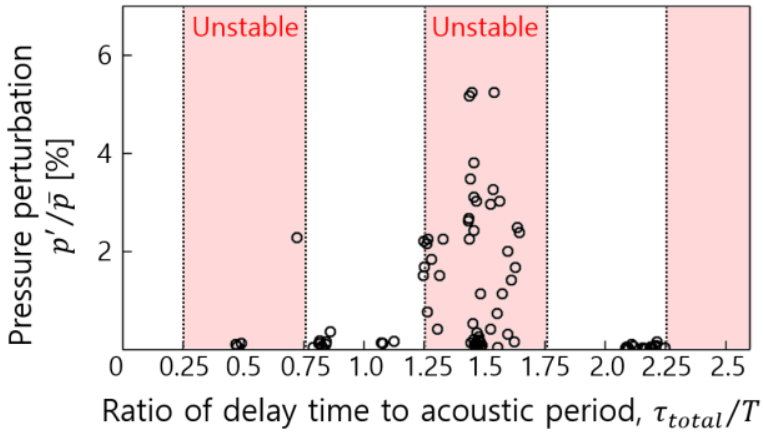

Fig. 4.3 Pressure perturbation ($p'/\bar{p}$) according to the total delay time (τ_{total}/T) [129].

Yoon et al. [31] found that the $\tau_{convect}$ of a partially premixed model combustor was the key parameter of the combustion instability mode shifting phenomenon. Furthermore, the development of high-repetition laser diagnostics such as PLIF and PIV has facilitated the precise measurement of flame structures and flow fields, thereby enabling deeper understanding of the combustion instability mechanism [130].

Although several studies on combustion instability have been carried out, the main subjects of those studies have been premixed flames [45, 49, 50]. Furthermore, because most propulsion systems use non-premixed flames formed by coaxial injectors, combustion instability characteristics of non-premixed flames should be identified to understand combustion instability in propulsion systems. Methane and oxygen are very popular propellants in the propulsion field because they have high specific thrust, are eco-friendly, and provide high performance. Therefore, research on combustion instability using

methane/oxygen and coaxial injectors has been continuously conducted in the recent past [92, 131, 132]. However, compared to premixed flames, not much research has been conducted on combustion instability [13] and the effects of delay time on combustion instability for non-premixed flames. In addition, to identify combustion instability in an engine under diverse operating conditions, combustion instability should be investigated under various experimental conditions. Therefore, the combustion instability characteristics and instability mode shift phenomenon of a non-premixed flame are investigated in the present study using a coaxial injector by conducting a time-lag analysis.

4.2 Experimental Methods

Figure 4.4 shows an atmospheric single-element combustor and a coaxial injector used in this study. The combustor has a square cross-section (80 × 80 mm^2), and four quartz windows are mounted on each side of the combustor for optical access. The downstream of the combustor is set as a closed boundary condition using a water-cooled movable plug nozzle, which is used to form an acoustic boundary at the combustor outlet by blocking 99.25% of the combustor area.

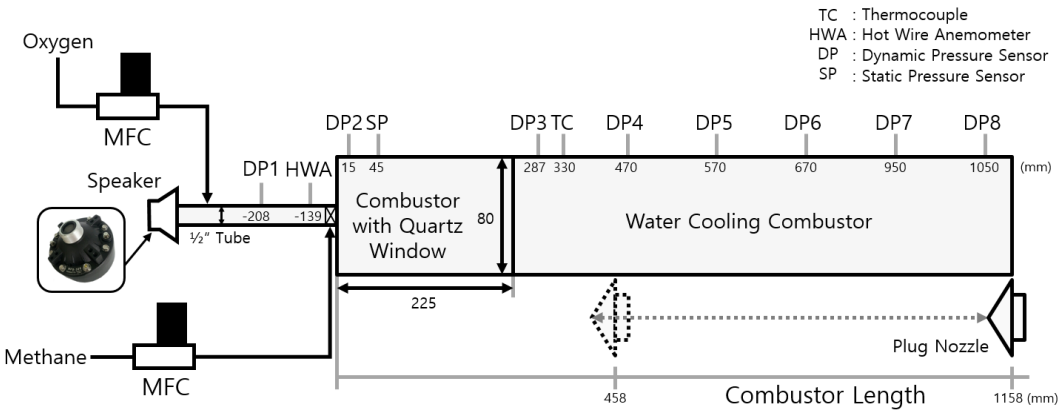

Fig. 4.4 Schematic of the single element combustor with acoustic modulation device.

Firstly, the effects of plug nozzle on acoustic boundary condition are explored by applying the external acoustic perturbation with a speaker. The modulation frequency is varied from 100 Hz to 450 Hz, and the modulation strength, which is defined as the strength of p'_{ox} relative to $\bar{p}_{ox}$, is kept constant at 5%. Before conducting the experiment for combustion instability, the experimental condition is determined using the stability map, which is identified with decreasing the methane flow rate (from 35 to 6 slpm) under each oxygen flow rate (70–160 slpm). Furthermore, for the combustion instability tests, the O/F ratios and combustor lengths are used as parameters. Under the O/F ratio variation tests, gaseous oxygen (O_2, 70–160 slpm, purity > 99.9 mol%) and gaseous methane (CH_4, 35 slpm, purity > 99.95 mol%) at 290 ± 5 K are supplied by MFC (LineTech, M3300V,

uncertainty = ±1% of full range) through a center jet and annular swirled jet, respectively. Furthermore, under the combustor length variation tests, the combustor length is varied from 458 mm to 1158 mm (span = 50 mm), which is the range of typical combustor characteristic lengths of rocket engines [133].

One static pressure sensor (SP) (VALCOM, VPRQ-A5-5bar, uncertainty = ±0.8%) and eight dynamic pressure sensors (DP) (PCB, 102A05 × 6, 102M205 × 2, uncertainty = ±1%) are used to measure the unsteady dynamic phenomenon at a rate of 10 kHz. The inlet oxygen velocity is measured by a HWA (Dantec, MiniCTA). The time interval between the two images of a PIV pair (dt) is 5 μs. The detailed test conditions of this chapter are summarized in the Table 4.1.

Table 4.1 Summary of the combustion instability test conditions.

Parameters	**Acoustic boundary**	**Stability map**	**O/F ratio**	**Combustor length**	**Unit**
Combustor exit condition	Closed end				-
Oxygen flow rate (Bulk velocity at injector exit)	-	70 ~ 160 (59.4 ~ 135.8)		110 (93.4)	slpm (m/s)
Methane flow rate (Bulk velocity at injector exit)	-	6 ~ 35 (9.8 ~ 57.1)	35 (57.1)		slpm (m/s)
O/F ratio	-	4.0 ~ 53.1	4.0 ~ 9.11	6.26	-
Inlet temperature		290			K
Oxygen Reynolds number	-	18,592 ~ 42,497		29,217	-
Methane Reynolds number	-	3,989 ~ 23,267	23,267		-
Modulation frequency	100 ~ 450	-			Hz
Modulation strength $(p'_{ox}/\bar{p}_{ox})$	5	-			%
Combustor length	1,158			458 ~ 1,158	mm

4.3 Acoustic Boundary Formation using Plug Nozzle

To achieve the resonance effect on the flame, the acoustic boundary condition inside the combustor is varied by moving the plug nozzle at the downstream of the combustor. To confirm whether the acoustic boundary condition exists inside the combustor, the acoustic transfer function (ATF) is calculated using Eq. (4.4) by applying external modulation.

$$\mathrm{ATF}(\omega) = \frac{p_{comb}{}'/\bar{p}_{\mathrm{comb}}}{p_{ox}{}'/\bar{p}_{\mathrm{ox}}}, \tag{4.4}$$

where p_{ox} and p_{comb} are the pressures at the inlet and inside of the combustor, respectively.

Therefore, the ATF represents pressure perturbation inside the combustor according to constant external modulation. Figure 4.5 shows the ATF according to the f_{ext} under a constant combustor length (L_{comb} = 1158 mm).

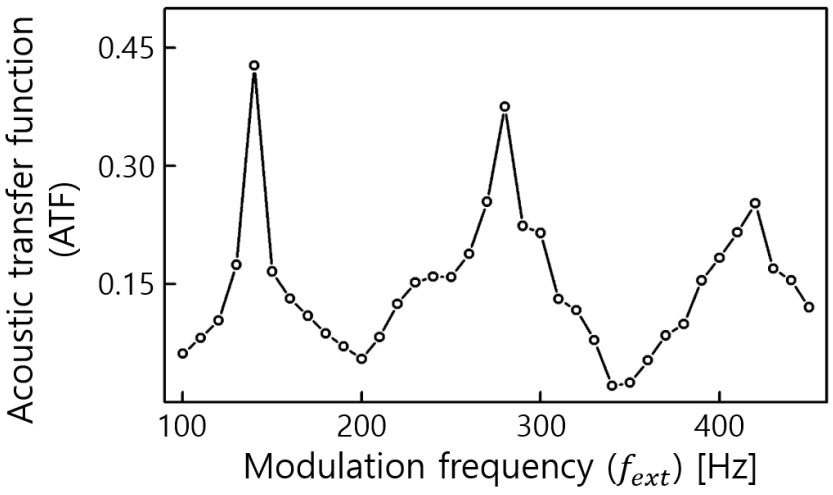

Fig. 4.5 Acoustic transfer function (ATF) according to the modulation frequencies (f_{ext} = 100–450 Hz, L_{comb} = 1158 mm).

The ATF shows peaks at modulation frequencies of 140, 280, and 420 Hz. The combustor in this study can be considered a closed-closed end pipe, and therefore, the resonant frequency can be calculated as

$$f_n = \frac{nc}{2L_{comb}}, \tag{4.5}$$

where f_n is the nth harmonic longitudinal resonant frequency, and c is the speed of sound.

In this study, the combustor length is 1158 mm, and the temperature inside the combustor is 290 K. Therefore, the fundamental longitudinal resonant frequency (f_1) is approximately 140 Hz. In other words, when external perturbations corresponding to the harmonic resonant frequency of the combustor are applied, resonance occurs inside the combustor, thereby resulting in a strong pressure perturbation. Therefore, we can confirm that a closed acoustic boundary is formed by the plug nozzle at the downstream of the combustor.

4.4 Stability Map

Figures 4.6(a) and 4.6(b) show the strength of pressure perturbation inside the combustor on varying the oxygen and methane flow rate under attached and detached flames, respectively. Although the pressure perturbation of the attached flame is not strong in the overall condition, strong pressure perturbation occurs in the detached flame despite the same flow conditions as the attached flame. According to Fig. 3.3 in the Chapter 3.3 and Fig. 4.6, the attached flame is considered stable with small perturbations of pressure and heat release rate, while the detached flame is considered unstable owing to the strong perturbations of pressure and heat release rate.

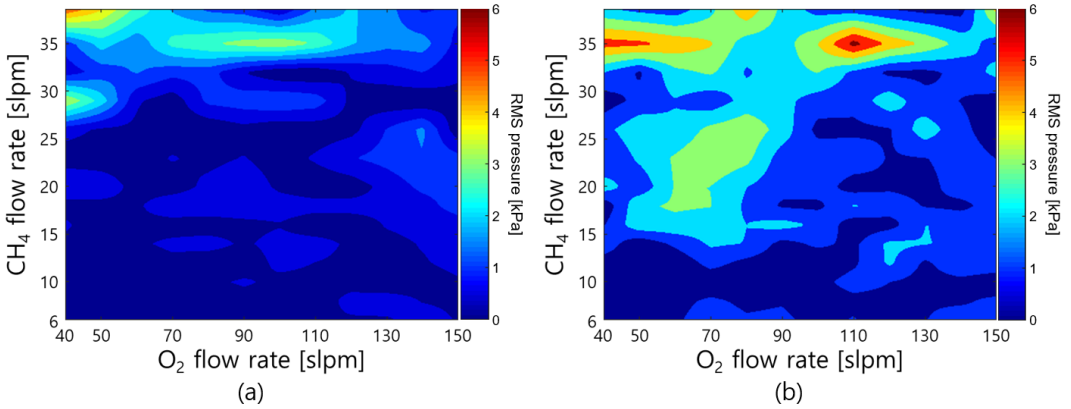

Fig. 4.6 Strength of pressure perturbation inside the combustor on varying the oxygen and methane flow rate under (a) attached and (b) detached flames, respectively.

Thus, this study aims to investigate the detached flames to identify the instability characteristics of unstable flame. According to the Chapter 3.4, the flame shape transition, under the open-end boundary condition, occurs from detached to attached flame with increasing the O/F ratio. However, the combustion instability is caused by the constructive interaction between the flame characteristics and combustor acoustics. Thus, in this study, the flame shape is determined, under the closed-end boundary condition by the plug nozzle, with decreasing the methane flow rate (from 35 to 6 slpm) under each oxygen flow rate

(70–160 slpm). Figure 4.7 shows the flame shape in terms of the oxygen velocity (V_{O_2}) and ΔV.

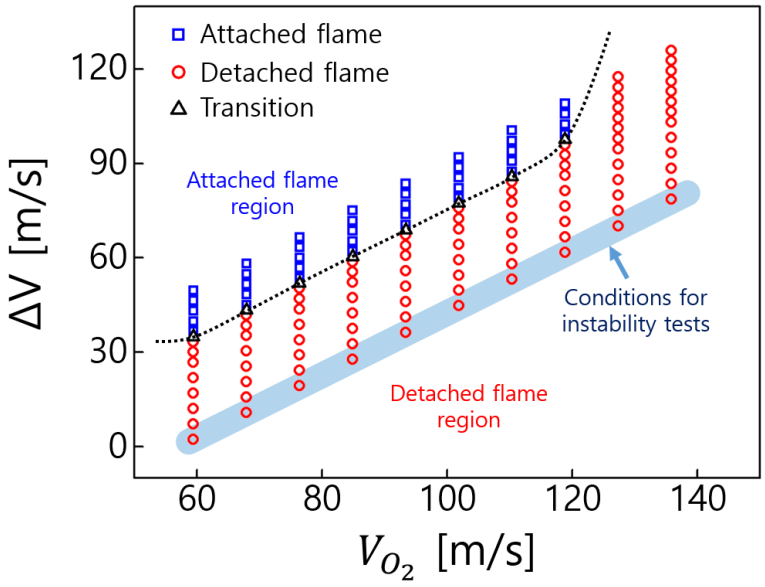

Fig. 4.7 Flame stability map in terms of oxygen velocity (V_{O_2}) and velocity difference (ΔV).

The flame shape transitions, owing to a decrease in methane flow rate, were observed in most oxygen flow conditions. As increasing the oxygen flow rate, the velocity difference at the transition increased, implying that more mixing strength was required for the flame to be anchored to the injector. If the fluid has compressibility effects, the gas density and temperature also become variables, resulting in the complicated characteristics and non-linearity effects. However, if Ma < 0.2, compressibility effects will be small and the fluid can be assumed as a simplified incompressible flow. The purpose of this study is to investigate the characteristics of unstable detached flame for varied various condition, thus, the methane flow rate is fixed at 35 slpm, as shown in Fig. 4.7, which represents a 20 kW combustor and makes Mach number under 0.185.

To avoid the compressibility effects but to obtain the acoustically closed boundary

effects, the condition ($0.1 < Ma < 0.2$) should be maintained at the nozzle. When the methane flow rate is constant at 35 slpm, Ma is calculated as 0.1 when the oxygen flow rate is 70 slpm, and Ma is calculated as 0.2 when the oxygen flow rate is 160 slpm. Furthermore, in this study, the strongest pressure perturbation occurs at an oxygen flow rate of 110 slpm and a methane flow rate of 35 slpm. Therefore, the oxygen flow rate is selected as 110 slpm for the experiments to determine the characteristics of combustion instability according to the change in combustor length.

4.5 Effect of O/F ratio on Combustion Instability Characteristics

To determine the combustion instability characteristics according to the O/F ratio that varies from 4.0 to 9.11, the combustor length and methane flow rate are held constant at 1158 mm and 35 slpm, respectively. Figure 4.8 shows the change in the instability frequency according to the O/F ratio. The instability frequency is determined as the frequency with the largest amplitude among the various frequency components of the pressure perturbation.

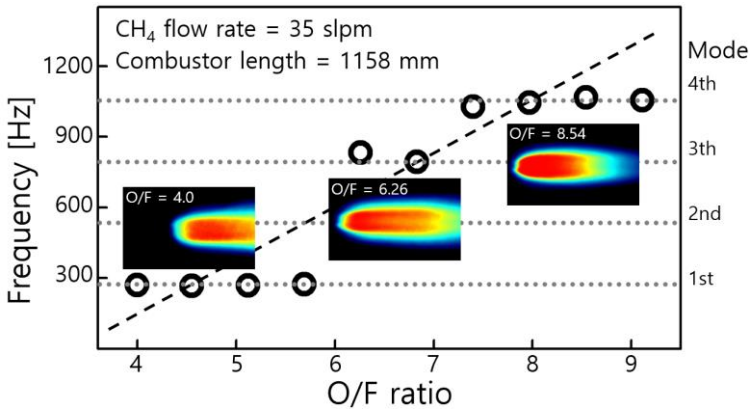

Fig. 4.8 Instability frequency according to the O/F ratio.

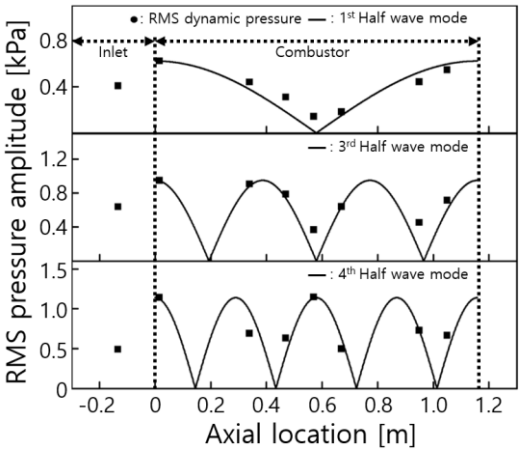

Fig. 4.9 Mode analysis based on the RMS pressure amplitude of each dynamic sensor.

Because the combustor length is held constant at 1158 mm, the fundamental longitudinal resonance frequency of the combustor is constant at approximately 290 Hz. As O/F ratio increased, the instability frequency changed from the first mode (≈290 Hz) to the fourth mode (≈1160 Hz) discretely; the modes were determined through mode analysis using the amplitudes of the pressure perturbations, as shown in Fig. 4.9.

4.5.1. Structural Flame Characteristics for Varied O/F Ratio

The OH^* chemiluminescence measurements are performed to investigate the flame characteristics and determine the integrated OH^* intensity to define the flame centroid. Figure 4.10 shows the flame shape that changed on varying the O/F ratio.

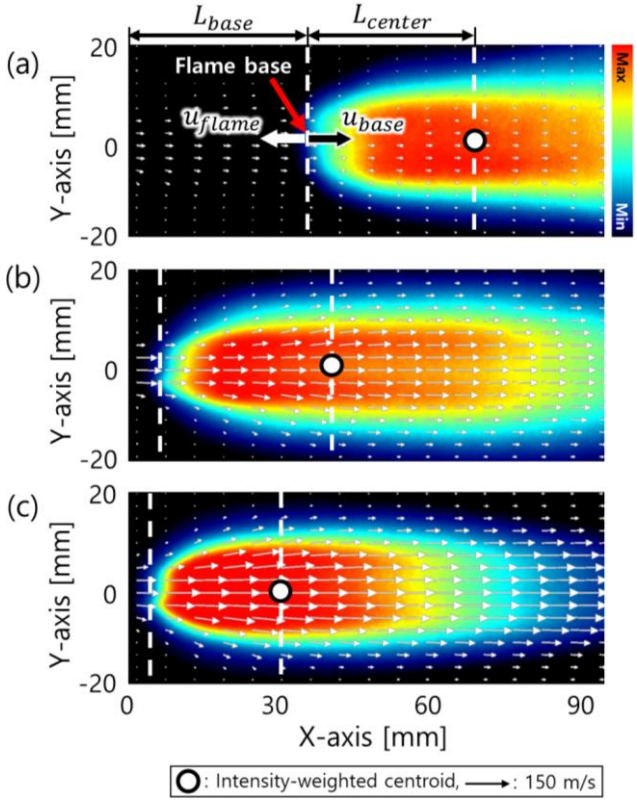

Fig. 4.10 Changing flame shapes, OH^* chemiluminescence intensity-weighted centroid, L_{base}, L_{center}, u_{base}, and u_{flame} for varied O/F ratios of (a) 4.0, (b) 6.26, and (c) 8.54.

L_{center} represents the distance from the flame base to the OH^* intensity centroid of the flame; L_{base} represents the distance from the injector exit to the flame base; and u_{base} represents the axial velocity at the flame base measured from the PIV image analysis. The chemiluminescence of the excited radicals in a flame is a consequence of chemical reactions [134]; therefore, a strong OH^* intensity indicates the strong magnitude of the reaction. Previous studies [31, 96, 135] have used the emission intensity from OH^* radicals to find the combustion region and flame centroid. Therefore, the flame base is determined as the first location where the gradient of the OH^* intensity, measured by OH-PLIF, is larger than the particular value, and the flame centroid is determined as the weighted average of the OH^* intensity. Furthermore, the flame speed (u_{flame}) is determined by measuring the u_{base} via PIV assuming that u_{flame} is the same as u_{base} because the detached flame in this study does not blow off or flashback.

Figure 4.11 presents the parameters of flame shape and velocities (L_{base}, L_{center}, u_{flame}, V_{O_2}, methane velocity (V_{CH_4}), and ΔV) according to the O/F ratio. As shown in Fig. 4.11(a), L_{base} is the maximum at an O/F ratio of 4.0 (stoichiometry condition), and it decreases as the O/F ratio deviated from 4.0. L_{center}, which is a characteristic length indicating the inverse of the degree of chemical reaction, also decreases as the O/F ratio increases. Furthermore, as shown in Fig. 4.11(b), u_{flame} increases as the O/F ratio increases.

To analyze the causes of changes in L_{base}, L_{center}, and u_{flame}, ΔV is calculated using V_{O_2} and V_{CH_4} according to the O/F ratio. In the coaxial injector used in this study, V_{O_2} and V_{CH_4} are the same at an O/F ratio of 4.0. Therefore, ΔV was almost zero at an O/F ratio of 4.0, and it increased as the O/F ratio deviated from 4.0, as shown in Fig. 4.11(c).

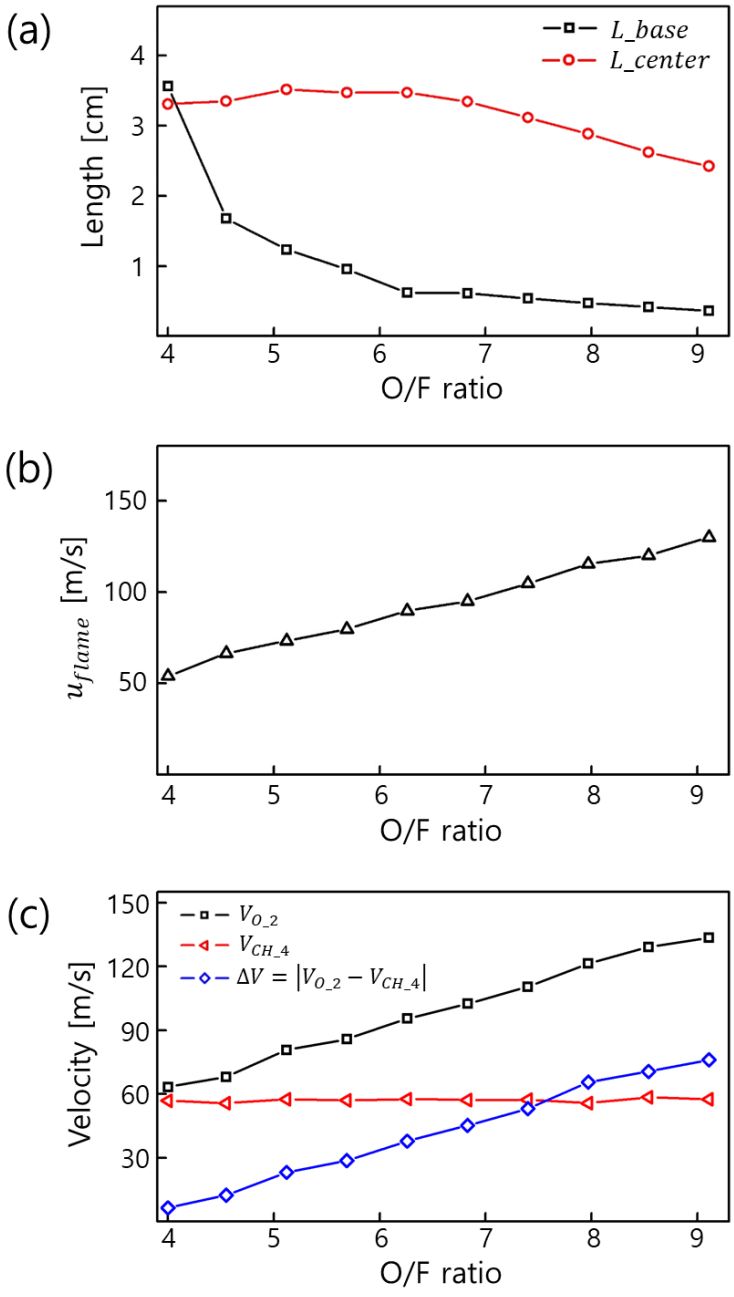

Fig. 4.11 Parameters of flame shape and velocities: (a) L_{base} and L_{center}, (b) u_{flame}, and (c) oxygen velocity (V_{O_2}), methane velocity (V_{CH_4}), and velocity difference between oxygen and methane (ΔV) according to O/F ratio.

To determine the mixing between oxygen and methane, the shear strain from immediately after the injector exit to near the flame base should be measured in the same region, indicated by the red-dashed box in Fig. 2.18 in Chapter 2.5. Figure 4.12 shows the shear strain magnitudes under different O/F ratios. The shear strain produces vortices that cause the mixing of the two flows. Areas with high shear strength are indicated in red in Fig. 4.12, and these areas represent regions where oxygen and methane are actively mixed.

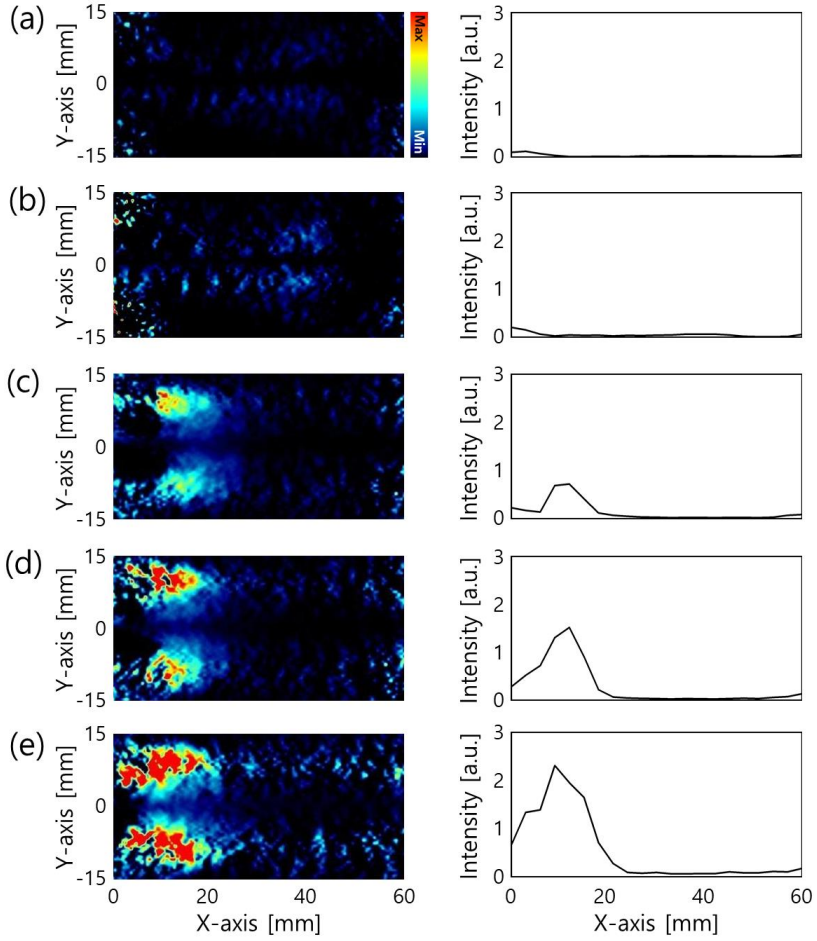

Fig. 4.12 Shear strain magnitudes ($\varepsilon_{xy,max}$) at different O/F ratios of (a) 4.0, (b) 5.12, (c) 6.26, (d) 7.4, and (e) 8.54. Left: time-averaged 2D $\varepsilon_{xy,max}$. Right: spatially-integrated $\varepsilon_{xy,max}$ spectrum along the Y-axis.

As observed in Fig. 4.12, the shear strength increased as the O/F ratio deviated from 4.0. As turbulent mixing increases between oxygen and methane owing to the increase in ΔV [118], the chemical reaction rate increases [121]. Furthermore, according to Oster [119], a larger ΔV causes the shear layer to spread faster into the low-speed region and results in a linear increase in the growth rate of the shear layer. Thus, for an O/F ratio of 4.0, the flame formed at the farthest location from the injector face because the mixing effect was the smallest, and therefore, L_{base} reached the maximum value. On increasing the O/F ratio, L_{base} decreased owing to increased mixing between oxygen and methane, as shown in Fig. 4.11(a). Furthermore, as the O/F ratio increased, the chemical reaction became stronger; therefore, u_{flame} increased and the flame became shorter, causing a decrease in L_{center} as shown in Figs. 4.11(a) and 4.11(b).

4.5.2. Time-lag Approach

To investigate the combustion instability characteristics via time-lag analysis, τ_{total} is calculated as

$$\tau_{total} = \tau_{pv} + \tau_{conv} + \tau_{eq} = \tau_{pv} + \frac{L_{inj}}{\bar{U}} + \frac{L_{center}}{u_{base}}, \quad (4.6)$$

where τ_{pv} is the delay time from the pressure perturbation to the flow modulation at the injector; τ_{pv}/T is generally 0 when the fuel injector is unchoked [10].

Figure 4.13 presents the parameters associated with τ_{total} described in Eq. (4.6). τ_{conv} is the convection delay time between the global equivalence ratio perturbation at the injector and at flame base; L_{inj} is the distance from the fuel-injection hole to the flame base (L_{recess} + L_{base}); $\bar{U}$ represents the mean velocity of unburned gas inside the injector; and τ_{eq} is the equivalent delay time, which is the delay time between the global equivalence ratio perturbation at the flame base and total heat release oscillation. Because the flame is axis-symmetric and oxygen is injected as a jet, 1-D time-lag analysis using the axial length and velocity is performed, as shown in Eq. (4.6). Therefore, the combustion

process is theoretically unstable when $\tau_{total} = (n - 0.5)T$, where T represents the oscillation period.

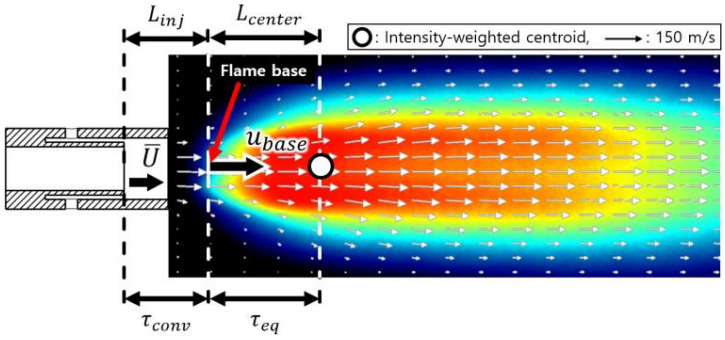

Fig. 4.13 Parameters for calculating τ_{total}.

Figure 4.14 shows the τ_{conv}, τ_{eq}, and τ_{total} calculated using L_{inj}, L_{center}, $\bar{U}$, and u_{base}. On increasing the O/F ratio, the velocities ($\bar{U}$ and u_{base}), which are the denominator terms in the equation for calculating τ_{total}, increase; however, the lengths (L_{inj} and L_{center}), which are the numerator terms, decrease, thereby yielding a decreased τ_{total}. As τ_{total} is determined according to the O/F ratio, the changes in the instability frequencies according to τ_{total} can be investigated.

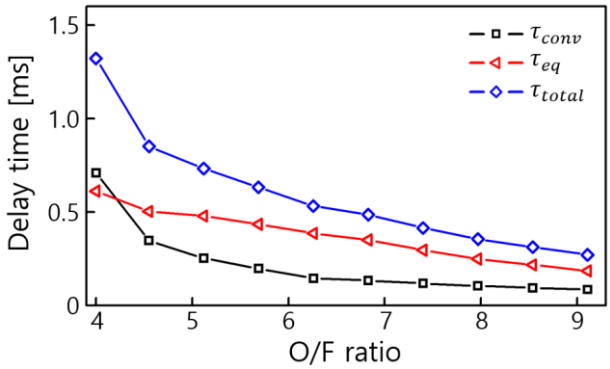

Fig. 4.14 Convective delay time (τ_{conv}), equivalent delay time (τ_{eq}), and total delay time (τ_{total}) in terms of O/F ratio.

Figure 4.15 shows the change in the instability frequency according to τ_{total}. On increasing τ_{total}, the instability mode shifted from the high mode to the low mode. This trend is the same as that obtained for a partially premixed flame by Yoon et al. [31].

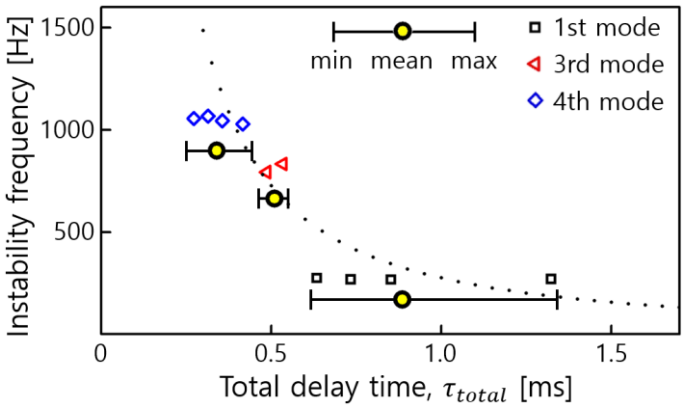

Fig. 4.15 Effect of τ_{total} on instability frequency (O/F ratio = 4.0–9.11, L_{comb} = 1158 mm).

The condition for combustion instability can be determined by the Rayleigh criterion using the Rayleigh's index (RI) as

$$\mathrm{RI} = \int_0^T p'(t) \cdot q'(t)\, dt. \tag{4.7}$$

RI indicates the degree of interaction between p' and q'. A positive RI implies that p' and q' are in phase because $-90° < \theta_{p'-q'} < 90°$. In contrast, a negative RI means that p' and q' are out of phase because $90° < |\theta_{p'-q'}| < 180°$.

Figure 4.16 presents the conditions that yield a positive RI for triggering combustion instability under each mode; τ_{total} is indicated by black arrows. As shown in Fig. 4.16(a), when τ_{total} is $\tau_{total,3}$, a positive RI is obtained in the third mode. Therefore, combustion instability occurs in the third mode frequency because p' and q' are in phase. When τ_{total} increases further, combustion instability occurs in the second or fundamental mode

because of the positive RI, as shown in Figs. 4.16(b) or 4.16(c), respectively. Therefore, on increasing τ_{total}, the instability mode shifts from the high mode to the low mode.

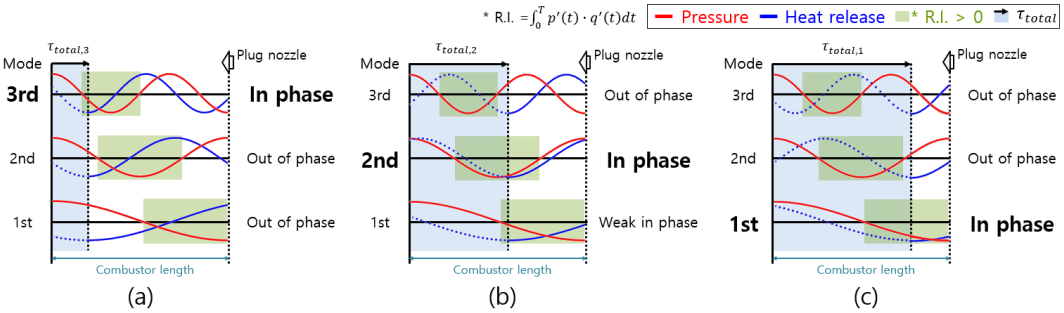

Fig. 4.16 Waveforms of the (a) third, (b) second, and (c) first mode occurrences based on time-lag analysis performed by varying τ_{total}.

4.6 Effect of Combustor Length on Combustion Instability Characteristics

Among all test conditions (O/F ratio = 4.0–9.11 and L_{comb} = 458–1158 mm), the pressure perturbation inside the combustor was the strongest ($p'/\bar{p}$ = 1.41%) at an O/F ratio of 6.26 and L_{comb} = 458 mm. Therefore, the effect of the combustor length on the instability characteristics is investigated for an O/F ratio of 6.26 by moving the plug nozzle. When the O/F ratio was 6.26, the average flame shape was consistent despite the change in the combustor length, and therefore, τ_{total} was consistent as shown in Fig. 4.17.

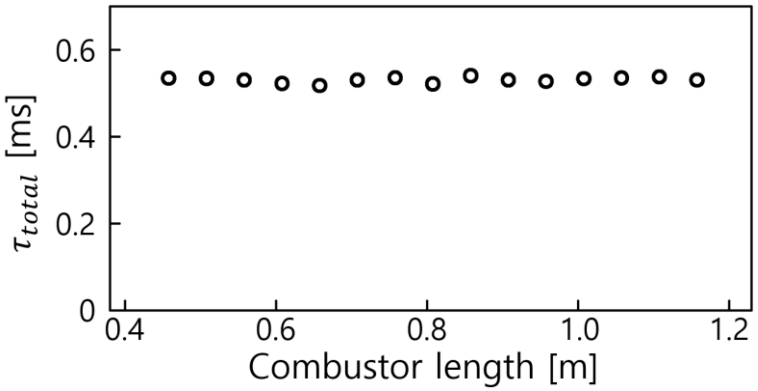

Fig. 4.17 Total delay time (τ_{total}) according to combustor length.

Figure 4.18 shows the instability frequency and strength obtained on varying the combustor length. As shown in Fig. 4.18(a), on increasing the combustor length, the instability frequency decreased because the longitudinal resonant frequency decreased. In other words, the instability frequency changed to match the resonant frequency of the combustor. However, when the instability frequency reached approximately 750 Hz, it did not decrease further but shifted to a higher mode. Therefore, the instability mode shifted from the fundamental longitudinal mode to the third harmonic mode as the combustor length increased from 458 mm to 1158 mm; this caused pressure perturbations only in a particular frequency range (750–1300 Hz). Furthermore, as shown in Fig. 4.18(b), the

amplitudes of pressure perturbation ($p'/\bar{p}$) increased at combustor lengths (458 and 858 mm) for which the harmonic resonant frequency is close to 900 Hz.

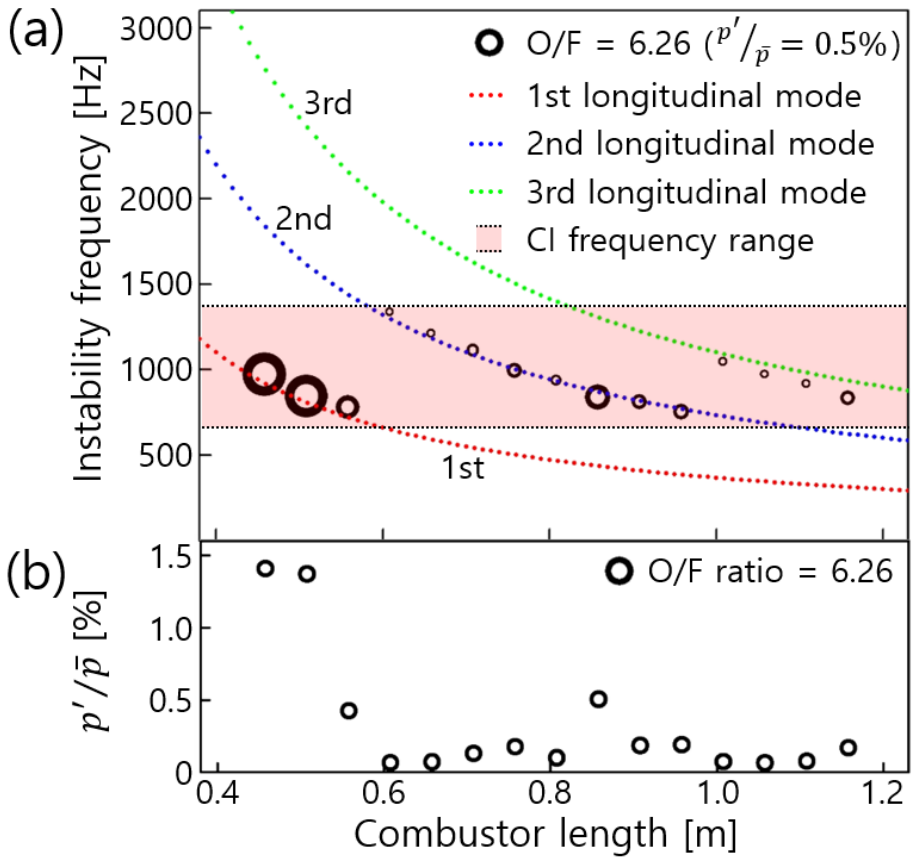

Fig. 4.18 Effect of combustor length on the instability: (a) frequency and (b) strength (O/F = 6.26).

Figure 4.19 shows the instability frequency on varying the combustor length (L_{comb} = 458–1158 mm) at each O/F ratio (O/F ratio = 4.0–9.11). As in Fig. 4.19, in each O/F ratio, instability occurred only within a particular frequency range according to the change in combustor length, and this range gradually increased toward higher frequency as the O/F ratio increased.

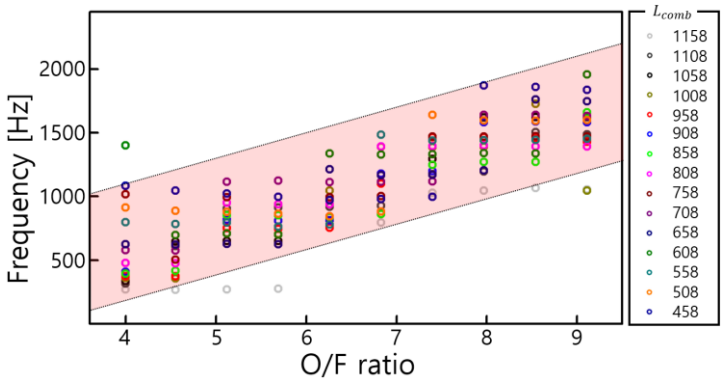

Fig. 4.19 Effect of O/F ratio on instability frequency with varying the combustor length (O/F ratio = 4.0–9.11, L_{comb} = 458–1158 mm).

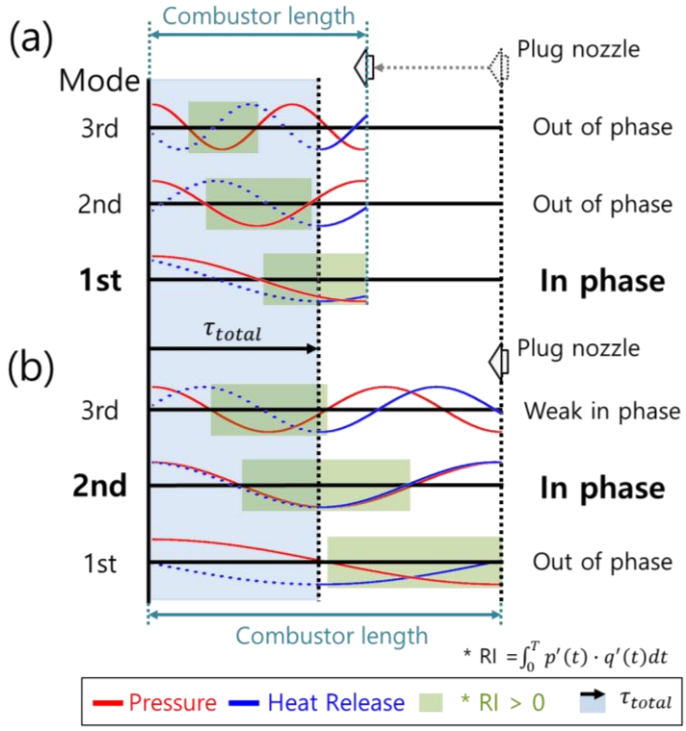

Fig. 4.20 Waveforms of (a) the first (L_{comb} = 458 mm) and (b) second mode (L_{comb} = 858 mm) occurrences based on time-lag analysis with varying combustor lengths (O/F = 6.26).

To analysis the transition of instability mode, Fig. 4.20 shows the conditions that yields a positive RI for triggering combustion instability under each mode. When the combustor length was short (Fig. 4.20(a), L_{comb} = 458 mm), the pressure and heat release rate perturbations were in phase at the first acoustic mode of the combustor (≈900 Hz), and instability consequently occurred at the first acoustic mode frequency. However, when the combustor length was long (Fig. 4.20(b), L_{comb} = 858 mm), the pressure and heat release rate perturbations were out of phase at the first acoustic mode of the combustor (≈450 Hz) but in phase at the second acoustic mode (≈900 Hz); therefore, instability occurred at the second acoustic mode frequency. In other words, increasing the combustor length shifted instability from the lower mode to the higher mode, as shown in Figs. 4.18 and 4.20.

As with the O/F ratio of 6.26, instability mode shifting occurred on varying the combustor length under all O/F ratios. Under each O/F ratio, the pressure perturbation was significantly amplified at a particular frequency. Figure 4.21 shows the pressure perturbation ($p'/\bar{p}$) in terms of the instability frequency under different O/F ratios (4.0, 6.26, and 8.54).

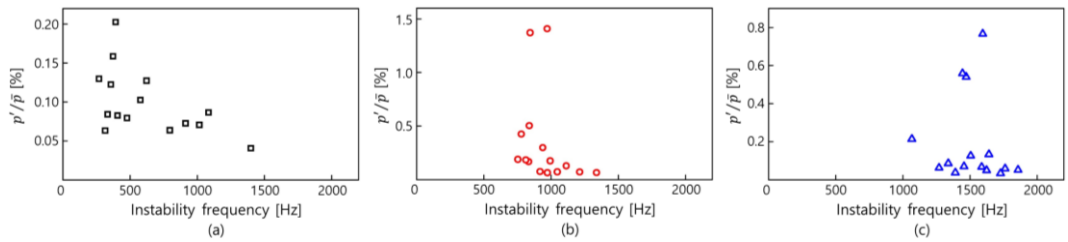

Fig. 4.21 Frequency and strength of instability under O/F ratios of (a) 4.0, (b) 6.26, and (c) 8.54 obtained by varying the combustor length (L_{comb} = 458–1158 mm).

Under O/F ratio = 4.0, most instabilities occurred in the first mode, and the strongest perturbation was measured at approximately 400 Hz. However, at O/F ratio = 6.26, instability occurred from the first mode to the third mode, and the strongest perturbation occurred at a frequency of approximately 900 Hz. Furthermore, under O/F ratio = 8.54, the instability occurred from the second mode to the fifth mode, and the strongest perturbation

occurred at a frequency of approximately 1500 Hz. The frequency at which the strongest perturbation occurs under each O/F ratio refers to the frequency of the perturbation in which each flame is most vulnerable, indicating the inherent characteristics of each flame. These inherent characteristics are closely related to the shape and velocity of the flame, which are the key parameters of τ_{total}.

Figure 4.22 shows the combustion instability frequency according to τ_{total}. As observed in Fig. 4.15, because the combustor length is constant at L_{comb} = 1158 mm, pressure perturbation occurs only at the frequency corresponding to the longitudinal harmonic mode of the combustor. However, Fig. 4.22 shows the frequency with the strongest perturbation among those generated using various combustor lengths; therefore, the combustion instability frequency is inversely proportional to τ_{total} rather discontinuously changing according to τ_{total} as indicated in Fig. 4.15.

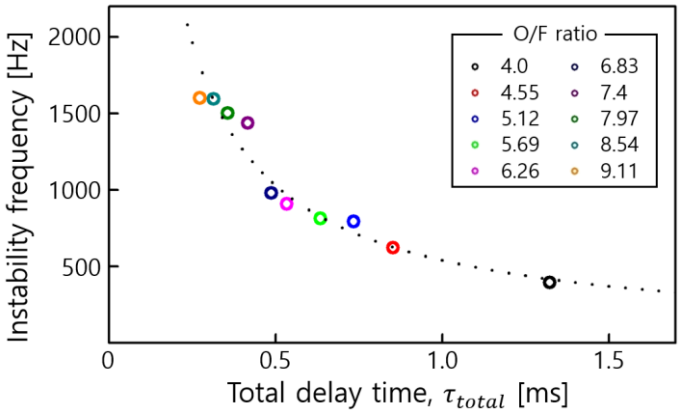

Fig. 4.22 Combustion instability frequency according to τ_{total}.

Based on the calculated τ_{total}, Fig. 4.23 shows the relationship between the ratio of the total delay time to the acoustic period (τ_{total}/T) and the combustion instability strength ($p'/\bar{p}$) under different conditions (O/F ratio = 4.0–9.11, L_{comb} = 458–1158 mm). According to the time-lag analysis, described in Fig. 4.1, and previous studies [9, 10, 129], the pressure and heat release rate perturbation inside the combustor are in phase when

$\tau_{total}/T = n - 1/2$ $(n = 1,\ 2,\ \cdots)$. As shown in Fig. 4.23, a strong pressure perturbation occurs under unstable conditions ($0.25 < \tau_{total}/T < 0.75$) where $-90° < \theta_{p'-q'} < 90°$, resulting in a constructive interaction between p' and q'.

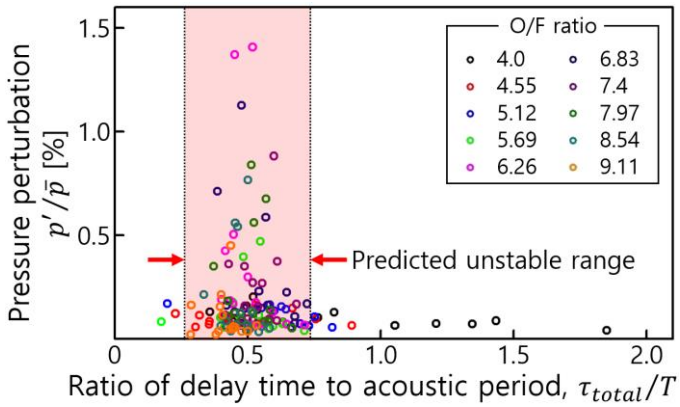

Fig. 4.23 Pressure perturbation ($p'/\bar{p}$) based on the ratio of the total delay time to the acoustic period (τ_{total}/T) (O/F ratio = 4.0–9.11, L_{comb} = 458–1158 mm).

Figures 4.24 and 4.25 show the results of clarifying conditions where the instability occurred by applying time-lag analysis to the results of Figs. 4.18(a) and 4.19. As Figs. 4.24 and 4.25, the strongest pressure perturbation occurred when τ_{total}/T was near 0.5.

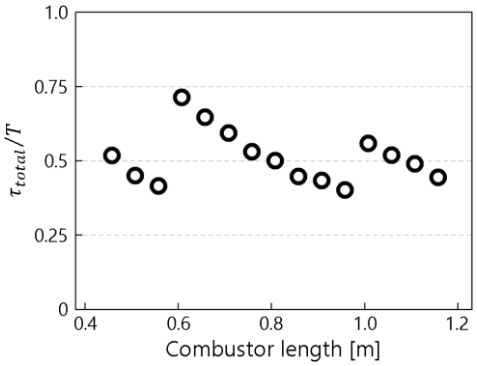

Fig. 4.24 τ_{total}/T according to the combustor length, which is derived by applying the time-lag analysis to Fig. 4.18(a).

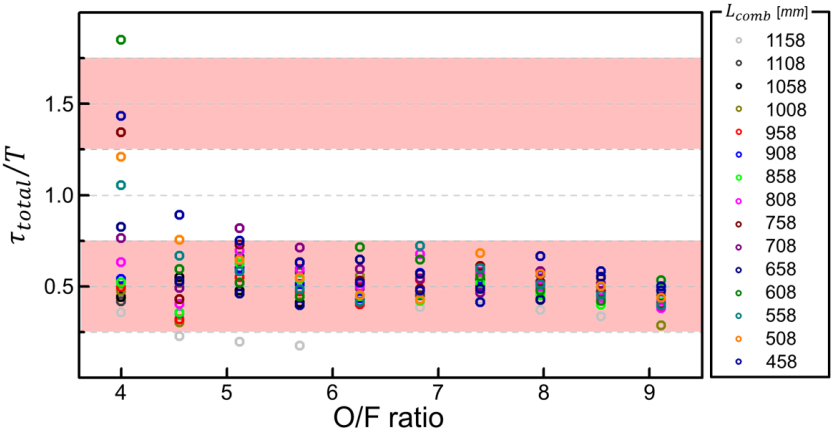

Fig. 4.25 τ_{total}/T according to the O/F ratio, which was derived by applying the time-lag analysis to Fig. 4.19.

As a result, if τ_{total} could be measured, then it would be possible to derive T using τ_{total}/T= 0.5 to calculate the most unstable frequency of the combustion system. As shown in Fig. 4.18(b), the perturbation is considerably amplified when the harmonic resonant frequency of the combustor is consistent with the unstable frequency. Therefore, combustion instability can be avoided by determining the combustor length at a different resonant frequency than the calculated unstable frequency.

Furthermore, to analyze the relationship between the vortex shedding and combustion instability, *St* is calculated when the instability strength is the strongest under each O/F ratio condition. Two conditions should be satisfied for the combustion instability due to the vortex shedding.

First, the Richardson number (*Ri*), which corresponds to the ratio of potential energy to kinetic energy, can be expressed as Eq. (4.8).

$$Ri = \frac{gH\Delta\rho}{\rho_0 \Delta V^2}, \tag{4.8}$$

where g is the gravity constant, H is height, ρ is the density, and ΔV is the velocity difference between two flows.

When *Ri* is less than 0.25, instability occurs between two flows due to vortex shedding, and when *Ri* is greater than 0.25, the perturbation is attenuated and stabilized [136]. In this study, the *Ri* is satisfied with the unstable condition since the *Ri* has an order of from 10^{-5} to 10^{-4}.

Second, *St* of flow should be around 0.2. Figure 4.26 shows the calculated *St* under the tests for combustion instability in this study. Except for the O/F ratio of 4.0, where the ΔV is almost 0, the *St* is calculated between 0.1 and 0.3, indicating that the instability is caused by the vortex shedding. This result is consistent with previous studies [8, 122, 123].

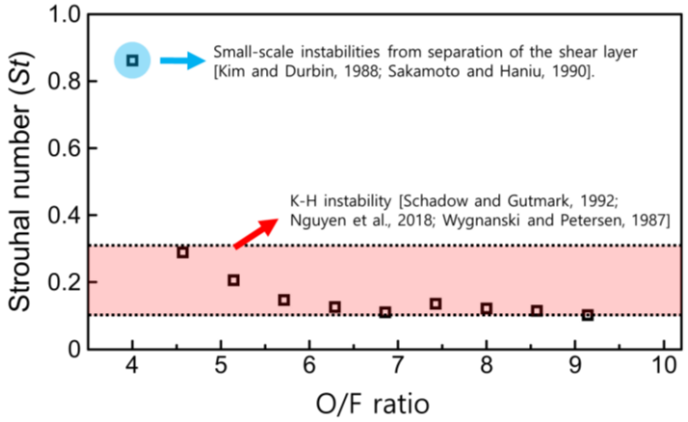

Fig. 4.26 Calculated *St* under the tests for combustion instability in this study.

However, when the O/F is 4.0, the *St* is largely calculated. According to previous work [137, 138], the instability, which occurs at high *St*, is caused by the shear layer separation and has weaker strength than instability caused by the vortex shedding. C.A. Saleel et al. [139] and K.B. Chun and H.J. Sung [140] conducted a study on the instability of the separated shear layer in a backward-facing step duct with a rapidly changing area. In previous studies [140-142], the instability occurred when *St*, calculated using the height of the duct (*H*), was 0.25 or 0.4. In this study, *H* is also used to calculate the *St* under an O/F ratio of 4.0, and as a result, *St* is calculated 0.32. Therefore, it is confirmed that under an O/F ratio of 4.0, the instability is caused by the separated shear layer.

4.7 Effect of Recess on Combustion Instability

The effects of recess were commonly known for improving combustion stability as mentioned in some previous works [23]. Furthermore, Tsohas [143] found that recess did not affect the instability frequencies. However, recent studies have reported that recesses amplified the instability. Candel et al. [144] found that recess amplified instability in the form of vortex in coaxial injectors. Also, An et al. [145] examined the effect of recess on reducing combustion stability in high-pressure environments. In addition, Seo et al. [14] found that recess caused strong pressure perturbations by increasing the acoustic perturbation and internal mixing.

To investigate the effect of recess on the flame stability in this study, a stability map is determined using a non-recessed injector as shown in Fig. 4.27.

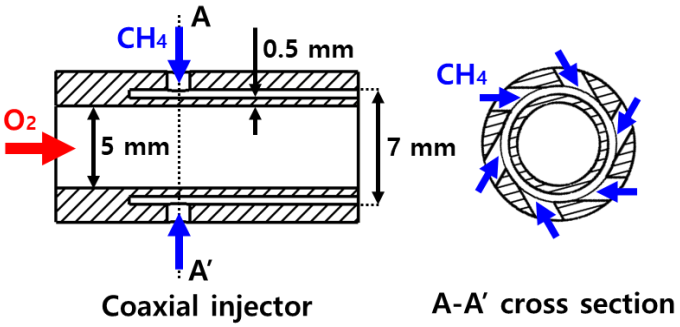

Fig. 4.27 Schematic of cross-sectional view of non-recessed injector.

Figure 4.28 shows the stability maps for the injector with recess and without recess, respectively. Under the fuel-lean conditions, the stable area for the non-recessed injector increased. However, under the fuel rich conditions, very unstable near-blow-off flame, which represents the flame just before the blow off, formed, which were not observed in the recessed injector. In other words, the recess has an effect of increasing the stability under fuel rich conditions, but under the fuel lean condition, it has the effect of widening the area where a flame with strong perturbation occurs.

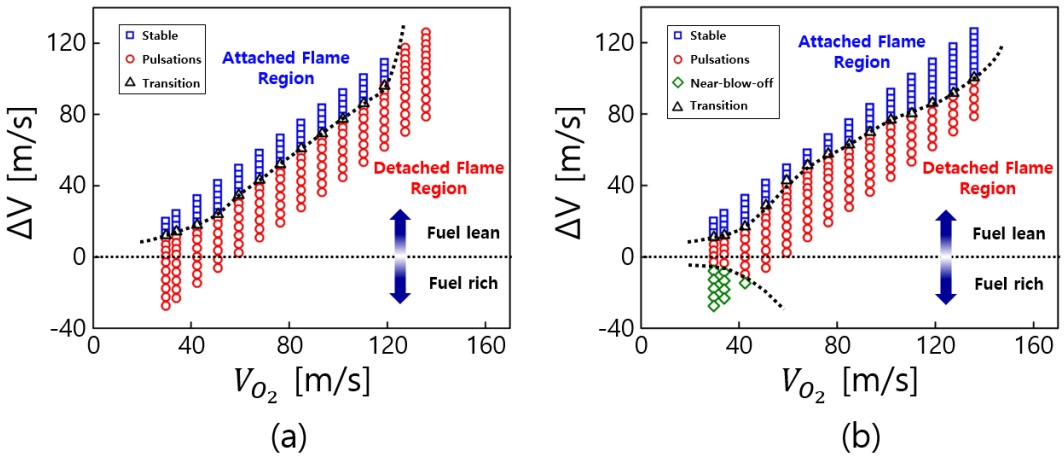

Fig. 4.28 Flame stability map (a) for recessed injector and (b) for the injector without recess in terms of oxygen velocity (V_{O_2}) and velocity difference (ΔV).

Figure 4.29 shows the ratio of the pressure perturbation of the non-recessed injector (RR = 0) to that of the recessed injector (RR = 1), which represents the effect of the recess on damping the pressure perturbation.

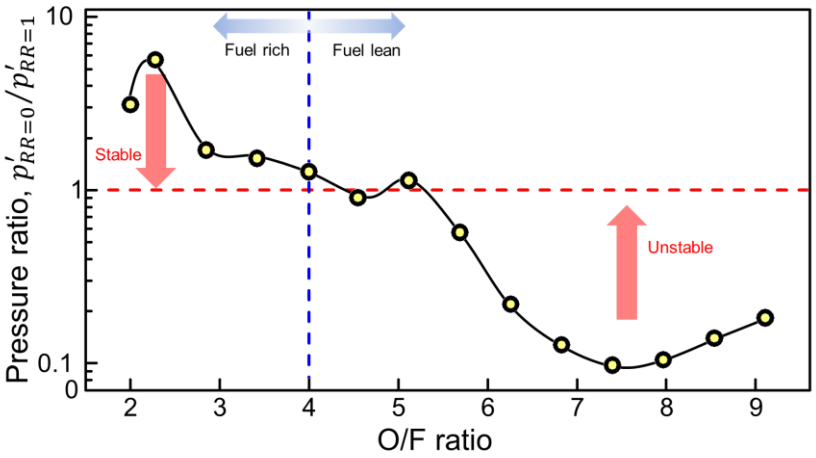

Fig. 4.29 Ratio of the pressure perturbation of the non-recessed injector (RR = 0) to that of the recessed injector (RR = 1) in terms of O/F ratio.

Under fuel rich conditions, the recess has the effect of reducing the pressure perturbation, because a near-blow-off flame with a strong pressure perturbation can be transitioned to a detached flame with a relatively small perturbation owing to the mixing effect inside the recess. However, under the fuel lean condition, pressure perturbation is rather amplified because the stable flame area decreases, which is the same as the phenomenon that instability is amplified in previous studies [14, 144, 145].

To determine whether the recess affects the combustion instability frequency as well, the changes in instability frequency according to the combustor length are measured as shown in Fig. 4.30.

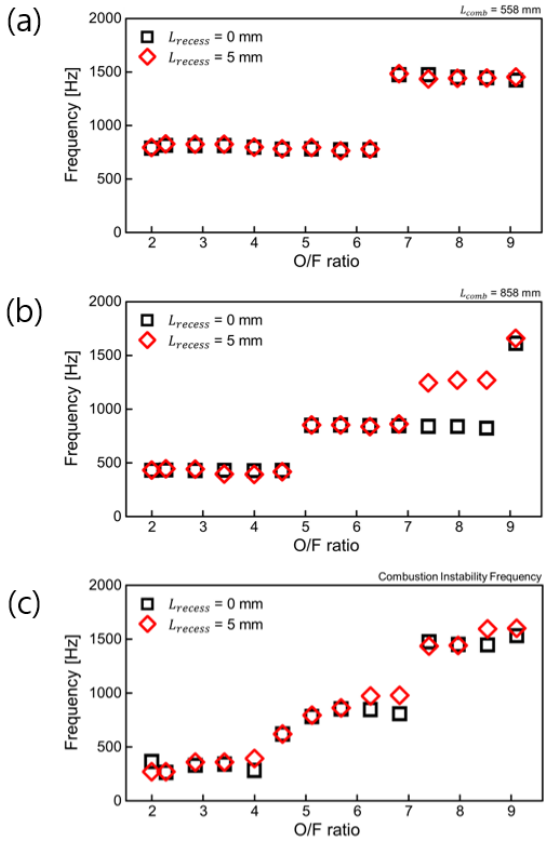

Fig. 4.30 Change in instability frequency according to the O/F ratio when (a) L_{comb} = 558 mm, (b) L_{comb} = 858 mm, and (c) the strongest combustion instability frequency.

Figures 4.30(a) and 4.30(b) show the frequency of pressure perturbation when the combustor length is 558 mm and 858 mm, respectively. Even when the recess length changed, the pressure perturbation occurred in the harmonic mode of the resonant frequency of the combustor. In addition, the tendency of the pressure perturbation mode to increase as the O/F ratio increased was the same even when the recess length was changed. The combustion instability frequency at which the strongest pressure perturbation occurred according to the change in the combustor length was the same despite the change in the recess length as shown in Fig. 4.30(c). Therefore, the recess length has a strong effect on the perturbation strength but has a small effect on the instability frequency.

4.8 Effect of Total Flow Rate on Combustion Instability

Additional experiments are conducted to determine whether the time lag analysis can also be applied to examine the characteristics of combustion instability when the total heat input is changed on varying the methane flow rate. The detailed test conditions of this chapter are summarized in the Table 4.2.

Table 4.2 Summary of the test conditions to examine the effect of total flow rate.

Parameters	**Previous condition (Chapters 4.5 and 4.6)**	**Small flow rate**	**Large flow rate**	**Unit**
Combustor exit condition	Closed end			-
Oxygen flow rate (Bulk velocity at injector exit)	70 ~ 160 (59.4 ~ 135.8)	40 ~ 91.4 (34.0 ~ 77.6)	77.2 ~ 143.4 (65.5 ~ 121.7)	slpm (m/s)
Methane flow rate (Bulk velocity at injector exit)	35 (57.1)	20 (32.6)	38.6 (63.0)	slpm (m/s)
O/F ratio	4.0 ~ 9.11		4.0 ~ 7.4	-
Inlet temperature	290			K
Combustor length	458 ~ 1,158			mm

The characteristics of combustion instability are examined under small and large flow rate conditions. The O/F ratio has an upper limit under the large flow rate condition due to the flow limit of MFC. Figure 4.31 shows the combustion instability frequency, where the strongest pressure perturbation occurred on varying the combustor length, according to the τ_{total} under the small and large flow rate conditions. Although the total flow rate was varied, the flame shape was also changed accordingly, so the τ_{total} did not significantly change. Under both conditions, the combustion instability frequency tended to be inversely proportional to the τ_{total} as with previous results in Fig. 4.22. Furthermore, for a large τ_{total}, the combustion instability frequency shifted to a higher mode. The dotted lines indicate the conditions that the product of the perturbation frequency and the total delay time, which represented the τ_{total}/T, is 0.5 or 1.5.

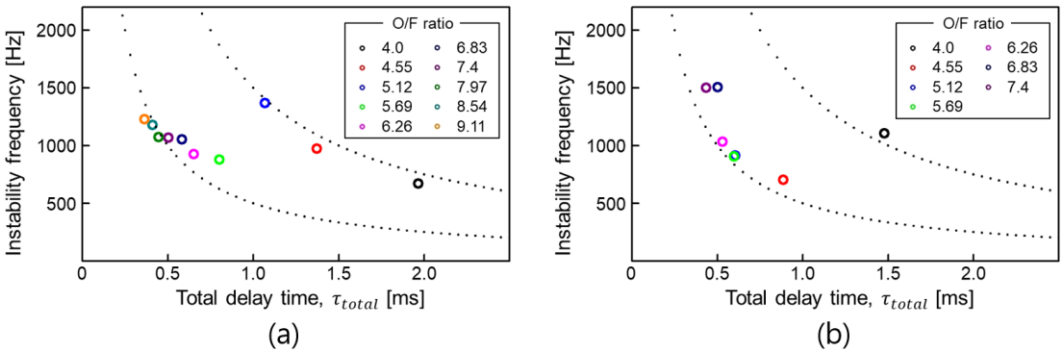

Fig. 4.31 Combustion instability frequency according to τ_{total} under the (a) small and (b) large flow rate conditions, respectively.

Figure 4.32 shows the relationship between the τ_{total}/T and $p'/\bar{p}$ under all experimental conditions at the methane flow rate of 20 slpm (O/F ratio = 4.0–9.11, L_{comb} = 458–1158 mm) and 38.6 slpm (O/F ratio = 4.0–7.4, L_{comb} = 458–1158 mm). As a result, the strong pressure perturbation occurs when τ_{total}/T is 0.5 or 1.5 as with previous results in Fig. 4.23

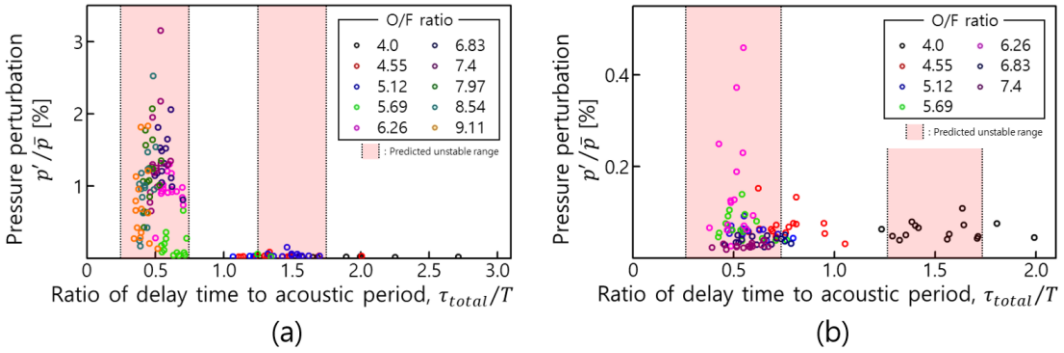

Fig. 4.32 The $p'/\bar{p}$ based on the τ_{total}/T under the (a) small and (b) large flow rate conditions (O/F ratio = 4.0–9.11, L_{comb} = 458–1158 mm).

Figure 4.33 shows the results of three flow conditions at once. The trends for combustion instability frequency and the $p'/\bar{p}$ are the same for each flow condition.

Therefore, it is confirmed that the time lag analysis can be applied to examine the characteristics of combustion instability regardless of the total flow rate.

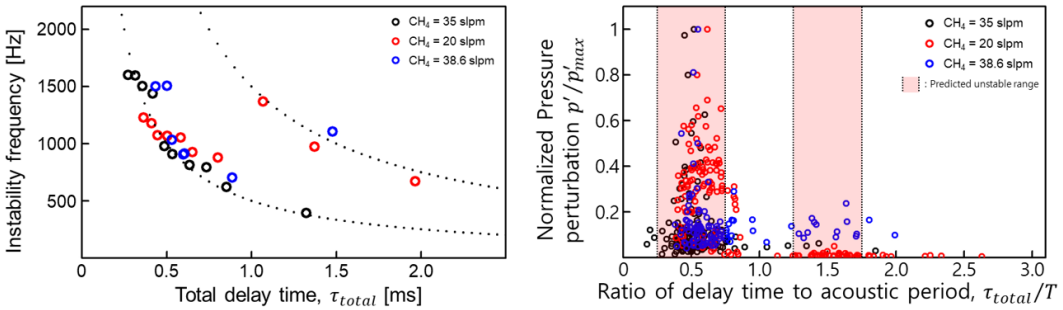

Fig. 4.33 (a) Combustion instability frequency according to the τ_{total} and (b) the $p'/\bar{p}$ based on the τ_{total}/T under each total flow rate condition.

In this study, the effects of the delay time on the combustion instability characteristics in a single-element combustor with a coaxial injector are investigated. In conclusion, τ_{total} of a non-premixed flame formed by a coaxial injector, which can vary the Rayleigh's index, is a key parameter in determining the combustion instability characteristics. In particular, the combustion instability strength and frequency can be adjusted by varying τ_{total} or the combustor length. In other words, varying the τ_{total} and combustor length can cause the instability mode shifting.

CHAPTER 5

FLAME TRNASFER FUNCTION

5.1 Background and Objectives

According to a report on the causes of failure in space vehicle launches around the world [1], investigated by the FAA in the United States of America, problems related to propulsion are the most common reasons. A typical reason for propulsion problems is a combustion instability. Combustion instability is the result of constructive interference between the perturbations of pressure and heat release rate, which can cause a significant increase in these perturbations inside the combustor. Strong combustion instability can lead to the severe perturbations of pressure and heat release rate, which can cause the engine damage or explosion. Therefore, to ensure a successful launch, the frequency of combustion instability needs to be predicted to avoid or reduce the combustion instability in the development process.

In previous studies, Crocco [146] defined the *n*-tau model to predict the combustion instability, where a stability curve was drawn to determine whether a combustion instability occurred. Ducruix et al. [147] compared the experimental and theoretical transfer functions of a laminar premixed flame and investigated its dynamical behavior. However, compared to premixed flames, not much research has been conducted on combustion instability [13] and the effect of delay time on combustion instability for non-premixed flames. Furthermore, only a small range of modulation frequencies has been used to measure FTF in previous research.

Therefore, in this study, FTFs are measured for varied O/F ratio with applying the wide frequency ranges of acoustic modulation, and the peak frequencies of FTF are compared to the combustion instability frequencies, which are measured in Fig. 4.22 in Chapter 4.6. Finally, combustion instabilities are predicted using a 1-D lumped network model.

5.2 Experimental Methods

The atmospheric single element combustor used for measuring FTF in this study is shown in Fig. 5.1. The downstream of the combustor is set as an open boundary condition without a plug nozzle and downstream combustor to remove the acoustic boundary effect of the combustor.

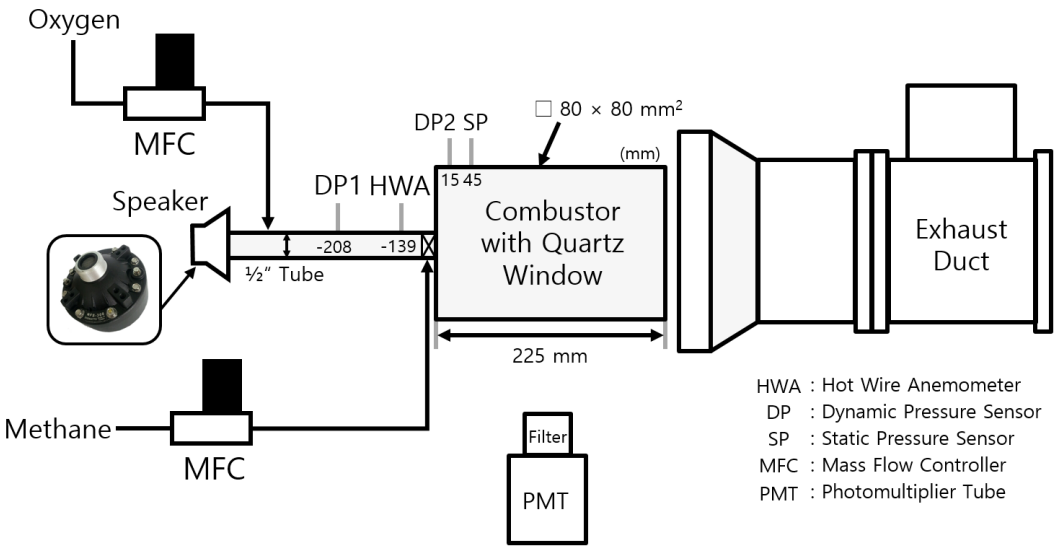

Fig. 5.1 Schematic of the single element combustor for measuring FTF.

Acoustic perturbations are applied with a speaker (Sammi, NFS-300) for single frequency modulation under oxygen flow. The modulation frequency is varied from 0 to 2000 Hz. According to the previous studies [48, 86], the gain and phase of FTF depend on the amplitude level of the input. Thus, the velocity fluctuation in the denominator of the FTF is kept constant at 5% of the mean velocity.

Gaseous oxygen (O_2, 70–160 slpm, purity > 99.9 mol%) and gaseous methane (CH_4, 35 slpm, purity > 99.95 mol%) at 290 ± 5 K are supplied by a MFC (LineTech, M3300V, uncertainty = ± 1% of full range) through a center jet and an annular swirled jet, respectively. The flame characteristics are obtained by calculating the FTF using Eq. (2.7), where the

input function is the inlet velocity fluctuation in the center flow [79], measured by HWA (Dantec, MiniCTA), and the output function is the perturbation of the volume-integrated heat release rate, measured by PMT (Hamamatsu, H7732-10) with the OH^* filter. The detailed test conditions of this chapter are summarized in the Table 5.1.

Table 5.1 Summary of the flame transfer function test conditions.

Parameters	**Bistable flame**	**Combustion instability**	**unit**
Combustion exit condition	Open end		-
Oxygen flow rate (Bulk velocity at injector exit)	50 (42.4)	70 ~ 160 (59.4 ~ 135.8)	slpm (m/s)
Methane flow rate (Bulk velocity at injector exit)	35 (57.1)		slpm (m/s)
O/F ratio	2.85	4.0 ~ 9.11	-
Inlet temperature	290		K
Oxygen Reynolds number	13,280	18,592 ~ 42,497	-
Methane Reynolds number	23,268		-
Modulation frequency	0 ~ 2,000		Hz
Modulation strength $(u'_{ox}/\bar{u}_{ox})$	5		%

5.3 Non-linearity Depending on Velocity Perturbation

As described in Chapter 2.4, the input and output variables of FTF are the normalized perturbations of velocity ($u'/\bar{u}$) and heat release rate ($q'/\bar{q}$), respectively. According to Kim et al. [128], if $u'/\bar{u}$ exceeds a particular value, non-linearity between $u'/\bar{u}$ and $q'/\bar{q}$ occurs, which changes the FTF. Thus, to measure the FTF under the conditions where $q'/\bar{q}$ and $u'/\bar{u}$ satisfies linearity, the $q'/\bar{q}$ is measured for varied $u'/\bar{u}$ as shown in Fig. 5.2.

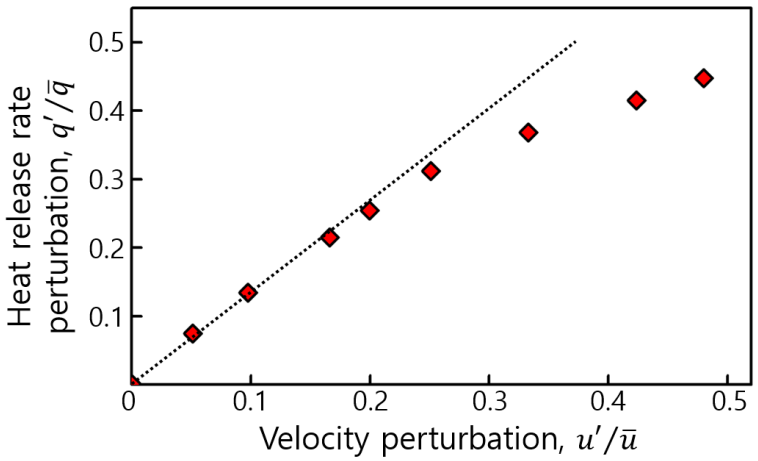

Fig. 5.2 Heat release rate perturbation ($q'/\bar{q}$) according to velocity perturbation ($u'/\bar{u}$). f_{ext} = 200 Hz, O/F ratio = 4.0.

Under the O/F ratio = 4.0 ($\dot{V}_{O_2}$ = 70 slpm, and $\dot{V}_{CH_4}$ = 35 slpm), $q'/\bar{q}$ and $u'/\bar{u}$ varied linearly until $u'/\bar{u}$ = 10% for f_{ext} = 200 Hz. Furthermore, the strengths of combustion instability did not exceed 5% in this study as shown in Chapter 4.6. Therefore, $u'/\bar{u}$, which is the denominator in the FTF, is kept constant at 5% for measuring the FTF. By using a Labview-based data acquisition system to check the real-time FFT of velocity during the combustion experiment, the voltage of the speaker is adjusted to keep $u'/\bar{u}$ near 5%. Figure 5.3 shows the measured $u'/\bar{u}$ according to the modulation frequency under the O/F ratio = 4.0.

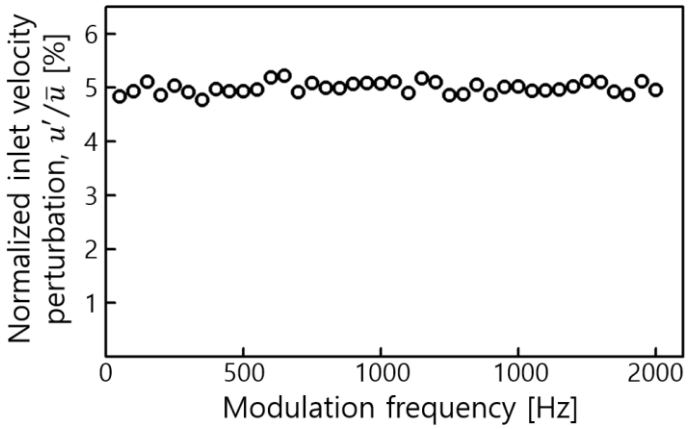

Fig. 5.3 Normalized inlet velocity perturbation ($u'/\bar{u}$) according to the modulation frequency (f_{ext}) with O/F ratio = 4.0 for measuring the FTF.

5.4 Flame Transfer Function for Bistable Flames

The purpose of Chapter 5.4 is to identify whether the bistable flame characteristics affect the FTFs. The typical swirled flame behaves as a low-pass filter [49] because the gain of the FTF for a swirled flame exhibits a typical shape. It starts at 1, increases toward a maximum, decreases to a local minimum at low frequencies [148], and it often reaches a second maximum at higher frequencies [104]. Figure 5.4 shows the FTFs of attached and detached flames under an O/F ratio of 2.85, which also behaves as a low-pass filter with multiple peak values.

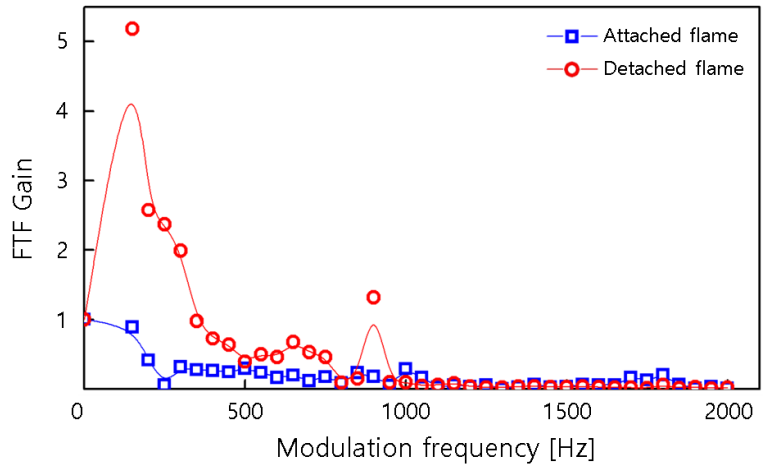

Fig. 5.4 Measured gain of FTFs of attached and detached flames under O/F ratio of 2.85.

The gain of FTF is small for the attached flame, while it has large values for the detached flame, implying that the detached flame is more vulnerable to the external modulation than the attached flame. In particular, in the low frequency region, the difference between the gains of the two FTFs is noticeable. Furthermore, no apparent peak of FTF gain occurs under the attached flame, but, for detached flame, the secondary peak of FTF gain occurs at 900 Hz. Thus, the attached and detached flames have different flame characteristics as identified in Chapter 3, and this differences can also be identified through the FTFs.

Figure 5.5 shows the trend of FTF gain for the detached flame. The flame acts as a low-pass filter as mentioned above, thus the FTF gain decreased as increasing the frequency of modulations. As shown in Fig. 5.5, local maximum values of FTF gain occurred at the modulation frequencies of 150 Hz and 900 Hz, causing a constructive interference between the flame oscillations and heat release rate perturbations. In other words, despite the constant strength of external modulations, strong heat release rate perturbations occurred for external modulations of 150 Hz and 900 Hz, which resulted in local maximum values of FTF gain. In contrast, a local minimum value of FTF gain occurred for external modulation of 500 Hz due to the destructive interaction which caused a small heat release rate perturbation despite the constant strength of external modulation.

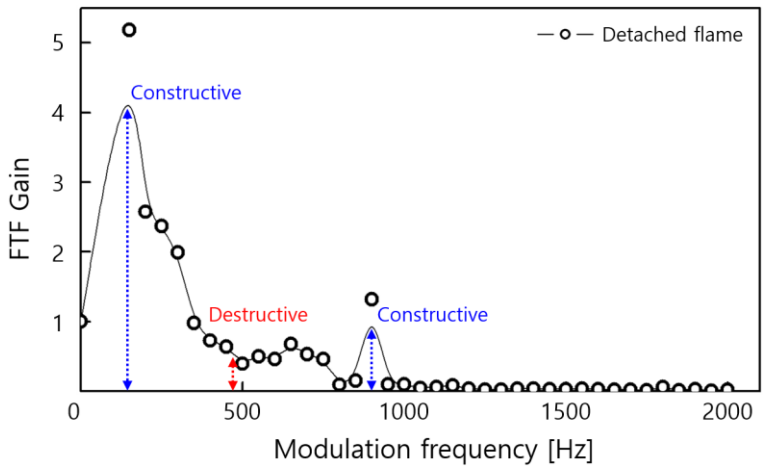

Fig. 5.5 Constructive and destructive interferences between the heat release rate fluctuations and flame oscillations.

Figure 5.6 shows the basic interactions leading to combustion instabilities [6]. When the acoustic perturbation occurs inside the combustor, a feedback loop, which affects the acoustics again owing to various causes, forms. One of the causes is the heat release rate perturbation. Therefore, when the local maximum occurs, perturbations of pressure and heat release rate cause constructive interference, resulting in strong heat release

perturbations. On the other hand, when the local minimum occurs, destructive interference occurs, resulting in relatively small perturbations in the heat release rate.

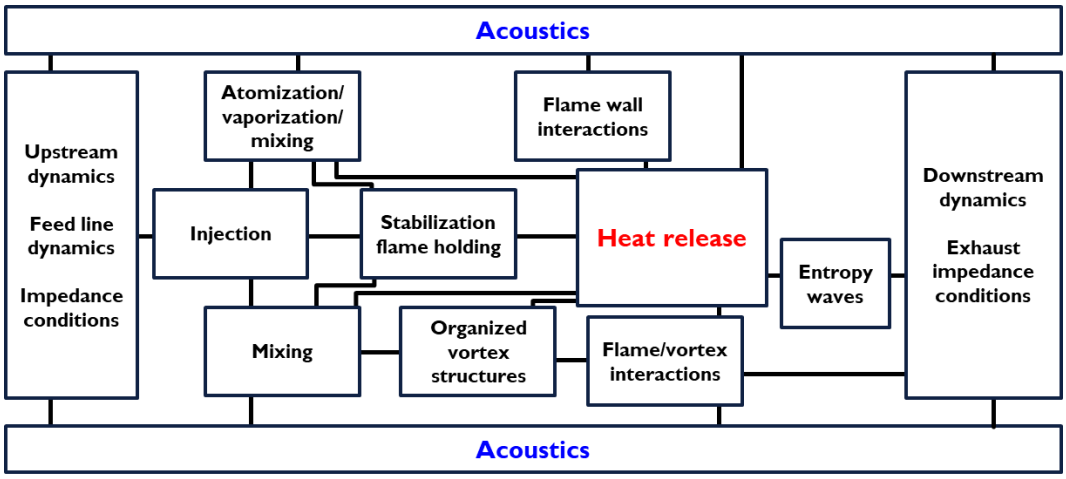

Fig. 5.6 Relationship between the acoustics of combustor and the heat release rate perturbation [6].

5.5 Flame Inherent Characteristics

The purpose of Chapter 5.5 is to identify the relationship between the combustion instability characteristics, explored in Chapter 4, and FTFs. Figure 5.7 shows the FTF under O/F ratio = 6.26. The dominant peak of the FTF gain occurs at a modulation frequency of 950 Hz, implying that the flame is most vulnerable near 950 Hz. As shown in Fig. 4.22 in Chapter 4.6, when the O/F ratio is 6.26, the frequency of combustion instability is approximately 900 Hz, which is close to the frequency of the dominant FTF peak.

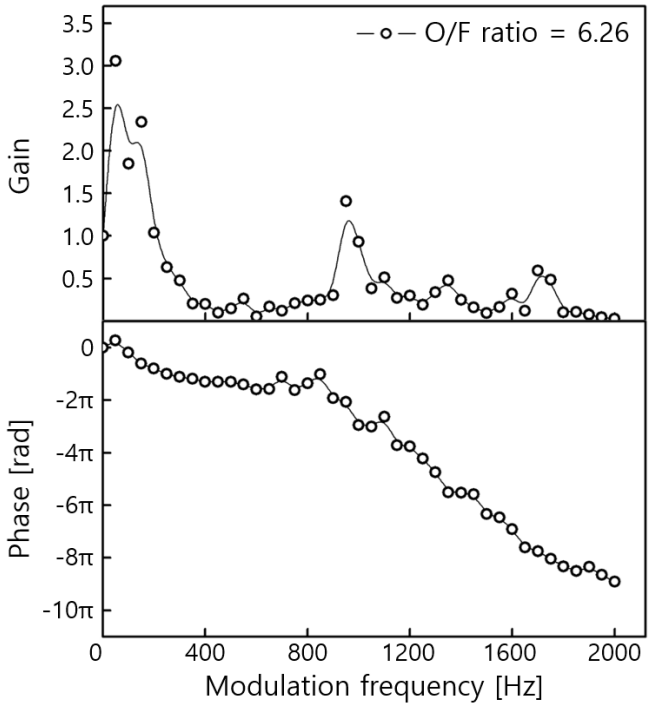

Fig. 5.7 Measured gain and phase of flame transfer function (FTF) under O/F ratio of 6.26.

To investigate the relationship between the frequencies of FTF peak and of combustion instability, the FTFs are measured under all O/F ratios. Figure 5.8 shows the gains of measured FTF under the O/F ratios of 4.0, 6.26, and 8.54. As the O/F ratio increased, the peak frequency of the FTF gain gradually increased.

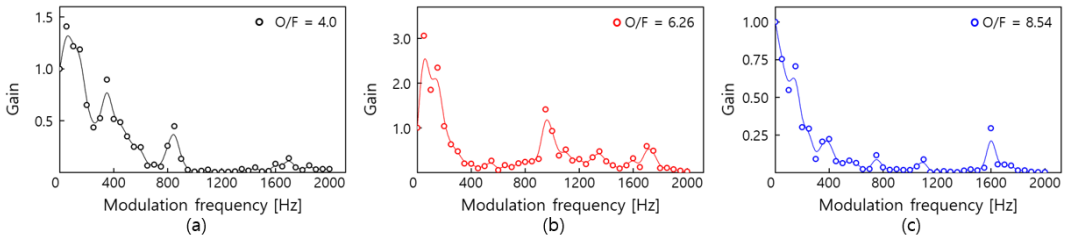

Fig. 5.8 Gains of measured FTF under the O/F ratios of (a) 4.0, (b) 6.26, and (c) 8.54, respectively.

Figure 5.9 shows the frequencies where the FTF peak occurs for each O/F ratio along with the frequencies of combustion instability (depicted in Fig. 4.22 in Chapter 4.6), and the x-axis is indicated by the τ_{total} corresponding to each O/F ratio.

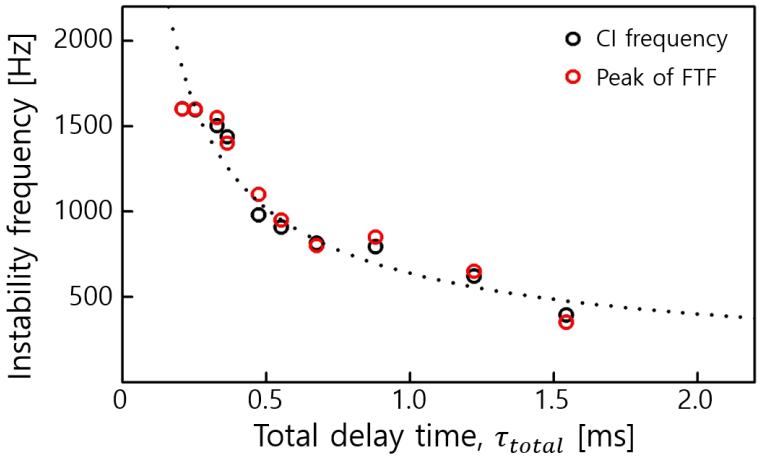

Fig. 5.9 Frequencies of combustion instability and FTF peak according to τ_{total}.

The frequencies of FTF peaks also decreased on increasing τ_{total} and were almost identical to the combustion instability frequencies. The FTF represents the response characteristics of the flame caused by external acoustic modulation; therefore, the FTF peak at a particular frequency indicates the inherent flame characteristics implying that the flame is most vulnerable to external perturbation at that frequency.

When the downstream of the combustor is set as a closed boundary condition, the perturbations corresponding to the resonant frequencies of the combustor are greatly amplified by the resonance with the acoustics of combustor. If the inherent instability frequency of flame coincides with the resonant frequency of combustor, the perturbations corresponding to that frequency are greatly amplified and then are applied to the flame to cause stronger perturbations, which result in the resonance inside the combustor. This positive feedback causes a strong perturbation, corresponding to the particular frequency, causing the combustion instability as shown in Fig. 5.10. During the FTF measurement, since external modulation by a speaker is applied instead of the amplification by the acoustics of combustor, both the combustion instability frequency and FTF peak frequency indicate the inherent characteristics of the flame, and therefore, they match well, as shown in Fig. 5.9.

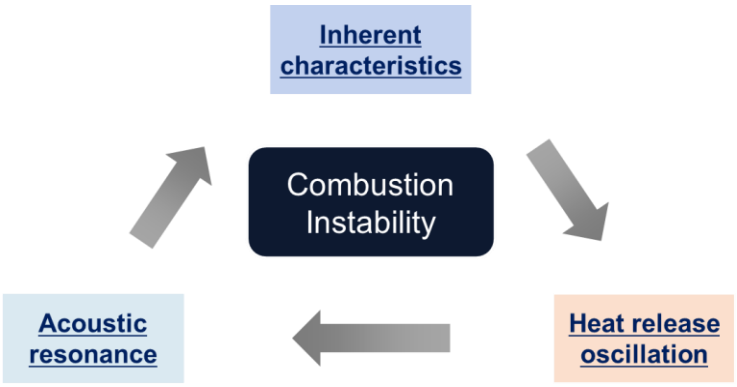

Fig. 5.10 Schematic mechanism for combustion instability.

5.6 Relationship between Flame Area Change and FTF

As mentioned in Chapter 2.4, the flame disturbances cause a change in the flame area, resulting in the heat release rate perturbations. Therefore, OH^* chemiluminescence images are captured using a high-speed CMOS camera to identify the effect of the flame area on the gain of FTF.

The flame area change rate is calculated using the flame area transfer function (FATF) defined by Eq. (5.1), which uses the flame area instead of the heat release rate in the FTF equation expressed as Eq. (2.7).

$$\mathrm{FATF}(\omega) = \frac{A'/\bar{A}}{u'/\bar{u}}, \tag{5.1}$$

where A is the flame area determined by OH^* chemiluminescence images.

Figure 5.11 shows the gains of FTF and FATF under the O/F ratios of (a) 2.85 and (b) 6.26. A very large area change occurred at a low frequency of 150 Hz for both O/F ratios of 2.85 and 6.26. Furthermore, in both cases, the perturbations of the flame area were large at the frequency corresponding to the local maximum of the FTF and were small at the 500 Hz which represented the local minimum of the FTF. Therefore, as mentioned in Chapter 2.4, the change in the flame area affected the perturbation of the heat release rate, which caused the variation in FTF.

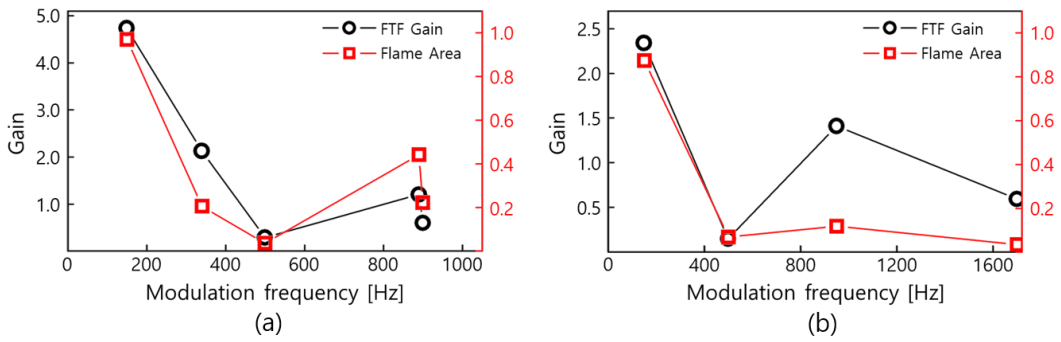

Fig. 5.11 Gains of FTF and FATF under the O/F ratios of (a) 2.85 and (b) 6.26.

5.7 Relationship between Combustion Instability and FTF

To understand the relationship between combustion instability and FTF, the phase of the FTF is analyzed. However, in this study, it was difficult to apply time-lag analysis directly because the velocity perturbations, which are the denominators of the FTF, were measured through HWA in the feed line. Therefore, it is necessary to determine the heat release rate perturbations according to the velocity perturbations at the exit of oxygen post so that the time-lag analysis can be applied. Figure 5.12 shows the locations of sensors to measure the modified FTF phase. In the non-reacting condition, another HWA is mounted to measure the velocity immediately after the injector exit.

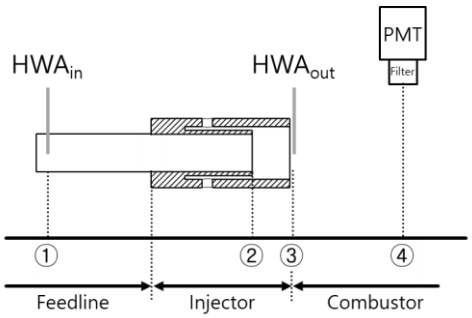

Fig. 5.12 Schematic of device configuration to measure the modified FTF phase.

In addition, under the O/F ratio of 6.26, the phase differences of the perturbations between each position are shown in Fig. 5.13. Figure 5.13(a) represents the phase of FTF calculated in Chapter 5.5. Figure 5.13(b) shows the phase difference between two velocity perturbations measured at ① and ③ in non-reacting conditions. Assuming that the phase difference measured in Fig. 5.13(b) is linear with distance, the phase difference between the perturbations measured at ② and ④ was calculated using the results in Figs. 5.13(a) and 5.13(b). Therefore, the phase shown in Fig. 5.13(c) represents the FTF phase for applying the time-lag analysis and it is almost linear in the low-frequency region, but the nonlinearity increases as the modulation frequency increases.

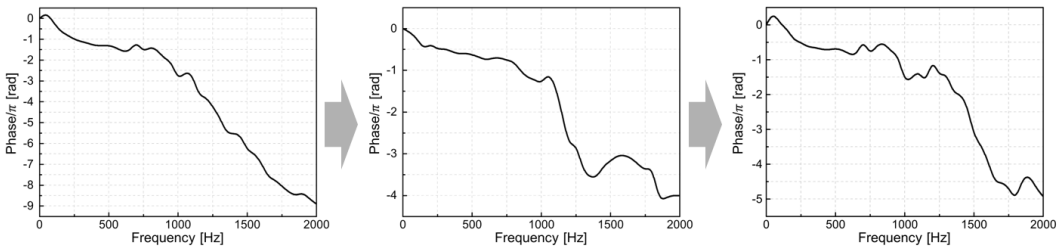

Fig. 5.13 Phase correction to determine the modified FTF phase under O/F ratio of 6.26; phase difference between (a) ① and ④ (reacting), (b) ① and ③ (non-reacting), and (c) ② and ④ in Fig. 5.12.

For the flame characteristics to be linear with the modulation frequency, the flow around the flame should be incompressible. When the wavelength of the acoustic perturbation is very large compared to the flame height, the flow around the flame can be assumed to be an incompressible flow. Therefore, as the modulation frequency increases, the wavelength decreases and the compressibility effect increases, resulting in nonlinearity.

The measured velocity perturbation in Fig. 5.13 is the velocity perturbation of oxygen, so the perturbations of velocity and equivalence ratio have a phase difference of 180 degrees. Therefore, as shown in Fig. 4.1, when the FTF phase satisfies the $(1-2n)\pi$ $(n = 1, 2, \cdots)$, the constructive interference occurs between the pressure inside the combustor and the heat release rate, resulting in combustion instability. Figure 5.14 shows the result of identifying the unstable condition using the time-lag analysis on the FTF phase. As a result, the frequencies between 250 Hz and 1300 Hz were identified as unstable regions. As shown in Fig. 4.18, the instability occurred between 750 Hz and 1300 Hz, which was included in the predicted unstable conditions, on varying the combustor length. Furthermore, at the O/F ratio of 6.26, the peak frequency of the FTF occurred at 950 Hz as shown in Fig. 5.7, and the combustion instability frequency was about 900 Hz similar to the peak frequency of FTF as shown in Figs. 4.21 and 4.22.

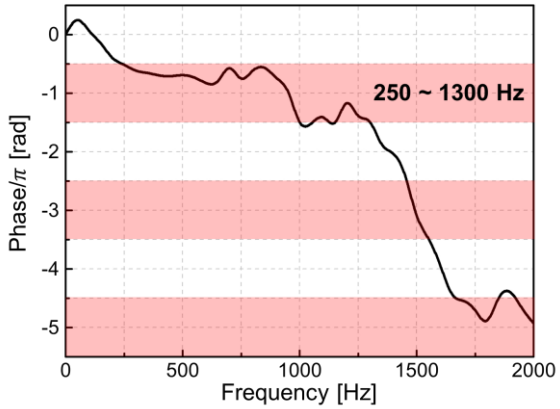

Fig. 5.14 Results of time-lag analysis on the FTF phase.

In a previous study [128], as in this study, the combustion instability was also roughly predicted through the peak frequency of FTF gain and FTF phase, so it is confirmed that the FTF is a key parameter for predicting the combustion instability.

5.8 Instability Prediction

If the combustion instability can be accurately predicted in the engine design process, a very stable engine can be developed under operating conditions. However, due to the non-linearity and complexity, there are many obstacles in predicting the combustion instability for large-scale commercial combustors. Therefore, numerous studies on combustion instability have been conducted to reach the final goal of accurately predicting the combustion instability. As a result, a prediction technique using a FTF has been proposed for predicting the combustion instability occurring in a lab-scale premixed combustor, thus, an accurately measured FTF is a key parameter for predicting the combustion instability. The flame used in this study is a non-premixed flame. However, the studies on prediction of combustion instability for non-premixed flames have not been sufficiently conducted compared to those for premixed flames. Therefore, in this study, approximate combustion instability characteristics are predicted using OSCILOS which is a tool for predicting combustion instability of premixed flames using the Helmholtz equation solver.

The combustion instabilities using methane are predicted under the geometry conditions of each combustor length. The experimentally measured FTFs are used after converted to a state-space model, and the reflection coefficients of the inlet and outlet of the combustor are selected as -1 and +1 through the assumption of open and closed boundaries, respectively. The flame concept of OSCILOS is a premixed thin flame, so the flame in this study is assumed as a thin flame which is formed at a specific location ($F_{Location} = L_{base} + L_{center}$) based on the measured flame shape depicted in Fig. 4.11(a) in Chapter 4.5.1.

Figure 5.15 shows the combustor configuration and flame location for using OSCILOS to predict the combustion instability. The analysis is performed assuming the region from the recess to the nozzle as the combustor and assuming that the flat flame is located at the measured flame center (red line in Fig. 5.15) according to each condition. In addition, the analysis is performed by setting the upstream as an open condition and the downstream as a closed condition.

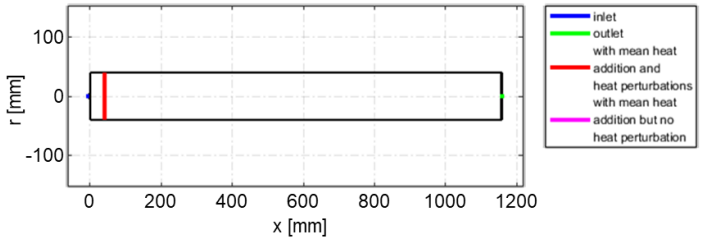

Fig. 5.15 Combustor configuration and flame location for using OSCILOS.

Figure 5.16(a) shows the instability frequencies experimentally measured for varied O/F ratio, and Fig. 5.16(b) shows the predicted instability frequency by OSCILOS. Due to various limitations and differences between experimental conditions and basic model of OSCILOS, there are some differences between the results of experiment and prediction. However, the tendency for an instability mode shifting to a higher mode with an increase in the O/F ratio was successfully predicted. The representative cause of the errors might be the heat loss from the combustor, so the instability frequency in the experiment was measured as smaller than the instability frequency predicted by OSCILOS.

Figure 5.17 shows the change in instability frequency on increasing the combustor length from 458 mm to 1,158 mm under the fixed O/F ratio of 6.26. The instability frequencies predicted through the OSCILOS were very similar to the experimental result, and the combustor lengths where the instability mode transition occurs were predicted accurately. As shown in Fig. 5.17(b), the predicted error of the instability frequency increased as the combustor length increased. This might be because as the combustor length increased, the volume of the combustor increased, resulting in an increase in heat loss. In addition, the repetitive tendency that the growth rate, which represents the strength of instability, becomes stronger and weaker as increasing the combustor length was also well predicted. Furthermore, the combustor lengths with high strength of the instability were also predicted very similarly.

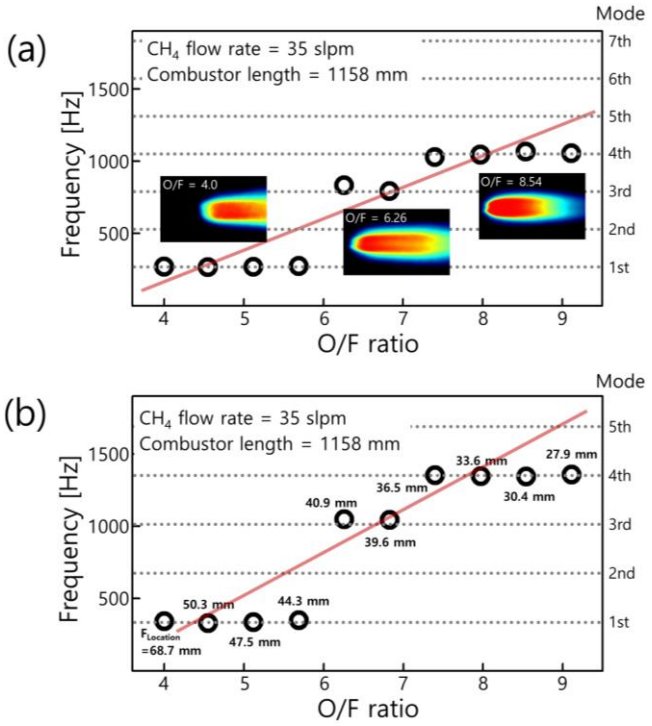

Fig. 5.16 Instability mode shift phenomenon for varied O/F ratio; (a) experimental results and (b) flame location considered prediction results.

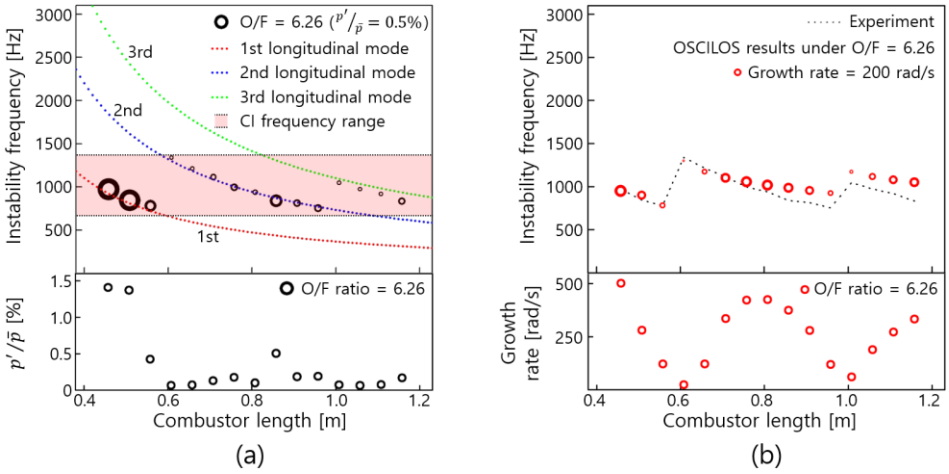

Fig. 5.17 Instability mode shift phenomenon on increasing the combustor length with fixed O/F ratio = 6.26; (a) experimental results and (b) predicted results.

Figure 5.18 shows the measured and predicted results of combustion instability frequency according to each O/F ratio The frequency of combustion instability is defined as the frequency of the perturbation with the largest amplitude among the various perturbations occurring for varied the combustor length (458–1158 mm) in the experimental results (Fig. 5.18(a)) and is defined as the frequency with the largest growth rate in the predicted results (Figs. 5.18(b) and 5.18(c)). Figure 5.18(b) shows the predicted results assuming that the flame is located immediately after the injector without considering the flame location, and Fig. 5.18(c) shows the predicted results using the measured flame locations. The x-axis represents the τ_{total} corresponding to each O/F ratio.

As in the experimental result (Fig. 5.18(a)), the predicted frequencies (Figs. 5.18(b) and 5.18(c)) of combustion instability also tended to decrease as increasing the τ_{total}. If the combustion instability was predicted without considering the flame location (Fig. 5.1(b)), there were some cases where the instability frequencies, which differed greatly from the combustion instability frequencies measured in the experiments, were predicted. Therefore, the tendency of the combustion instability frequency, which is inversely proportional to the τ_{total}, was not properly predicted. However, if the combustion instability was predicted using the flame location (Fig. 5.18(c)) which was determined by measuring the flame shape, the tendency of the combustion instability frequency, which is inversely proportional to the τ_{total}, was well determined, and the instability frequency was predicted similarly to that measured in the experiment.

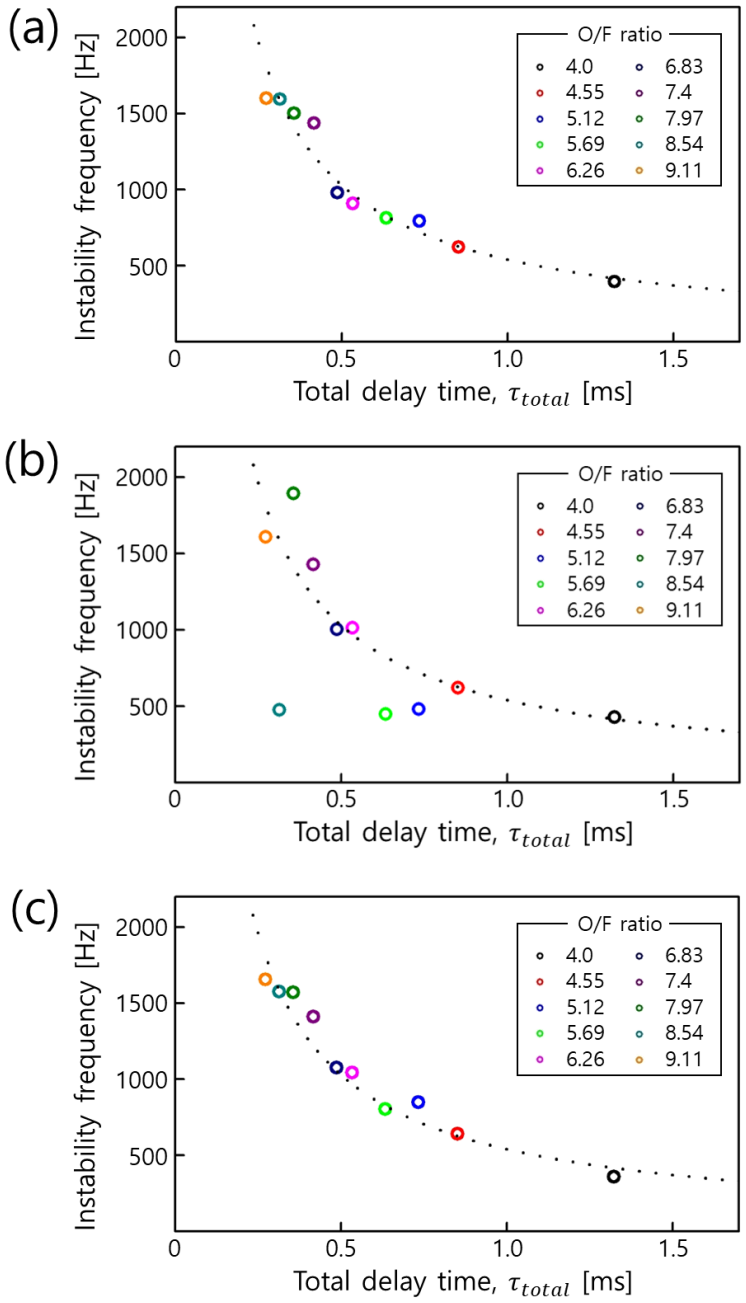

Fig. 5.18 Combustion instability frequency according to τ_{total} (varied O/F ratio); (a) experimental results, (b) predicted results without considering the flame location, and (c) predicted results using the flame location.

To examine the effect of the change in boundary conditions on the predicted results, instability is analyzed by changing the upstream and downstream boundary conditions as shown in Fig. 5.19.

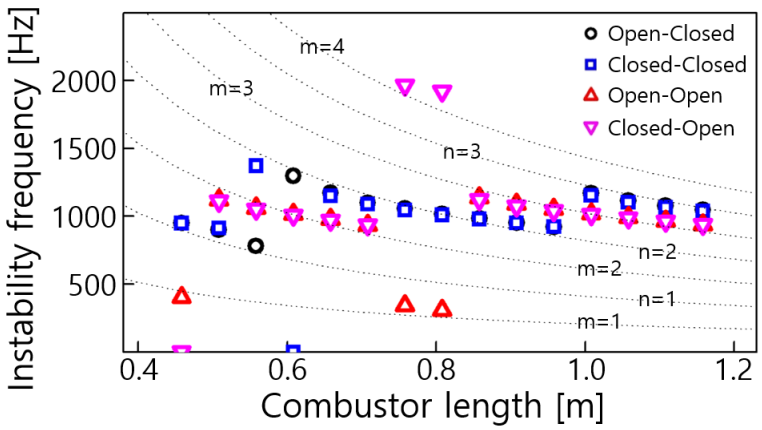

Fig. 5.19 Effect of boundary conditions (upstream-downstream) on OSCILOS analysis.

When the upstream boundary condition was changed to “closed”, the instability was predicted differently for a particular combustor length, which might be an effect of the interaction between the recess and the combustor. However, in most cases, the prediction of the instability frequency did not change significantly. In other words, the effect of the interaction between the recess and the combustor might be small because the recess length was very short compared to the combustor length.

On the contrary, when the downstream boundary condition was changed to "open", the overall trend was predicted the same, except for the cases where different results were predicted in particular combustor lengths by the effect of the recess, as can be seen from the results of the red triangles and purple inverted triangles in Fig. 5.19. However, the instability frequencies were predicted differently from when the downstream was a closed boundary. A closed boundary condition is formed between the recess and the combustor due to the dramatic area change, so when the downstream is a closed boundary, the resonant frequency can be calculated as in Eq. (5.2).

$$f_{closed} = \frac{nc}{2L} \tag{5.2}$$

Conversely, if the downstream is an open boundary, the resonant frequency can be calculated as in Eq. (5.3).

$$f_{open} = \frac{(2n-1)c}{4L} \tag{5.3}$$

The trend of the predicted instability frequency was the same as that of the resonant frequency calculated through Eqs. (5.2) or (5.3) depending on each boundary condition.

Furthermore, to determine the effect of FTF, the prediction results according to the changes in gain and phase of FTF are identified. Figure 5.20 shows the changes in the prediction results of instability when the FTF gain is changed while the phase is fixed. The analyses are performed as the gain is arbitrarily changed from 0.3 times to 1.7 times, and this ratio of FTF gains is defined as the gain factor. As shown in Fig. 5.20, as the gain factor increased, the predicted growth rate increased proportionally.

As a result of the instability frequency prediction, when the gain factor was between 0.9 and 1.4, the same result as the predicted result using the measured FTF was obtained. However, when the gain factor was less than 0.8, the length of the combustor where the instability mode transition occurred changed, but the overall trend was almost the same as shown in Fig. 5.21(a). When the gain factor exceeded 1.5, different instability modes were predicted for particular lengths as shown in Fig. 5.21(b). The reason for this is that if the gain factor is small, the difference in the FTF gains between the peak frequency and other frequencies decreases, so the influence of the FTF gain peak frequency might be relatively reduced. Therefore, instability does not occur at the FTF gain peak frequency so that an accurate prediction has not been made. If the gain factor is very large, although the FTF gain at the peak frequency increases, the FTF gain at other frequencies also increases. Therefore, the influences of not only the peak frequency but also other frequencies might increase, resulting in inaccurate prediction in particular cases.

$$Gain_{using} = Gain\ factor \times Gain_{measured}$$

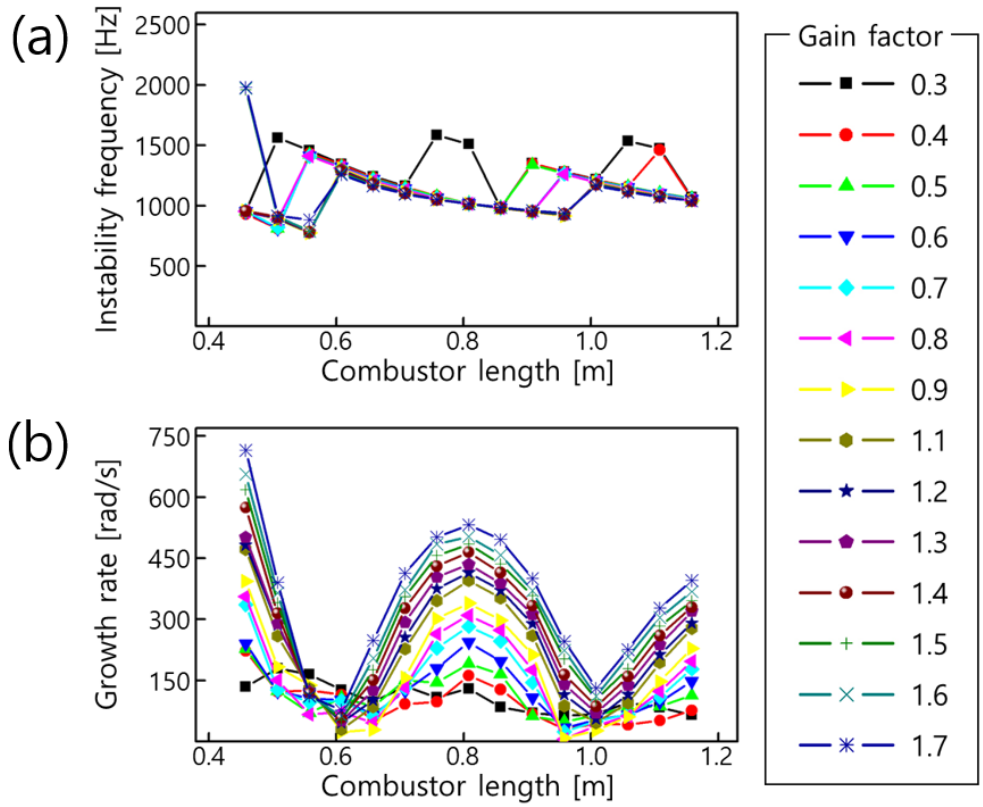

Fig. 5.20 Instability prediction results according to the change in FTF gain.

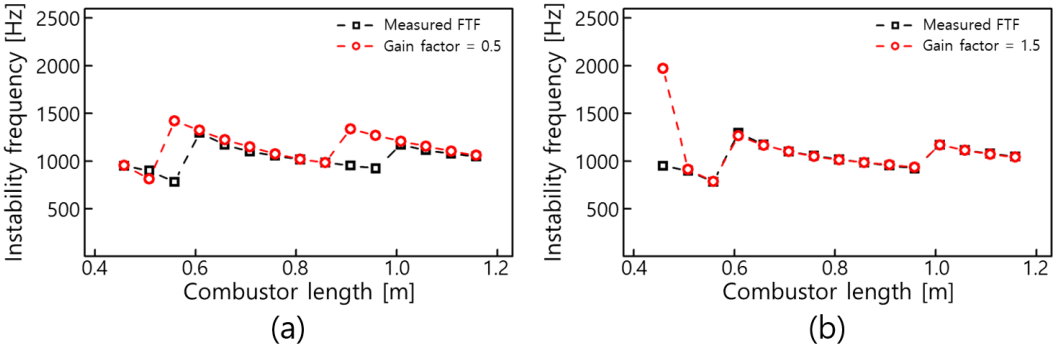

Fig. 5.21 Prediction of instability frequency when the gain factor is (a) 0.5 and (b) 1.5.

Next, to identify the effect of the FTF phase on the prediction of instability, the FTF is applied to the prediction by doubling the FTF phase with the FTF gain is fixed as shown in Fig. 5.22(a). Figure 5.22(b) shows the change in the growth rate according to the change in the FTF phase at the instability frequency predicted using the measured FTF. When the FTF phase was doubled, the growth rate decreased significantly at the predicted instability frequency, and negative growth rates were rather predicted under particular conditions. Therefore, the FTF phase is related to the occurrence of combustion instability, and the FTF gain is related to the strength of combustion instability. In other words, the accurately measured FTF is a key parameter for accurately predicting combustion instability.

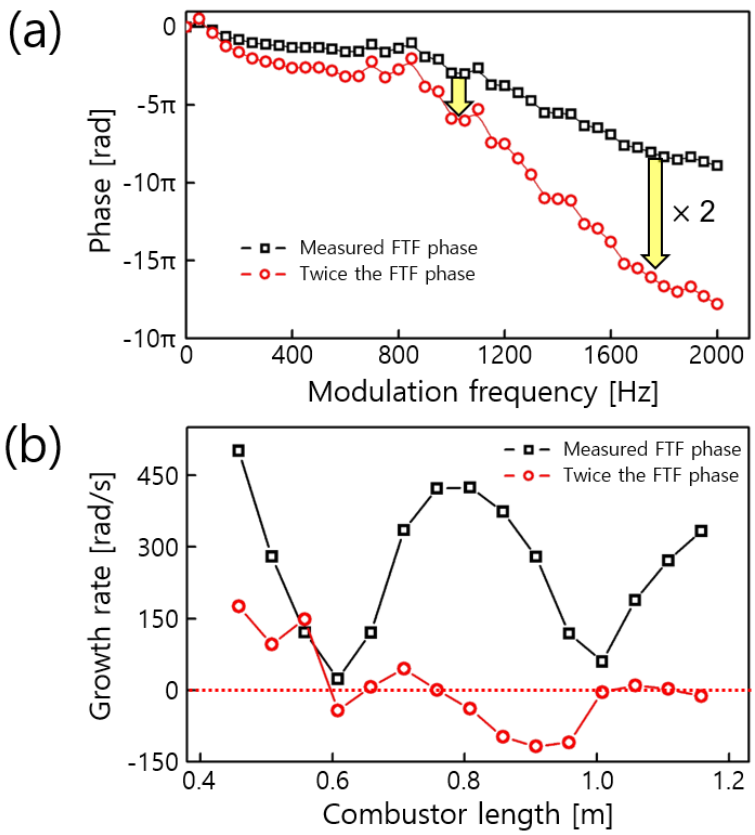

Fig. 5.22 (a) Change in FTF phase and (b) change in the growth rate at the predicted instability frequency when FTF phase is doubled.

Despite various limitations and differences between the concepts of OSCILOS and experimental conditions, the non-premixed flames in this study are assumed as a thin flame using the measured flame center to match the basic concept of OSCILOS. Therefore, the mode shift phenomenon of instability, on varying the O/F ratios and combustor lengths, is successfully predicted similarly to the experimental results. Furthermore, the frequencies of combustion instability are also predicted to be similar to the experimental results. Therefore, the accurately measured flame shape and FTF are identified as the key parameters in the prediction for combustion instability.

In this study, FTFs are measured for varied O/F ratio under the open end boundary condition. First, the difference in the FTFs of the bistable flames is explored, and the FTF gain is larger and the secondary peak also occurs in the case of an unstable detached flame. Then, the relationship between the frequencies of combustion instability and of FTF gain peak is investigated, and both have similar values indicating the inherent instability characteristics of the flame. Finally, using a tool for predicting the combustion instability using measured FTF, the characteristics of combustion instability are roughly predicted.

In conclusion, accurately measured flame shape and FTF are key parameters for predicting the combustion instability. In particular, the flame shape, measured precisely to determine the centroid of flame so that a non-premixed flame can be assumed as a thin flame, overcomes the limitations in differences of flame characteristics when using the conventional tools for predicting the combustion instability of premixed flame.

CHAPTER 6

CONCLUSION

In this study, flame shape and combustion instability characteristics are explored using a recessed coaxial injector in a single element combustor. The high repetition dynamic pressure data measurement and flame visualization technique are applied to investigate the dynamic characteristics of non-premixed flames. The characteristics and reasons of flames formed in different shapes are analyzed despite the same operating conditions. Then, the characteristics of combustion instability and its mode transition are investigated. Finally, the FTF are also measured and analyzed. A summary of the findings is as follows.

First, bistable flame characteristics are investigated experimentally for methane–oxygen flames formed by a recessed coaxial injector. Two different flame shapes, attached and detached bistable flames, are formed, despite constant flow conditions, with distinct stability characteristics. Transitions between the bistable flames can be initiated by varying the ΔV and acoustic modulation strength under oxygen flow. Mixing in the shear layer and perturbation inside the combustor can be the main causes of these transitions, which are investigated by measuring the flame shape changes. Varying the O/F ratio induces the velocity difference between the oxygen and methane, resulting in changes in the flame shapes and perturbation through vortex shedding in the shear layer, which can result in transitions from detached to attached flames. The modulation under oxygen flow has different impacts on the flame shape transitions depending on the perturbation strength. Moderate modulation increases mixing in the shear layer and pulls flames towards the injector, causing transitions from the detached to the attached flame state. However, strong modulation induces severe flow perturbation and pushes flames downstream, causing transitions from attached to detached states. In conclusion, flame shape is a key parameter to consider, in conjunction with the O/F ratio, in evaluating combustion characteristics. In particular, flame stability characteristics can be adjusted by controlling the flame shape through ΔV variation or external modulation application. Thus, flames formed by recessed

coaxial injectors can be stabilized by controlling the operating conditions or external disturbances, despite the constant geometric conditions. In addition, the bistable characteristics should be considered to avoid combustion instability when designing the operating sequence of the engine because the difference in flame shape affects the static and dynamic stabilities of the flame.

Second, the effects of the delay time on the combustion instability characteristics in a single-element combustor with a coaxial injector are investigated. Changes in the instability characteristics owing to variations in the O/F ratio are investigated. Varying the O/F ratio changes the flame shape and speed, which cause the change in τ_{total}. The value of τ_{total} calculated through the time-lag analysis tends to decrease as the O/F ratio increases. As a result, the instability mode is shifted from a higher to a lower mode as τ_{total} increases. Therefore, variation in τ_{total} is the main reason for the change in the instability characteristics. The combustor length is also a key parameter influencing the instability characteristics. Even when τ_{total} is constant, varying the combustor length results in a transition of acoustic modes, satisfying positive RI. Increasing the combustor length causes the instability mode to switch from a lower to a higher mode; thus, instability occurs only in a particular range of frequencies. Furthermore, when the longitudinal harmonic mode of the combustor corresponds to the most unstable frequency, the combustion instability strength is greater than the pressure perturbations obtained with the other combustor lengths. Finally, measuring the frequency where the strongest pressure perturbation occurs by varying the O/F ratio and combustor length reveals that the combustion instability frequency is inversely proportional to τ_{total}. Furthermore, combustion instability occurs only at specific values of τ_{total}/T. In conclusion, τ_{total} of a non-premixed flame formed by a coaxial injector is a key parameter in determining the combustion instability characteristics. In particular, the combustion instability strength and frequency can be adjusted by varying τ_{total} or the combustor length. In other words, a combustion system using a non-premixed flame can be stabilized by controlling the operational or geometric conditions. Furthermore, for the non-premixed flame formed in the recessed coaxial injector used in this study, the combustion instability frequency, where

the strongest pressure perturbation occurs, can be predicted by calculating T for τ_{total}/T = 0.5.

Finally, FTF is measured to explore the inherent instability characteristics of the flame. The FTFs of bistable flames are measured and show different FTF characteristics despite the same operating conditions. Furthermore, under each O/F ratio, the FTF behaves as a low-pass filter with a high gain in the low-frequency region, and multiple peaks occur in the high-frequency region. Furthermore, the gain of FTFs has a peak value at a frequency similar to the frequency where the combustion instability occurs, implying that the inherent instability characteristics of flame can be identified using measured FTF. Also, the results show that the combustion instability can occur when these inherent characteristics are combined with the acoustics of the combustor. In addition, the combustion instability prediction tool, using the location of flame centroid and FTF, successfully predicts the instability characteristics similar to the experimental results. Therefore, accurately measured FTF and flame shape are the key parameters for predicting the combustion instability.

In conclusion, the flame shape should be considered along with the operating conditions such as an O/F ratio to determine the combustion instability characteristics. The τ_{total} and combustor length are the key parameters for determining the mode of combustion instability. Furthermore, the frequency of combustion instability can be determined through the time-lag analysis using the calculated τ_{total} by measuring the flame shapes, implying that the combustion instability can be avoided or reduced by designing the combustor to have a resonant frequency different from the expected instability frequency. In addition, the inherent instability characteristics of flame can be identified by the measured FTFs, and the characteristics of combustion instability can be predicted similar to the experimental results by using the FTF and flame shape. This study is expected to advance our collective understanding of combustion instability mechanisms and provide a means of avoiding combustion instability by applying time-lag analysis to a non-premixed flame.

REFERENCES

[1] N. Demidovich, Launch Vehicle Failure Mode Database, *COMSTAC RLV Working Group (FAA)* 5 (2007).

[2] F.E. Culick and V. Yang, Overview of combustion instabilities in liquid-propellant rocket engines, *Liquid Rocket Engine Combustion Instability* 169 (1995) 3-37.

[3] L. Crocco and S.I. Cheng, Theory of combustion instability in liquid propellant rocket motors, Princeton Univ., Princeton, NJ, 1956.

[4] D.W. Kendrick, T.J. Anderson, W.A. Sowa and T.S. Snyder, Acoustic sensitivities of lean-premixed fuel injectors in a single nozzle rig, In ASME 1998 International Gas Turbine and Aeroengine Congress and Exhibition, 1998, American Society of Mechanical Engineers Digital Collection, p. V003T006A032.

[5] T. Lieuwen, H. Torres, C. Johnson and B.T. Zinn, A mechanism of combustion instability in lean premixed gas turbine combustors, *Journal of Engineering for Gas Turbines and Power* 123 (2001) 182.

[6] S. Candel, Combustion dynamics and control: Progress and challenges, *Proceedings of the Combustion Institute* 29 (2002) 1-28.

[7] U. Hegde, D. Reuter, B. Daniel and B. Zinn, Flame driving of longitudinal instabilities in dump type ramjet combustors, *Combustion Science and Technology* 55 (1987) 125-138.

[8] K. Schadow and E. Gutmark, Combustion instability related to vortex shedding in dump combustors and their passive control, *Progress in Energy and Combustion Science* 18 (1992) 117-132.

[9] T. Lieuwen and B.T. Zinn, The role of equivalence ratio oscillations in driving combustion instabilities in low NOx gas turbines, In Symposium (International) on combustion, 1998, Elsevier, p. 1809-1816.

[10] T.C. Lieuwen, Investigation of combustion instability mechanisms in premixed gas turbines, PhD Thesis, School of Mechanical Engineering, Georgia Institute of Technology, Atlanta, GA, 1999.

[11] H. Merk, An analysis of unstable combustion of premixed gases, In Symposium (International) on Combustion, 1957, Elsevier, p. 500-512.

[12] F. Culick, Combustion instabilities in solid propellant rocket motors, California Inst. of Tech., Pasadena, CA, 2004.

[13] K. Balasubramanian and R. Sujith, Non-normality and nonlinearity in combustion–acoustic interaction in diffusion flames, *Journal of Fluid Mechanics* 594 (2008) 29-57.

[14] S. Seo, Y.M. Han and H.S. Choi, Combustion characteristics of bi-liquid swirl coaxial injectors with respect to a recess, *Transactions of the Japan Society for Aeronautical and Space Sciences* 53 (2010) 24-31.

[15] G. Gill and W. Nurick, Liquid rocket engine injectors, NASA SP-8089, Washington, D.C, (1976).

[16] J.C. Oefelein and V. Yang, Comprehensive review of liquid-propellant combustion instabilities in F-1 engines, *Journal of Propulsion and Power* 9 (1993) 657-677.

[17] G. Dressler and J. Bauer, TRW pintle engine heritage and performance characteristics, In 36th AiAA/ASME/SAE/ASEE joint propulsion conference and exhibit, 2000, p. 3871.

[18] M.J. Casiano, J.R. Hulka and V. Yang, Liquid-propellant rocket engine throttling: a comprehensive review, *Journal of Propulsion and Power* 26 (2010) 897-923.

[19] M. Son, K. Yu, J. Koo, O.C. Kwon and J.S. Kim, Effects of momentum ratio and Weber number on spray half angles of liquid controlled pintle injector, *Journal of thermal science* 24 (2015) 37-43.

[20] W. Peschka, Liquid hydrogen: fuel of the future, Springer Science & Business Media, 2012.

[21] K. Ahn, J.G. Kim and H.S. Choi, Effects of injector recess on heat flux in a combustion chamber with cooling channels, *Aerospace Science and Technology* 37 (2014) 110-116.

[22] K. Ahn, J.H. Kim and Y. Yoon, Application of PIV to over-expanded supersonic flows: Possibilities and limits, *Journal of visualization* 6 (2003) 353-361.

[23] W. Mayer and H. Tamura, Propellant injection in a liquid oxygen/gaseous hydrogen rocket engine, *Journal of Propulsion and Power* 12 (1996) 1137-1147.

[24] W. Mayer and H. Tamura, Flow visualization of supercritical propellant injection in a firing LOX/GH2 rocket engine, In 31st Joint Propulsion Conference and Exhibit, 1995, p. 2433.

[25] V.R. Rubinsky, Combustion instability in the RD-0110 engine, *Liquid Rocket Engine Combustion Instability* 169 (1995) 89-112.

[26] Y. Demyanenko, A. Dmitrenko, A. Ivanov and V. Pershin, Turbopumps for gas generator and staged combustion cycle rocket engines, In 41st AIAA/ASME/SAE/ASEE Joint Propulsion Conference & Exhibit, 2005, p. 3946.

[27] J. Davis, R. Campbell, J. Davis and R. Campbell, Advantages of a full-flow staged combustion cycle engine system, In 33rd Joint Propulsion Conference and Exhibit, 1997, p. 3318.

[28] S. Farhangi, T. Yu, L. Rojas, K. Sprouse and J. McKinnon, Gas-gas injector technology for full flow stage combustion cycle application, In 35th Joint Propulsion Conference and Exhibit, 1999, p. 2757.

[29] W. Marshall, S. Pal, R. Woodward and R. Santoro, Benchmark wall heat flux data for a GO2/GH2 single element combustor, In 41st AIAA/ASME/SAE/ASEE Joint Propulsion Conference & Exhibit, 2005, p. 3572.

[30] R. Balachandran, S.R. Chakravarthy and R.I. Sujith, Characterization of an acoustically self-excited combustor for spray evaporation, *Journal of Propulsion and Power* 24 (2008) 1382-1389.

[31] J. Yoon, S. Joo, J. Kim, M.C. Lee, J.G. Lee and Y. Yoon, Effects of convection time on the high harmonic combustion instability in a partially premixed combustor, *Proceedings of the Combustion Institute* 36 (2017) 3753-3761.

[32] T. Lieuwen and B. Zinn, Theoretical investigation of combustion instability mechanisms in lean premixed gas turbines, In 36th AIAA Aerospace Sciences Meeting and Exhibit, 1998, p. 641.

[33] J.P. Moeck, D. Durox, T. Schuller and S. Candel, Nonlinear thermoacoustic mode

synchronization in annular combustors, *Proceedings of the Combustion Institute* 37 (2019) 5343-5350.

[34] Á . Muelas, J. Carpio, J. Ballester, A.L. Sánchez and F.A. Williams, Pyrolysis effects during high-temperature vaporization of alkane droplets, *Combustion and Flame* 217 (2020) 38-47.

[35] W. De Roeck, W. Desmet, M. Baelmans and P. Sas, On the prediction of near-field cavity flow noise using different CAA techniques, *Aeroacoustics and Flow Noise Proceedings of ISMA*, (2004) 369-386.

[36] E.D. Gonzalez-Juez, Hybrid Computational Fluid Dynamics/Thermoacoustic-Solver Approach to Model Acoustics in Combustion Simulations, *Journal of Propulsion and Power* 34 (2018) 636-646.

[37] Y. Huang and V. Yang, Effect of swirl on combustion dynamics in a lean-premixed swirl-stabilized combustor, *Proceedings of the Combustion Institute* 30 (2005) 1775-1782.

[38] C.E. Martin, L. Benoit, Y. Sommerer, F. Nicoud and T. Poinsot, Large-eddy simulation and acoustic analysis of a swirled staged turbulent combustor, *AIAA journal* 44 (2006) 741-750.

[39] X. Han, J. Yang and J. Mao, LES investigation of two frequency effects on acoustically forced premixed flame, *Fuel* 185 (2016) 449-459.

[40] S. Van Buren, A.C. Miranda and W. Polifke, Large eddy simulation of enhanced heat transfer in pulsatile turbulent channel flow, *International Journal of Heat and Mass Transfer* 144 (2019) 118585.

[41] H.M. Altay, R.L. Speth, D.E. Hudgins and A.F. Ghoniem, Flame–vortex interaction driven combustion dynamics in a backward-facing step combustor, *Combustion and Flame* 156 (2009) 1111-1125.

[42] K.T. Kim, J.G. Lee, B.D. Quay and D. Santavicca, Spatially distributed flame transfer functions for predicting combustion dynamics in lean premixed gas turbine combustors, *Combustion and Flame* 157 (2010) 1718-1730.

[43] K.T. Kim and S. Hochgreb, The nonlinear heat release response of stratified lean-

premixed flames to acoustic velocity oscillations, *Combustion and Flame* 158 (2011) 2482-2499.

[44] C. Coats, Z. Chang and P. Williams, Excitation of thermoacoustic oscillations by small premixed flames, *Combustion and Flame* 157 (2010) 1037-1051.

[45] P. Palies, D. Durox, T. Schuller and S. Candel, Nonlinear combustion instability analysis based on the flame describing function applied to turbulent premixed swirling flames, *Combustion and Flame* 158 (2011) 1980-1991.

[46] K.S. Kedia and A.F. Ghoniem, An analytical model for the prediction of the dynamic response of premixed flames stabilized on a heat-conducting perforated plate, *Proceedings of the Combustion Institute* 34 (2013) 921-928.

[47] Preetham, H. Santosh and T. Lieuwen, Dynamics of laminar premixed flames forced by harmonic velocity disturbances, *Journal of Propulsion and Power* 24 (2008) 1390-1402.

[48] S. Candel, D. Durox, T. Schuller, J.F. Bourgouin and J.P. Moeck, Dynamics of swirling flames, *Annual review of fluid mechanics* 46 (2014) 147-173.

[49] D. Durox, T. Schuller, N. Noiray and S. Candel, Experimental analysis of nonlinear flame transfer functions for different flame geometries, *Proceedings of the Combustion Institute* 32 (2009) 1391-1398.

[50] M. Haeringer, M. Merk and W. Polifke, Inclusion of higher harmonics in the flame describing function for predicting limit cycles of self-excited combustion instabilities, *Proceedings of the Combustion Institute* 37 (2019) 5255-5262.

[51] J. Hwang, NOx Scaling and Stability Characteristics of Turbulent Non-premixed Jet Flames of H2/CO Syngas, PhD Thesis, School of Mechanical and Aerospace Engineering, Seoul National University, 2014.

[52] Y. Hu, J. Tan, L. Lv and X. Li, Investigations on quantitative measurement of heat release rate using chemiluminescence in premixed methane-air flames, *Acta Astronautica* 164 (2019) 277-286.

[53] K. Ahn, Turbulent mixing and combustion control in dump combustors, PhD Thesis, School of Mechanical and Aerospace Engineering, Seoul National University, 2005.

[54] J. Kim, Characteristics of hydrogen diffusion flames stabilized on a bluff-body in supersonic flow, PhD Thesis, Department of Aerospace Engineering, Seoul National Univeristy, 2003.

[55] P. Magre and R. Dibble, Finite chemical kinetic effects in a subsonic turbulent hydrogen flame, *Combustion and Flame* 73 (1988) 195-206.

[56] R.S. Barlow, R.W. Dibble, J.Y. Chen and R.P. Lucht, Effect of Damköhler number on superequilibrium OH concentration in turbulent nonpremixed jet flames, *Combustion and Flame* 82 (1990) 235-251.

[57] J.M. Seitzman, A. Ü ngüt, P.H. Paul and R.K. Hanson, Imaging and characterization of OH structures in a turbulent nonpremixed flame, In Symposium (International) on Combustion, 1991, Elsevier, p. 637-644.

[58] S.R. Turns, Introduction to combustion, McGraw-Hill Companies, 1996.

[59] A. Lantz, Application of Laser Techniques in Combustion Environments of Relevance for Gas Turbine Studies, Department of Physics, Lund University, 2012.

[60] R. Puri, M. Moser, R.J. Santoro and K.C. Smyth, Laser-induced fluorescence measurements of oh· concentrations in the oxidation region of laminar, hydrocarbon diffusion flames, In Symposium (International) on Combustion, 1992, Elsevier, p. 1015-1022.

[61] R. Tolstoguzov, Temperature measurements in a Bunsen flame by planar laser-induced fluorescence, In Journal of Physics: Conference Series, 2020, IOP Publishing, p. 012045.

[62] J. Yoon, High Harmonic Combustion Instability Characteristics of H2/CH4 Fuel in a Partially Premixed Combustor, PhD Thesis, Department of Mechanical and Aerospace Engineering, Seoul National University, 2017.

[63] S. Hammack, S. Kostka, A. Lynch, C. Carter and T. Lee, Simultaneous 10-kHz PLIF and chemiluminescence imaging of OH radicals in a microwave plasma-enhanced flame, *IEEE Transactions on Plasma Science* 41 (2013) 3279-3286.

[64] P. Petersson, R. Wellander, J. Olofsson, H. Carlsson, C. Carlsson, B.B. Watz, N. Boetkjaer, M. Richter, M. Aldén and L. Fuchs, Simultaneous high-speed PIV and

OH PLIF measurements and modal analysis for investigating flame-flow interaction in a low swirl flame, *16th IntSymp on Applications of Laser Techniques to Fluid Mechanics*, (2012).

[65] P. Xavier, A. Vandel, G. Godard, B. Renou, F. Grisch, G. Cabot, M.A. Boukhalfa and M. Cazalens, Analysis of the flame structure in a trapped vortex combustor using low and high-speed OH-PLIF, In ASME Turbo Expo 2014: Turbine Technical Conference and Exposition, 2014, American Society of Mechanical Engineers Digital Collection, p. V04AT04A012.

[66] I. Boxx, M. Stöhr, C. Carter and W. Meier, Temporally resolved planar measurements of transient phenomena in a partially pre-mixed swirl flame in a gas turbine model combustor, *Combustion and Flame* 157 (2010) 1510-1525.

[67] M. Stöhr, I. Boxx, C. Carter and W. Meier, Dynamics of lean blowout of a swirl-stabilized flame in a gas turbine model combustor, *Proceedings of the Combustion Institute* 33 (2011) 2953-2960.

[68] M. Stöhr, C.M. Arndt and W. Meier, Effects of Damköhler number on vortex–flame interaction in a gas turbine model combustor, *Proceedings of the Combustion Institute* 34 (2013) 3107-3115.

[69] P.M. Allison, Y. Chen, M. Ihme and J.F. Driscoll, Coupling of flame geometry and combustion instabilities based on kilohertz formaldehyde PLIF measurements, *Proceedings of the Combustion Institute* 35 (2015) 3255-3262.

[70] S. Meares, V. Prasad, M. Juddoo, K. Luo and A. Masri, Simultaneous planar and volume cross-LIF imaging to identify out-of-plane motion, *Proceedings of the Combustion Institute* 35 (2015) 3813-3820.

[71] J. Dawson, R. Gordon, J. Kariuki, E. Mastorakos, A. Masri and M. Juddoo, Visualization of blow-off events in bluff-body stabilized turbulent premixed flames, *Proceedings of the Combustion Institute* 33 (2011) 1559-1566.

[72] N.A. Worth and J.R. Dawson, Cinematographic OH-PLIF measurements of two interacting turbulent premixed flames with and without acoustic forcing, *Combustion and Flame* 159 (2012) 1109-1126.

[73] T.C. Lieuwen, Unsteady combustor physics, Cambridge University Press, 2012.

[74] H. Wang, C.K. Law and T. Lieuwen, Linear response of stretch-affected premixed flames to flow oscillations, *Combustion and Flame* 156 (2009) 889-895.

[75] A. Sengissen, J. Van Kampen, R. Huls, G.G. Stoffels, J.B. Kok and T. Poinsot, LES and experimental studies of cold and reacting flow in a swirled partially premixed burner with and without fuel modulation, *Combustion and Flame* 150 (2007) 40-53.

[76] K.P. Geigle, W. Meier, M. Aigner, C. Willert, M. Jarius, P. Schmitt and B. Schuermans, Phase-resolved laser diagnostic measurements of a downscaled, fuel-staged gas turbine combustor at elevated pressure and comparison to LES predictions, *Journal of Engineering for Gas Turbines and Power-Transactions of the Asme* 129 (2007) 680-687.

[77] W. Cheung, G. Sims, R. Copplestone, J. Tilston, C. Wilson, S.R. Stow and A.P. Dowling, Measurement and analysis of flame transfer function in a sector combustor under high pressure conditions, In ASME Turbo Expo 2003, collocated with the 2003 International Joint Power Generation Conference, 2003, American Society of Mechanical Engineers Digital Collection, p. 187-194.

[78] A. Gentemann, C. Hirsch, K. Kunze, F. Kiesewetter, T. Sattelmayer and W. Polifke, Validation of flame transfer function reconstruction for perfectly premixed swirl flames, In ASME Turbo Expo 2004: Power for Land, Sea, and Air, 2004, American Society of Mechanical Engineers Digital Collection, p. 501-510.

[79] B. Varoquié, J. Légier, F. Lacas, D. Veynante and T. Poinsot, Experimental analysis and large eddy simulation to determine the response of non-premixed flames submitted to acoustic forcing, *Proceedings of the Combustion Institute* 29 (2002) 1965-1970.

[80] C. Paschereit, B. Schuermans, W. Polifke and O. Mattson, Measurement of transfer matrices and source terms of premixed flames, *Journal of Engineering for Gas Turbines and Power* 124 (2002) 239-247.

[81] G. Benham, I. Hewitt, C. Please and P. Bird, Optimal control of diffuser shapes for non-uniform flow, *Journal of engineering mathematics* 113 (2018) 65-92.

[82] L. Malvern, Introduction to the mechanics of a continuous medium. Englewood Cliffs, NJ: Prentice-Hall; 1969.

[83] R. Weijermars and M. Ettehad, Displacement field potentials for deformation in elastic Media: Theory and application to pressure-loaded boreholes, *Applied Mathematics and Computation* 340 (2019) 276-295.

[84] C. da Costa, M. Kashiwagi and M.H. Mathias, Rotor failure detection of induction motors by wavelet transform and Fourier transform in non-stationary condition, *Case Studies in Mechanical Systems and Signal Processing* 1 (2015) 15-26.

[85] T. Lieuwen, H. Torres, C. Johnson and B. Zinn, A mechanism of combustion instability in lean premixed gas turbine combustors, *J. Eng. Gas Turbines Power* 123 (2001) 182-189.

[86] N. Noiray, D. Durox, T. Schuller and S. Candel, A unified framework for nonlinear combustion instability analysis based on the flame describing function, *Journal of Fluid Mechanics* 615 (2008) 139-167.

[87] X. Han, J. Li and A.S. Morgans, Prediction of combustion instability limit cycle oscillations by combining flame describing function simulations with a thermoacoustic network model, *Combustion and Flame* 162 (2015) 3632-3647.

[88] L. Selle, G. Lartigue, T. Poinsot, R. Koch, K.U. Schildmacher, W. Krebs, B. Prade, P. Kaufmann and D. Veynante, Compressible large eddy simulation of turbulent combustion in complex geometry on unstructured meshes, *Combustion and Flame* 137 (2004) 489-505.

[89] J. Li and A.S. Morgans, Time domain simulations of nonlinear thermoacoustic behaviour in a simple combustor using a wave-based approach, *Journal of Sound and Vibration* 346 (2015) 345-360.

[90] C.F. Silva, F. Nicoud, T. Schuller, D. Durox and S. Candel, Combining a Helmholtz solver with the flame describing function to assess combustion instability in a premixed swirled combustor, *Combustion and Flame* 160 (2013) 1743-1754.

[91] G.M. Choi, M. Tanahashi and T. Miyauchi, Control of oscillating combustion and noise based on local flame structure, *Proceedings of the Combustion Institute* 30

(2005) 1807-1814.

[92] J. Moore and K. Kuo, Effect of Changing Methane/Oxygen Coaxial Injector Configuration on Diffusion Flame Stability, In 40th AIAA/ASME/SAE/ASEE Joint Propulsion Conference and Exhibit, 2004, p. 3714.

[93] J. Moore, G. Risha, K. Kuo, B. Zhang, R. Wehrman and M. D'Agostini, Stability of methane/oxygen coaxial diffusion flame, In 39th AIAA/ASME/SAE/ASEE Joint Propulsion Conference and Exhibit, 2003, p. 4636.

[94] B.R. Chowdhury and B.M. Cetegen, Effects of free stream flow turbulence on blowoff characteristics of bluff-body stabilized premixed flames, *Combustion and Flame* 190 (2018) 302-316.

[95] C. Hassa, J. Heinze and K. Stursberg, Investigation of the response of an air blast atomizer combustion chamber configuration on forced modulation of air feed at realistic operating conditions, *J. Eng. Gas Turbines Power* 125 (2003) 872-878.

[96] J. Bae, J. Yoon, S. Joo, J. Kim, C. Jeong, C.H. Sohn, I.N. Borovik and Y. Yoon, Predicting the Frequency of Combustion Instability Using the Measured Reflection Coefficient through Acoustic Excitation, *International Journal of Aeronautical and Space Sciences* 18 (2017) 797-806.

[97] T. Lieuwen and K. McManus, Introduction: Combustion dynamics in lean-premixed prevaporized (LPP) gas turbines, *Journal of Propulsion and Power* 19 (2003) 721-721.

[98] S. Ducruix, T. Schuller, D. Durox and S. Candel, Combustion dynamics and instabilities: Elementary coupling and driving mechanisms, *Journal of Propulsion and Power* 19 (2003) 722-734.

[99] K.T. Kim and D.A. Santavicca, Interference mechanisms of acoustic/convective disturbances in a swirl-stabilized lean-premixed combustor, *Combustion and Flame* 160 (2013) 1441-1457.

[100] J. Bae, S. Jeong and Y. Yoon, Effect of delay time on the combustion instability in a single-element combustor, *Acta Astronautica* 178 (2021) 783-792.

[101] N.A. Worth and J.R. Dawson, Effect of equivalence ratio on the modal dynamics of

azimuthal combustion instabilities, *Proceedings of the Combustion Institute* 36 (2017) 3743-3751.

[102] A. Urbano, L. Selle, G. Staffelbach, B. Cuenot, T. Schmitt, S. Ducruix and S. Candel, Exploration of combustion instability triggering using large eddy simulation of a multiple injector liquid rocket engine, *Combustion and Flame* 169 (2016) 129-140.

[103] O. Lucca-Negro and T. O'doherty, Vortex breakdown: a review, *Progress in Energy and Combustion Science* 27 (2001) 431-481.

[104] S. Hermeth, G. Staffelbach, L.Y. Gicquel, V. Anisimov, C. Cirigliano and T. Poinsot, Bistable swirled flames and influence on flame transfer functions, *Combustion and Flame* 161 (2014) 184-196.

[105] L. Tay-Wo-Chong and W. Polifke, Large eddy simulation-based study of the influence of thermal boundary condition and combustor confinement on premix flame transfer functions, *Journal of Engineering for Gas Turbines and Power* 135 (2013).

[106] K. Oberleithner, M. Stöhr, S.H. Im, C.M. Arndt and A.M. Steinberg, Formation and flame-induced suppression of the precessing vortex core in a swirl combustor: experiments and linear stability analysis, *Combustion and Flame* 162 (2015) 3100-3114.

[107] Q. An and A.M. Steinberg, The role of strain rate, local extinction, and hydrodynamic instability on transition between attached and lifted swirl flames, *Combustion and Flame* 199 (2019) 267-278.

[108] Z. Yin, P. Nau and W. Meier, Responses of combustor surface temperature to flame shape transitions in a turbulent bi-stable swirl flame, *Experimental Thermal and Fluid Science* 82 (2017) 50-57.

[109] S. Taamallah, S.J. Shanbhogue and A.F. Ghoniem, Turbulent flame stabilization modes in premixed swirl combustion: Physical mechanism and Karlovitz number-based criterion, *Combustion and Flame* 166 (2016) 19-33.

[110] D. Ebi, A. Denisov, G. Bonciolini, E. Boujo and N. Noiray, Flame dynamics intermittency in the bistable region near a subcritical hopf bifurcation, *Journal of*

Engineering for Gas Turbines and Power 140 (2018).

[111] G. Bonciolini, D. Ebi, E. Boujo and N. Noiray, Subcritical thermoacoustic bifurcation in turbulent combustors: effects of inertia, In 26th International Colloquium on the Dynamics of Explosions and Reactive Systems (ICDERS 2017), 2017.

[112] V.R. Unni, Y.M. Prasaad, N. Ravi, S.M. Iqbal, B. Pesala and R. Sujith, Experimental investigation of bifurcations in a thermoacoustic engine, *International Journal of Spray and Combustion Dynamics* 7 (2015) 113-129.

[113] R. Vishnu, R. Sujith and P. Aghalayam, Role of flame dynamics on the bifurcation characteristics of a ducted V-flame, *Combustion Science and Technology* 187 (2015) 894-905.

[114] J.W. Bennewitz, S.L. Rani, J.T. Cranford and R.A. Frederick Jr, Combustion Instability Control Through Acoustic Modulation at the Inlet Boundary: Analysis, *Journal of Propulsion and Power* 31 (2015) 1689-1695.

[115] J.W. Bennewitz, R.A. Frederick Jr, J.T. Cranford and D.M. Lineberry, Combustion Instability Control Through Acoustic Modulation at the Inlet Boundary: Experiments, *Journal of Propulsion and Power* 31 (2015) 1672-1688.

[116] A. Renaud, S. Ducruix, P. Scouflaire and L. Zimmer, Flame shape transition in a swirl stabilised liquid fueled burner, *Proceedings of the Combustion Institute* 35 (2015) 3365-3372.

[117] A. Renaud, S. Ducruix and L. Zimmer, Bistable behaviour and thermo-acoustic instability triggering in a gas turbine model combustor, *Proceedings of the Combustion Institute* 36 (2017) 3899-3906.

[118] D. Moore and P. Saffman, The density of organized vortices in a turbulent mixing layer, *Journal of Fluid Mechanics* 69 (1975) 465-473.

[119] D. Oster and I. Wygnanski, The forced mixing layer between parallel streams, *Journal of Fluid Mechanics* 123 (1982) 91-130.

[120] T. New and E. Tsioli, An experimental study on the vortical structures and behaviour of jets issuing from inclined coaxial nozzles, *Experiments in fluids* 51 (2011) 917-

932.

[121] F. Tabet, B. Sarh and I. Gökalp, Hydrogen–hydrocarbon turbulent non-premixed flame structure, *International journal of hydrogen energy* 34 (2009) 5040-5047.

[122] T.M. Nguyen, P.P. Popov and W.A. Sirignano, Longitudinal combustion instability in a rocket engine with a single coaxial injector, *Journal of Propulsion and Power* 34 (2018) 354-373.

[123] I.J. Wygnanski and R.A. Petersen, Coherent motion in excited free shear flows, *AIAA journal* 25 (1987) 201-213.

[124] C. Jeong, J. Bae, T. Kim, J. Yoon, S. Joo and Y. Yoon, Investigation of flashback characteristics coupled with combustion instability in turbulent premixed bluff body flames using high-speed OH-PLIF and PIV, *Proceedings of the Combustion Institute* 36 (2017) 1861-1868.

[125] T.C. de Souza, B.J. Geurts, R. Bastiaans and L. De Goey, Steady large-scale modulation of a moderately turbulent co-flow jet, *Journal of turbulence* 15 (2014) 273-292.

[126] E.R. Hawkes, R. Sankaran, J.C. Sutherland and J.H. Chen, Scalar mixing in direct numerical simulations of temporally evolving plane jet flames with skeletal CO/H2 kinetics, *Proceedings of the Combustion Institute* 31 (2007) 1633-1640.

[127] J. Pieringer, T. Sattelmayer and F. Fassl, Simulation of combustion instabilities in liquid rocket engines with acoustic perturbation equations, *Journal of Propulsion and Power* 25 (2009) 1020-1031.

[128] K.T. Kim, H.J. Lee, J.G. Lee, B. Quay and D. Santavicca, Flame transfer function measurement and instability frequency prediction using a thermoacoustic model, In ASME Turbo Expo 2009, 2009, International Gas Turbine Institute, p. GT2009-60026.

[129] M.C. Lee, J. Yoon, S. Joo, J. Kim, J. Hwang and Y. Yoon, Investigation into the cause of high multi-mode combustion instability of H2/CO/CH4 syngas in a partially premixed gas turbine model combustor, *Proceedings of the Combustion Institute* 35 (2015) 3263-3271.

[130] M. Stöhr, C.M. Arndt and W. Meier, Transient effects of fuel–air mixing in a partially-premixed turbulent swirl flame, *Proceedings of the Combustion Institute* 35 (2015) 3327-3335.

[131] L. Hakim, A. Ruiz, T. Schmitt, M. Boileau, G. Staffelbach, S. Ducruix, B. Cuenot and S. Candel, Large eddy simulations of multiple transcritical coaxial flames submitted to a high-frequency transverse acoustic modulation, *Proceedings of the Combustion Institute* 35 (2015) 1461-1468.

[132] N. Magina, D.H. Shin, V. Acharya and T. Lieuwen, Response of non-premixed flames to bulk flow perturbations, *Proceedings of the Combustion Institute* 34 (2013) 963-971.

[133] D.H. Huang and D.K. Huzel, Modern engineering for design of liquid-propellant rocket engines, American Institute of Aeronautics and Astronautics, 1992.

[134] A.G. Gaydon and H.G. Wolfhard, Flames, their structure, radiation, and temperature, Halsted Press, 1979.

[135] J. Kojima, Y. Ikeda and T. Nakajima, Spatially resolved measurement of OH*, CH*, and C2* chemiluminescence in the reaction zone of laminar methane/air premixed flames, *Proceedings of the Combustion Institute* 28 (2000) 1757-1764.

[136] P. Hazel, Numerical studies of the stability of inviscid stratified shear flows, *Journal of Fluid Mechanics* 51 (1972) 39-61.

[137] H. Kim and P. Durbin, Observations of the frequencies in a sphere wake and of drag increase by acoustic excitation, *The Physics of fluids* 31 (1988) 3260-3265.

[138] H. Sakamoto and H. Haniu, A study on vortex shedding from spheres in a uniform flow, *Journal of Fluid Engineering* 112 (1990) 386-392.

[139] C. Saleel, A. Shaija and S. Jayaraj, Computational simulation of fluid flow over a triangular step using immersed boundary method, *International Journal of Computational Methods* 10 (2013) 1350016.

[140] K.B. Chun and H.J. Sung, Control of turbulent separated flow over a backward-facing step by local forcing, *Experiments in fluids* 21 (1996) 417-426.

[141] S. Bhattacharjee, B. Scheelke and T.R. Troutt, Modification of vortex interactions in

a reattaching separated flow, *AIAA journal* 24 (1986) 623-629.

[142] F.W. Roos and J.T. Kegelman, Control of coherent structures in reattaching laminar and turbulent shear layers, *AIAA journal* 24 (1986) 1956-1963.

[143] J. Tsohas, Hydrodynamics of shear coaxial liquid rocket injectors, Purdue University, 2009.

[144] S. Candel, M. Juniper, G. Singla, P. Scouflaire and C. Rolon, Structure and dynamics of cryogenic flames at supercritical pressure, *Combustion Science and Technology* 178 (2006) 161-192.

[145] K. Ahn, Y.M. Han, S. Seo and H.S. Choi, Effects of injector recess and chamber pressure on combustion characteristics of liquid–liquid swirl coaxial injectors, *Combustion Science and Technology* 183 (2010) 252-270.

[146] L. Crocco, Theoretical studies on liquid-propellant rocket instability, In Symposium (International) on Combustion, 1965, Elsevier, p. 1101-1128.

[147] S. Ducruix, D. Durox and S. Candel, Theoretical and experimental determinations of the transfer function of a laminar premixed flame, *Proceedings of the Combustion Institute* 28 (2000) 765-773.

[148] F. Boudy, D. Durox, T. Schuller and S. Candel, Nonlinear mode triggering in a multiple flame combustor, *Proceedings of the Combustion Institute* 33 (2011) 1121-1128.

초 록

추진 기관 및 저 NO_x 가스터빈 연소기의 설계 과정에서 발생하는 가장 큰 걸림돌 중 하나인 연소불안정을 해결하기 위한 수많은 연구가 진행되어 왔음에도 불구하고, 아직까지 이를 위한 완전한 해결책은 제시되지 못하고 있다. 연소불안정에 관한 선행 연구에서는 주로 당량비 혹은 O/F 비에 따른 연소 특성을 파악했으나, 동일한 작동조건임에도 불구하고 서로 다른 구조를 갖는 쌍안정 화염이 형성되기도 하며 각 화염은 서로 다른 특성을 보여주기 때문에 화염 구조 역시 연소불안정을 판단함에 있어 반드시 고려되어야 한다. 또한, 연소불안정은 주로 고주파 영역에서 발생하나 화염의 특성을 나타내는 화염전달함수는 주로 저주파 영역에서만 측정되었기 때문에 연소불안정과 화염전달함수의 직접적인 비교는 수행되지 못하였다. 더군다나 연소불안정에 관한 연구는 주로 가스터빈에서 사용되는 예혼합화염에 집중되어 있으며, 발사체에서 사용되는 비예혼합화염에 관한 연구는 부족한 실정이다. 그러나 발사 이후 작동을 중단시키고 개선작업을 수행하기 어려운 발사체의 특성 상 연소불안정은 사전에 완벽하게 해결되어야 한다.

본 연구에서는 최근 발사체 재사용을 위한 친환경 연료로 각광받고 있는 메탄을 사용하여 리세스를 가지는 동축형 분사기의 연소불안정 특징을 파악하였다. 이 과정에서 화염의 구조 및 불안정 모드 천이 현상의 원인 파악에 대한 상세 연구를 수행하였다. 또한, 연소불안정 연구의 최종 목표인 연소불안정 예측을 위하여 화염전달함수에 관한 연구도 수행하였다.

연소불안정 특징을 파악하기에 앞서 쌍안정 화염의 특성파악을 위하여 O/F 비 및 외부 섭동에 따른 화염 구조 파악을 위한 연소시험을 수행하였다. 그 결과 부착화염과 부상화염이 발생하였으며, 부상화염일 때 압력 및 열방출율 섭동이 더 강하게 발생하였다. O/F 비의 증가는 부상화염에서 부착화염으로의 천이를 야기하였고, 부착화염은 O/F 비의 변화에도 불구하고 부착화염의 상태를 유지하였다. 외부 음향 섭동은 그 세기에 따라 화염 구조에 다른 영향을 주었으며, 일반적으로 음향 섭동은 부상화

염에서 부착화염으로의 천이를 야기하였으나, 매우 강한 섭동은 오히려 부착화염에서 부상화염으로의 천이를 야기하였다. O/F 비의 변화와 외부 음향 섭동은 산소와 메탄 사이의 속도차를 발생시키며, 속도차가 클수록 둘 사이의 강한 혼합이 발생하여 화염이 인젝터 쪽으로 당겨져 오게 되고, 결과적으로 부상화염에서 부착화염으로의 천이가 발생한다. 다만, 매우 강한 음향 섭동은 오히려 정상적인 화학 반응을 방해하며, 국소 소염을 야기하기 때문에 부착화염에서 부상화염으로의 천이를 야기시키는 것으로 판단되었다. 화염 구조 간의 천이 현상은 화염 구조 계측 및 continuous wavelet transform을 활용한 압력 신호를 통해 분석되었다.

다음으로, 음향 섭동 시험을 통해 연소실 후단에 닫힌 음향 경계를 형성시키는 것이 확인된 플러그 노즐을 사용하여 연소시험을 수행하였다. O/F 비의 변화에 따라 발생하는 불안정 주파수에 대한 모드 분석을 수행하였으며, 연소실 길이방향 공진 주파수의 1st, 3rd, 4th에 해당하는 불안정임을 확인하였다. 이에 대한 상세 연구를 위하여 각 O/F 조건에서 전체 시간 지연을 계측하였으며, 불안정 모드는 전체 시간 지연에 반비례하도록 천이되는 것을 확인하였다. 이러한 원인은 Rayleigh criterion에 의해 전체 시간 지연이 증가함에 따라 연소실 내부의 압력 섭동과 열방출율 섭동의 보강간섭이 발생하는 음향 모드가 낮은 모드로 천이되기 때문인 것으로 예측되었다.

또한, 일정한 O/F 비에서 연소실 길이를 증가시키면, 불안정 주파수는 연소실의 공진 주파수와 일치하도록 서서히 감소하다가 다음 모드로 천이되는 현상이 발생하였는데, 연소실 길이 변화 역시 Rayleigh criterion에 의해 연소실 내부의 압력 섭동과 열방출율 섭동 사이의 위상차 변화를 야기하여 보강간섭이 발생하는 음향 모드의 변화를 발생시키기 때문인 것으로 판단되었다. 또한, 각 O/F 비 조건에서 연소실 길이를 변화시켜감에 따라 가장 큰 압력 섭동이 발생하는 주파수를 연소불안정 주파수로 정의하고 분석한 결과 전체 시간 지연과 연소불안정 주파수는 반비례 관계가 있음을 확인하였다. 이는 시간 지연 분석기법에 따라 전체 시간 지연과 불안정 주파수의 곱이 일정한 값을 가질 때 이론적으로 연소실 내부의 압력 섭동과 열방출율 섭동 사이에 보강간섭이 발생하여 연소불안정이 발생하기 때문이며, 본 연구에서 측정된 전체 시간 지연과 불안정 주파수의 곱은 이론 값인 0.5와 일치하는 것을 확인하였다.

마지막으로 화염의 특성을 파악하여 연소불안정 예측에 활용될 수 있는 화염전달함

수에 관한 연구를 수행하였다. 먼저, 쌍안정 화염의 화염전달함수를 측정한 결과 부상 화염의 화염전달함수는 부착화염에 비해 큰 gain이 발생하였다. 화염전달함수의 gain은 동일한 외부 섭동에 따른 열방출율 섭동을 의미하므로, 부상화염이 외부 교란에 더 민감함을 나타낸다. 또한, 각 O/F 비에서 화염전달함수를 측정하였고, gain의 peak이 발생하는 주파수는 연소불안정 주파수와 거의 일치하는 것으로 확인되었다. 화염전달함수 gain의 peak은 화염의 내재적 불안정 주파수를 의미하며, 해당 주파수 섭동에 가장 큰 교란이 야기됨을 의미한다. 즉, 내재적 불안정 주파수와 동일한 공진주파수를 가지는 연소실에서는 해당 주파수 섭동의 공진 효과로 인해 화염의 떨림이 증폭되는 양의 피드백 현상이 발생하게 되어 연소불안정이 발생하기 때문에 화염전달함수 gain의 peak 주파수와 연소불안정 주파수는 일치하는 것으로 판단되었다. 또한, 측정된 화염전달함수 및 화염의 구조를 사용하여 연소불안정 예측을 수행한 결과 실험에서 발생하였던 불안정 모드 천이 현상 및 연소불안정 주파수가 유사하게 예측되는 것을 확인할 수 있었다.

상기 연구를 통하여 리세스를 가진 동축형 분사기에서 발생하는 비예혼합화염의 화염 구조 및 연소불안정에 대한 다양한 특성을 파악하였으며, 화염전달함수에 관한 연구도 수행되었다. 이러한 연구는 비예혼합화염을 활용한 연소시스템의 연소안정성 향상, 비예혼합화염의 구조 및 연소불안정 특성을 파악하기 위한 연구의 선행연구자료로 활용될 수 있을 것으로 기대된다.

중심어: 비예혼합 화염, 리세스를 가진 동축형 분사기, 쌍안정 화염, 화염구조, 연소불안정, 연소불안정 모드 천이, 시간 지연 분석기법, 화염전달함수, OH-PLIF, PIV, 연소불안정 예측

학 번: 2015-20773